A Gated Breath-Hold Radiotherapy Technique Using a Linear Position Transducer

Svetlana Denissova
Medical Physics Unit
McGill University
Montréal, Québec
August 2003.

A thesis submitted to McGill University in partial fulfillment of the requirements for the degree of Master of Science in Medical Radiation Physics.

Acknowledgements

I would like to thank Dr. Ervin B. Podgorsak and all my McGill medical physics instructors in the Medical Physics Unit (MPU) of McGill University for giving me a good basic knowledge of Medical Physics and related disciplines, as well as teaching me a creative approach to studying that was very important for realization of this project.

The thesis work was carried out under the auspices of McGill University in Montreal; however, the research work was carried out in the Medical Physics Department of the Nova Scotia Cancer Center (NSCC) in Halifax. The special arrangement reached between the MPU and the Medical Physics Department of the NSCC that allowed me to work on my research topic at the NSCC rather than at McGill was very convenient for my family life and is thus very much appreciated.

I would like to make my special acknowledgements to my supervisor Dr. Mammo Yewondwossen of the NSCC for involving me in the project, sharing his knowledge with me and guiding me through difficult steps during my research work. Special thanks are due to Dr. John W. Andrew for allowing me to work in his department and for his constant and total support of my work during this project. I also appreciate very much the useful advice, assistance in experiments, contribution in software development, and very interesting discussions with Carl Murphy and Scott Purcell. I am grateful to Ian Porter who designed and developed hardware for linear accelerator gating and CT experiments.

I would also like to recognize the contribution in developing and implementing of this technique and very fruitful cooperation with Dr. Liam Mulroy, Dr. Wladislawa Swajna, Lisa Bourne, Helen Burgess, Joleen Orr, CarolAnn Jessiman, Heather Edstrom, Dr. Jim Meng, Dr. Mike Hale, Dr. James Robar, Michael D.C. Evans, Jason Schella, David Burgess, James Allan and Pam Colbourne.

I am very grateful to my husband Serguei and my daughter Julia for their patience, understanding and support.

Table of Contents

Abstract

For patients with thoracic and abdominal lesions, respiration-induced internal organ motion and deformations during radiation therapy are limiting factors for the administration of high radiation dose. In order to escalate the dose to the tumor and reduce the treatment margins, the tumor movement during treatment must be minimized. In our approach we have established a largely automated deep-breath-hold technique for treating lung cancer patients. We have used a Linear Position Transducer to monitor tumor movement through changes in the patient's abdominal cross-sectional area. The technique aims to reduce the amount of healthy lung tissue in high-dose regions. Normal tissue can be spared as a result of two distinct features of this method: deep inspiration, which reduces the lung density, and breath hold, which immobilizes the tumor. Due to reduced tumor motion, the Planning Target Volume margins can be tightened and a higher dose of radiation can be delivered to the tumor with the same risk of normal tissue complications.

Résumé

Pour des patients avec les lésions thoraciques et abdominales, le mouvement et les déformations internes d'organes induits par respiration pendant la radiothérapie sont des facteurs limitants pour l'administration d'une dose élevée de rayonnements ionisants. Pour augmenter la dose à la tumeur et réduire les marges, le mouvement de la tumeur pendant le traitement doit être réduit au minimum. Dans notre approche nous avons établi une technique entièrement automatisée pour traiter des patients atteints du cancer du poumon. Nous avons utilisé un capteur de position linéaire (LPT) pour surveiller le mouvement de la tumeur par des changements de circonférence abdominale du patient. La technique vise à réduire la quantité de tissu pulmonaire sain dans la région à dose élevée. Deux caractéristiques distinctes de cette méthode permettent d'épargner les tissus sains: l'inspiration profonde, qui réduit la densité de poumon et la rétention du souffle, qui immobilise la tumeur. Grâce à la réduction des mouvements de la tumeur, les marges du volume planifié de la tumeur peuvent être réduites et une dose plus élevée de rayonnements ionisants peut être donnée à la tumeur avec le même risque de complications pour les tissus sains.

Chapter 1.
Introduction

Normally body cells reproduce by dividing in an orderly fashion so that growth and repair of the body tissues can take place. Cancer develops when cells start to grow out of control. Even though the term "cancer" is applied to more than 100 diseases, all cancers start because of an out-of-control growth of abnormal cells. Different types of cancer can behave and respond to treatments differently. Lung cancer is one of the most common types of cancer.

The National Cancer Institute of Canada statistics estimated 136,900 new cases of cancer and 66,200 deaths from cancer in Canada in 2002[1]. Breast cancer for women and prostate cancer for men are and will continue to be the most frequently diagnosed types of cancer. The second most common cancer for both sexes is lung cancer. Lung cancer is considered to be the leading cause of cancer death among both men and women. It kills more patients than the next five most common cancers combined. At least 85 percent of patients who develop lung cancer die from it[2] (Figs. 1.1 and 1.2).

There are two main types of lung cancer: non–small cell lung cancer and small cell lung cancer (Fig. 1.3). The cancer cells of these two types of lung cancer look different under a microscope, grow and spread in different ways and should be treated differently. Almost 80% of lung cancer patients are diagnosed with non–small cell lung cancer (NSCLC) that is subdivided into three types named for the kinds of cells found in the cancer and their appearence when viewed under a microscope.

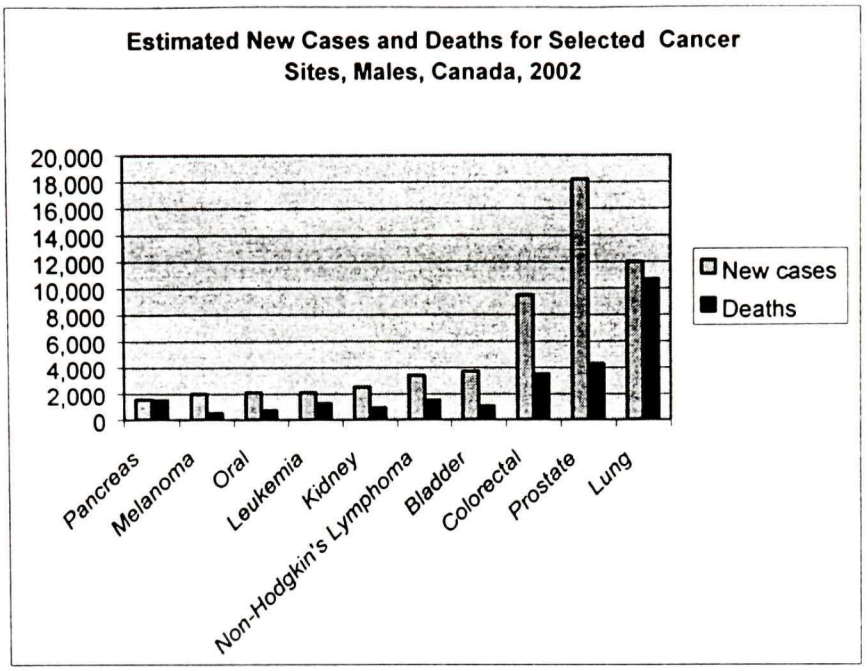

Figure 1.1. Estimated New Cases and Deaths for Selected Cancer Sites, Males, Canada, 2002.

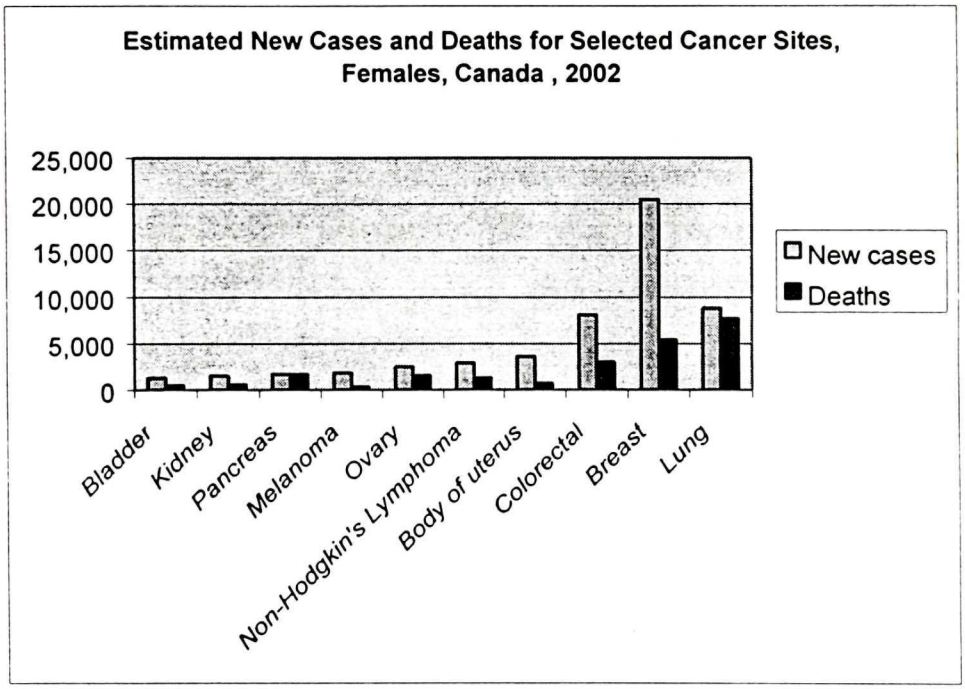

Figure 1.2. Estimated New Cases and Deaths for Selected Cancer Sites, Females, Canada, 2002.

The three types of lung cancer are: **squamous cell carcinoma** is a type of cancer that begins in squamous cells, which are thin, flat cells; **adenocarcinoma** begins in cells that have glandular properties and **large cell carcinoma** is a cancer in which the cells are large and look abnormal when viewed under a microscope.

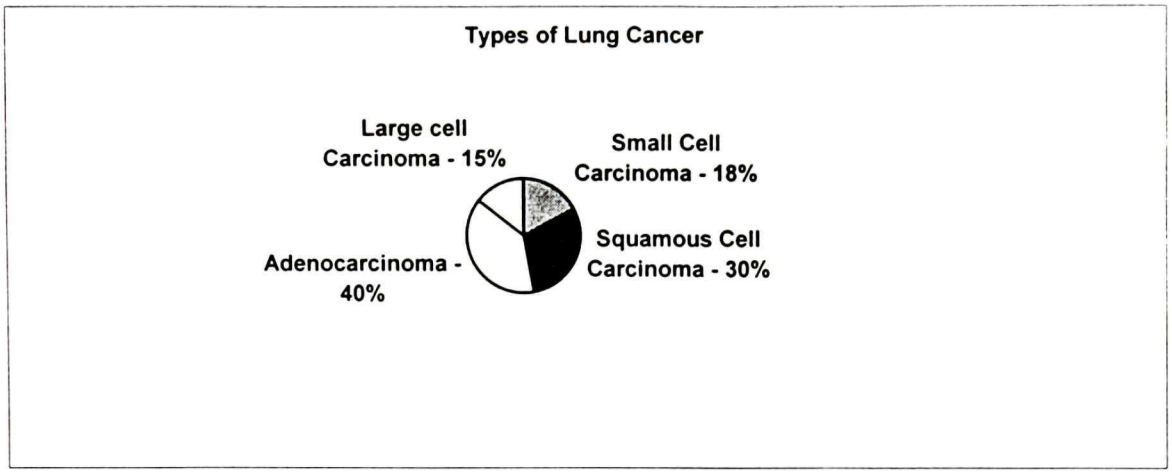

Figure 1.3. Types of Lung Cancers[3].
(Numbers do not add to 100% because of differences in diagnostic criteria.)

Surgery is the primary, potentially curative, therapeutic option for lung cancer. However, because of stage and medical condition at presentation, it is estimated that only 20% of patients initially presenting with lung cancer are eligible for definitive surgery[4]. For the remaining 80%, radiation therapy can produce a cure in a small minority and palliation in the majority of patients. For most patients with non-small cell lung cancer, current treatments do not cure the cancer: in 1992 for Canada, the overall age-standardized five-year relative survival rate for lung cancer was 17% and 14% among women and men, respectively[1]. Because of poor results obtained with standard treatment, all newly diagnosed patients with NSCLC are potential candidates for studies evaluating new forms of treatment.

Much effort is concentrated on improving radiation treatment response and increasing survival rate among the lung cancer patients. Certain factors affect the

response to radiation, such as patient's characteristics (general health, weight loss), tumor characteristics (clinical stage, size of the lesion), type of cancer, etc. Among the variety of factors, technical parameters related to delivery of external beam radiation play a very important role in the probability of controlling the lesion. High risk of local and distant failure for lung cancer patients can be attributed to errors in dose delivery and portal design resulting in inadequate coverage of the primary tumor. Theoretically, all cancers could be controlled locally, if a sufficiently high radiation dose could be delivered to the treatment volume. In practice, the administration of a high radiation dose to sterilize all tumor cells could cause severe damage to normal tissue, surrounding the tumor. Therefore a balance between delivering a high dose to the tumor and avoiding complications for healthy tissue is required. The possibility of very precise localization of the tumor during the treatment and very accurate dose delivery per fraction will lead to some improvements in the therapeutic ratio (i.e., the ratio of the dose required to eradicate every tumor cell to the dose that produces unacceptable normal tissue toxicity).

The most important limiting factor in radiation treatment of lung cancer patients is tumor movement during the respiration cycle. In conventional external beam radiotherapy, to cover the tumor motion during breathing, a planning target volume (PTV) includes a margin to account for this as well as other uncertainties in positions, sizes, shapes and orientations of both the tissues, patient and the beams in relation to the common coordinate system[5]. As a result of respiration, tumor motion in the lungs can vary from 0 cm up to 5 cm[6,7,8,9] and the typical range of movement is from 1 cm to 3 cm. In the case of considerable range of tumor movement, an attempt to deliver an adequate dose to the tumor will increase the risk of severe normal tissue complications.

One of the approaches to solve this problem is breathing-synchronized radiotherapy (BSRT). This technique allows correlating treatment delivery with respiratory cycle. As a result, the radiation field can be substantially reduced to avoid normal tissue complications, while allowing higher doses to the tumor, thus improving chances of local tumor control. Tumor motion is tracked with an organ motion detector and appropriate treatment is delivered with the help of a respiration-synchronized radiotherapy technique. Direct or indirect tumor motion detection can be used. Direct monitoring is performed with the help of diagnostic X-ray imaging, while indirect detection estimates tumor displacement from chest wall movement, monitoring air volume in the lungs, airflow temperature variations, or change in a cross-sectional area of the thorax. A good correlation between the motion of the tumor and the motion of the diaphragm, as monitored by external detectors, was demonstrated in several research projects[8,10,11].

The purpose of this work is to develop and implement a Deep Inspiration Breath Hold (DIBH) technique in the Nova Scotia Cancer Center for radiotherapy treatment of Non-Small Cell Lung Cancer (NSCLC) patients. The technique has two aims. The first aim is to reduce the amount of healthy lung tissue in high dose regions. Normal tissue can be spared due to two distinct features of this method: deep inspiration, which reduces the lung density, and breath hold, which immobilizes the tumor. Due to reduced tumor motion, Planning Target Volume (PTV) margins can be reduced and a higher dose of radiation can be delivered to the tumor with the same risk of normal tissue complications. The second aim is to escalate the dose to the tumor. DIBH allows for tumor dose escalation, while maintaining or reducing the surrounding normal tissue dose.

Chapter 2.

Interaction of ionizing radiation with matter

Radiation is a process of transmitting energy or mass through space. Radiation can be divided into two main groups – ionizing and non-ionizing, depending on its ability to ionize matter. Ionizing radiation can cause the removal of an electron from the atom that then acquires a charge (ionization) or the displacement of an orbital electron from an allowed orbit to a higher allowed orbit (excitation). Directly ionizing radiation (fast charged particles, such as electrons, protons or other heavy ions) delivers energy directly to the matter through multiple Coulomb interactions along the particle's track. Indirectly ionizing radiation (uncharged particles such as X– or γ–ray photons, neutrons) first transfers kinetic energy (KE) to directly ionizing charged particles (electrons or protons), and then these particles deliver the energy to the matter through direct Coulomb interactions.

2.1 Electron interactions

Traveling electrons lose their kinetic energy through interactions mediated by Coulomb forces between their electric fields and electric fields of orbital electrons and nuclei of a material. The interactions can be classified using the relationship between the impact parameter *b* (the distance by which the electron misses making a direct hit on the atomic nucleus) and the atomic radius *a* (Fig. 2.1).

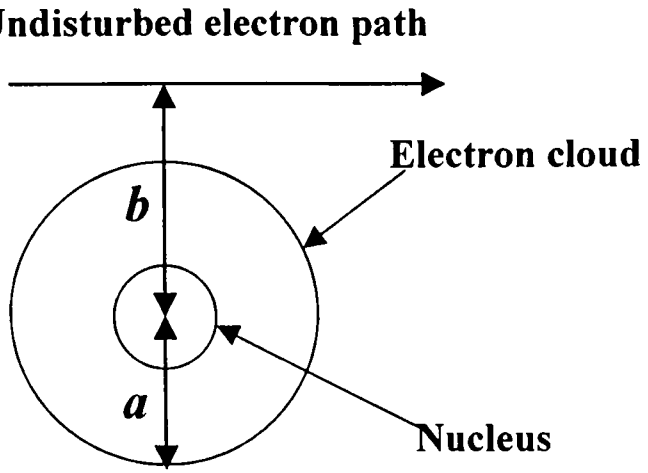

Figure 2.1. Schematic diagram of possible electron interactions.

When impact parameter b is significantly larger than the atomic radius a – the traveling electron interacts with the atom as a whole. This kind of interaction is referred to as a soft collision. The term hard collision refers to an interaction between a traveling electron and orbital electrons. Hard collisions occur when the impact parameter b is of the same order as the atomic radius a. These two types of collisions are predominantly ionizing events that result in a loss of electron kinetic energy (collisional energy loss). This energy loss is proportional to the square of the particle charge and inversely proportional to the particle velocity.

The third possible type of interaction occurs between a traveling electron and a nucleus, when the impact parameter b is significantly smaller than the atomic radius a. In the majority of cases these interactions result in elastic scattering with little or no consequence for kinetic energy loss. These interactions are referred to as elastic collisions. Scattering is described by scattering power, which varies as the square of Z and inversely as the square of the kinetic energy.

In a minority of cases, electron-nucleus interactions lead to electron deceleration which gives rise to the production of bremsstrahlung or "braking radiation". During this process, an electron approaches the atomic nucleus and is slowed or completely stopped by the Coulomb force of the nucleus. If the electron is slowed down, it will continue its trajectory with reduced energy. The loss in energy will be emitted as a photon with energy $h\nu$. If the electron is completely stopped by the positive nucleus force, the emitted X-ray photon will have an energy equal to the total kinetic energy of the electron.

The angle of maximum emitted photon intensity θ_{max} can be determined using the following formula:

$$\theta_{\max} = \arccos\left[\frac{1}{3\beta}\left(\sqrt{1+15\beta}-1\right)\right] , \qquad (2.1)$$

where $\beta = \frac{v}{c}$, c = 3x10^8 m/s - speed of light in vacuum.

Simple analysis shows that for $\beta \rightarrow 0$ (electron speed significantly less than the speed of light) $\theta_{max} \rightarrow \pi/2$ and for $\beta \rightarrow 1$ (electron speed close to the speed of light) $\theta_{max} \rightarrow 0$. This is the reason that in diagnostic radiology, X-rays produced using electrons with kinetic energies in the orthovoltage range are oriented 90° to the electronic path, and in radiotherapy X-ray photons produced by electrons in the megavoltage range are emitted predominantly in the direction of electrons striking the target[12].

The total mass stopping power S_{tot}/ρ is a macroscopic quantity that describes the rate of kinetic energy (KE) loss per unit path length x as follows:

$$\frac{S_{tot}}{\rho} = \frac{1}{\rho}\frac{d(KE)}{dx} , \qquad (2.2)$$

where ρ is the density of a material

The total mass stopping power is measured in MeV cm^2/g and can be divided into a collisional component (electron-orbital electron interactions, resulting in atomic ionizations and excitations) and a radiative component (electron-nucleus interactions, resulting in bremsstrahlung radiation):

$$\frac{S_{tot}}{\rho} = \frac{S_{col}}{\rho} + \frac{S_{rad}}{\rho} \quad . \tag{2.3}$$

The bremsstrahlung radiation yield can be determined, using both the total and radiation mass stopping powers:

$$g = \frac{1}{KE_i} \int_0^{KE_i} \frac{S_{rad}/\rho}{S_{tot}/\rho} d(KE) \quad , \tag{2.4}$$

where KE_i is the initial energy of the electron.

Bremsstrahlung yield g or energy loss by radiation as the electron travels through the medium is directly proportional to the kinetic energy of the electron and the medium's atomic number Z. Because of this dependence the bremsstrahlung yield for X-ray targets is 10-20% in the megavoltage range (radiotherapy), while in the orthovoltage range it is only 1% (diagnostic radiology). The remainder of electron kinetic energy is deposited in the target mostly as heat, making the target cooling a very important issue.

In radiation dosimetry the dose in the medium can be expressed using the collision mass stopping power S_{col}/ρ and the fluence of the electrons ϕ:

$$D = \phi\left(S_{col}/\rho\right) \quad , \tag{2.5}$$

To account only for the energy deposited locally in the vicinity of a particle track a concept of restricted mass stopping power $\left(L/\rho\right)_\Delta$ was introduced in radiation

dosimetry. Restricted mass stopping power considers collisional losses from soft collisions plus those from hard collisions with secondary electrons with less than some delta energy cutoff (Δ) usually taken as 10 keV.

2.2 Photon interactions

Photons interact with matter by absorption and scatter. A photon beam can be described with the help of the following concepts.

The **photon fluence** is the number photons *dN* per cross-sectional area *da* (unit: cm^{-2}):

$$\phi = \frac{dN}{da} \quad . \tag{2.6}$$

Photon fluence rate is photon fluence per unit time (unit: $cm^{-2} \cdot s^{-1}$):

$$\varphi = \frac{d\phi}{dt} \quad . \tag{2.7}$$

Energy fluence is the quotient of *dE* by *da*, where *dE* is the radiant energy incident per cross-sectional area *da* (unit: $MeV.cm^{-2}$):

$$\Psi = \frac{dE}{da} \quad . \tag{2.8}$$

Energy fluence rate or energy flux density is defined as energy fluence per unit time (unit: $MeV \cdot cm^{-2} \cdot s^{-1}$):

$$\Psi \quad = \frac{d\Psi}{dt} \quad . \tag{2.9}$$

Photon beams passing through matter are attenuated. Attenuation of a narrow monoenergetic photon beam may be described by following equations:

$$I(x) = I(0)e^{-\mu(h\upsilon, Z)x} \quad , \tag{2.10}$$

where *I(0)* is the intensity of the beam incident on the absorber; *I(x)* is the intensity of the beam after it has been attenuated by the absorber of the thickness *x;* and μ is the linear attenuation coefficient, which depends on photon energy and the nature of the material (atomic number *Z* and density) and represents the fraction of photons that interact per unit thickness of attenuator (unit: cm^{-1}).

The **Half-Value Layer** ($x_{1/2}$) is defined as the thickness of an attenuator that is required to reduce the beam intensity to a half of its original value:

$$x_{1/2} = \frac{\ln 2}{\mu} \quad . \tag{2.11}$$

For non-monoenergetic photon beams the lower energy (softer) components of a spectral distribution are attenuated preferentially resulting in beam hardening and an increase in the half-value layer thickness.

The **linear attenuation coefficient** μ is related to the **mass attenuation coefficient** μ_m (unit: cm^2/g), **atomic attenuation coefficient** ${}_a\mu$ (unit: cm^2/atom) and **electronic attenuation coefficient** ${}_e\mu$ (unit: cm^2/electron) as follows:

$$\mu = \rho\mu_m = \frac{\rho N_A}{A}{}_a\mu = \frac{\rho N_A Z}{A}{}_e\mu \quad . \tag{2.12}$$

There are two additional attenuation coefficients, which are used in radiation dosimetry. The **energy transfer coefficient** μ_{tr} describes the fraction of photon energy transferred on average into kinetic energy of charged particles per unit thickness of attenuator and it is related to the linear attenuation coefficient μ as:

$$\mu_{tr} = \mu\frac{\overline{E_{tr}}}{h\nu} \quad , \tag{2.13}$$

where $\overline{E_{tr}}$ is the average energy transferred to kinetic energy of charged particles per photon *(hv)* interaction.

The **energy absorption coefficient** μ_{ab} excludes the fraction of the transferred energy that is lost to bremsstrahlung radiation, i.e.:

$$\mu_{ab} = \mu_{tr}(1-g) \tag{2.14}$$

or

$$\mu_{ab} = \mu\frac{\overline{E_{ab}}}{hv} \quad , \tag{2.15}$$

where g represents the fraction of radiative energy loss (bremsstrahlung yield) and $\overline{E_{ab}}$ is the energy absorbed in the medium.

A photon beam passing through material is attenuated due to the following photon interactions with atoms of the medium: coherent scattering, photoelectric effect, Compton (or incoherent) scattering, pair production, triplet production and photonuclear disintegration. The probability of each of these processes depends on the photon energy hv and attenuator material atomic number Z. Each of those interactions can be described by its own attenuation coefficient. The total attenuation coefficient μ can be represented as a sum of individual attenuation coefficients, i.e.,

$$\mu = \tau + \sigma_{coh} + \sigma_{incoh} + \kappa_{pair} + \kappa_{triplet} + \sigma_{ph.n} \quad , \tag{2.16}$$

where τ, σ_{coh}, σ_{incoh}, κ_{pair}, $\kappa_{triplet}$, $\sigma_{ph.n}$ are attenuation coefficients of the photoelectric effect, coherent scattering, Compton (incoherent) scattering, pair production, triplet production and photonuclear disintegration respectively.

2.2.1 Coherent (Rayleigh) scattering

Coherent scattering is the photon interaction with a bound orbital electron, i.e., with the combined action of the whole atom (Fig. 2.2).

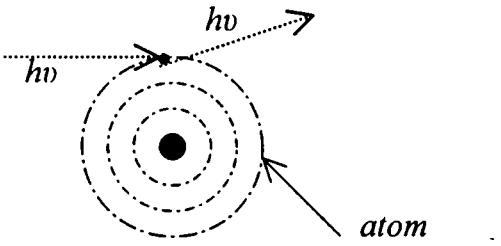

Figure 2.2. Coherent scattering.

During this event all the energy of a colliding photon is scattered through a small angle causing beam broadening. No energy is lost by the incident photon, thus this interaction does not contribute to the energy transfer coefficient, but still plays role in the attenuation coefficient. The probability of the coherent scattering σ_R / ρ is higher at low energies and larger Z values. The mass attenuation coefficient is proportional to $Z/(h\nu)^2$. Rayleigh scattering is significant for interaction energies less than 10 keV. For diagnostic spectra this interaction accounts only for 5% interactions.

2.2.2 Photoelectric effect

The photoelectric interaction occurs between photons and the tightly bound orbital electrons of a material, representing a combined action of the whole atom (Fig. 2.3). As a result of the interaction, the photon energy is transferred to an atom and a bound electron from the inner shell is ejected from the atom with a kinetic energy equal to the difference between the incident photon energy $h\upsilon$ and the binding energy of the ejected electron BE:

$$KE = h\upsilon - BE \ . \tag{2.17}$$

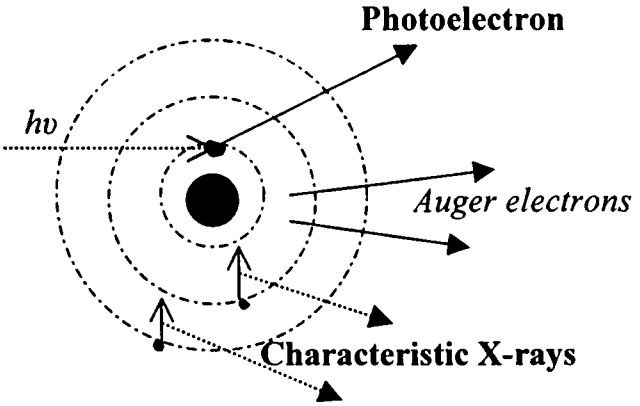

Figure 2.3. Photoelectric effect.

An outer shell electron fills the vacancy created by the ejected electron, giving rise to Auger electrons or characteristic radiation.

The mass attenuation coefficient of the photoelectric effect τ_m increases with decreasing photon energy $h\upsilon$ and with increasing Z of a material as $\left(Z/h\nu\right)^3$. The atomic attenuation coefficient ${}_a\tau$ is then proportional to $Z^4/(h\nu)^3$.

2.2.3 Compton effect

Incoherent or Compton scattering involves a photon interaction with a free and stationary orbital electrons with binding energy BE significantly less than the photon energy $h\nu$. This interaction results in the energy transfer from the photon to an electron. As a result of a collision a photoelectron is ejected at angle ϕ and a lower energy photon is scattered at an angle θ as shown schematically in Figure 2.4.

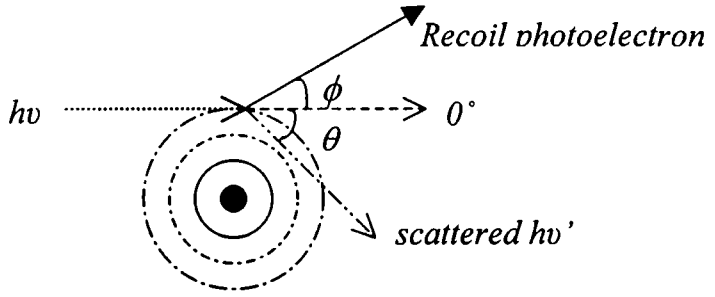

Figure 2.4. Compton scattering.

The energy of the scattered photon $h\nu'$ and the kinetic energy of the recoil electron KE_c are related to the scattering angle θ as follows:

$$h\nu' = h\nu \frac{1}{1+\varepsilon(1-\cos\theta)} \tag{2.18}$$

and

$$KE_c = h\nu \frac{\varepsilon(1-\cos\theta)}{1+\varepsilon(1-\cos\theta)} \quad , \tag{2.19}$$

where $\varepsilon = h\nu / m_e c^2$, $m_e = 0.511$ MeV/c^2 – electron rest mass.

Compton effect increases with the electron density of the attenuator but is independent of its atomic number Z, since it involves essentially free electrons in the absorbing material. The Compton mass attenuation coefficient σ_c / ρ decreases with an increase in photon energy. The Compton effect is the most important photon interaction in tissue-equivalent materials for the radiotherapy (megavoltage) range of photon energy.

2.2.4 Pair production

Pair production (Fig. 2.5) involves an interaction between a photon $h\nu$ and a nucleus as a result of which the photon disappears and its energy is transformed into an electron-positron pair with combined transferred kinetic energy (transferred energy E_{tr}):

$$KE = h\nu - 2m_e c^2 \quad . \tag{2.20}$$

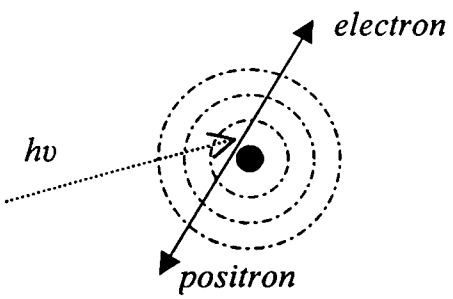

Figure 2.5. Pair production.

Since in the pair-production process, the mass of electron-positron pair is created out of photon energy, this interaction has a threshold of $2m_e c^2 = 1.02$ MeV. Generally, the kinetic energy is distributed evenly between the created particles. Usually after slowing down to thermal energies, the positron will annihilate with an electron, producing two 0.511 MeV photons, which are emitted in approximately opposite directions.

A similar interaction, referred to as triplet production, may occur in the vicinity of an orbital electron. Triplet production results in two electrons and one positron sharing the available energy. The threshold for this interaction is $4m_e c^2 = 2.04$ MeV.

The probability of pair production increases rapidly with photon energy above the threshold. The attenuation coefficient κ varies approximately as Z^2 per atom and Z per gram.

2.2.5 Photonuclear disintegration

Photonuclear disintegration occurs when a high-energy photon interacts with and is captured by the nucleus of an atom. As a result of the interaction the nucleus becomes unstable and undergoes a transformation by the emission of a neutron or proton. It is a less probable photon interaction compared to the atomic interactions described above and its contribution to attenuation coefficients can largely be ignored.

2.2.6 Relative importance of principal interactions

The probability of a specific type of photon interaction varies with photon energy $h\nu$ and atomic number of an attenuator Z. The graph in Figure 2.7 presents three regions

of relative predominance of the principal photon interactions: photoelectric effect, Compton effect and pair production.

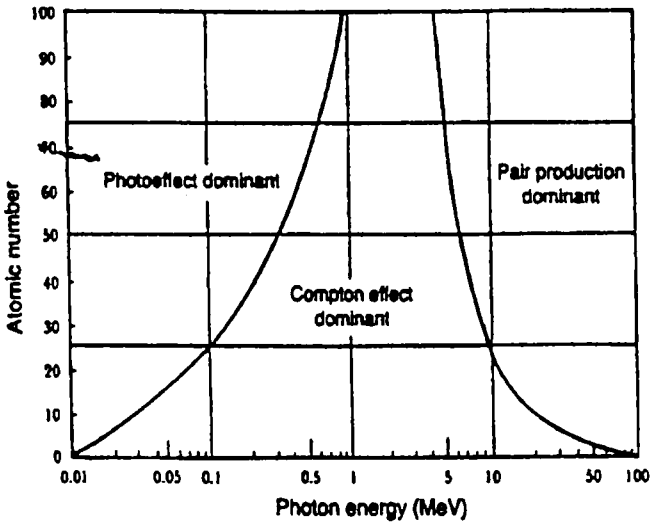

Figure 2.6. Relative predominance of principle photon interactions[12].

The two curves show the points with equal probability for the photon to undergo photoelectric or Compton interaction (${}_a\tau = {}_a\sigma_C$ - left curve) and Compton or pair production (${}_a\sigma_C = {}_a\kappa$ - right curve). One can see from the graph that for the radiotherapy energy region, the Compton effect predominates for soft tissue equivalent materials with $Z_{eff} = 7.5$.

2.3 Measurement of ionizing radiation and absorbed dose

In 1928, the International Commission on Radiological Units and Measurements adopted the Roentgen as a unit of exposure, which is measure of the ability of a radiation to ionize air. Exposure X is defined as:

$$X = \frac{dQ}{dm_{air}}, \tag{2.21}$$

where dQ is an absolute value of the total charge of the ions of one sign produced in air when all electrons liberated by photons in air of mass dm are completely stopped in air. The unit for exposure is a roentgen ($1R = 2.58 \times 10^{-4}$ C/kg air).

Another important dosimetric concept is kerma (kinetic energy released in the medium). Kerma describes the energy transfer from uncharged particles (photons) to a medium through setting charged particles in motion. It is expressed as

$$K = \frac{dE_{tr}}{dm} \quad . \tag{2.22}$$

The unit of kerma is J/kg. Kerma consists of two components: inelastic or collision kerma K^{col} and radiative kerma K^{rad}:

$$K = K^{col} + K^{rad} \quad . \tag{2.23}$$

Collision kerma K^{col} leads to the production of electrons that dissipate their energy as ionization near electron tracks in the medium. Radiative kerma K^{rad} leads to the production of bremsstrahlung as the charged particles are decelerated in the medium. Collision kerma and radiation kerma can be expressed using concepts of energy fluence Ψ, averaged mass energy absorption coefficient $\overline{\frac{\mu_{ab}}{\rho}}$ and averaged fraction of an electron energy lost to radiative process $\bar{g}$:

$$K^{col} = \Psi\left(\overline{\frac{\mu_{ab}}{\rho}}\right) \quad , \tag{2.24}$$

$$K^{rad} = \Psi\left(\overline{\frac{\mu_{ab}}{\rho}}\right)\left(\frac{\bar{g}}{1-\bar{g}}\right) \quad . \tag{2.25}$$

Collision air-kerma is directly proportional to exposure with proportionality factor $\overline{W}/e$:

$$\left(K_{air}^{col}\right)_{air} = X\left(\frac{\overline{W}}{e}\right) , \tag{2.26}$$

where $\overline{W}/e$ = 33.97 eV/i.p., representing the average energy required to produce one ion pair in dry air.

Absorbed dose D represents the energy absorbed in the medium from impinging radiation (energy not radiated away) per unit mass:

$$D = \frac{E_{ab}}{dm} . \tag{2.27}$$

The unit is the Gray, with 1 Gy= 1 J/kg.

Figure 2.7 represents the relationship between absorbed dose D and collision kerma K_{col} as a function of depth in the medium.

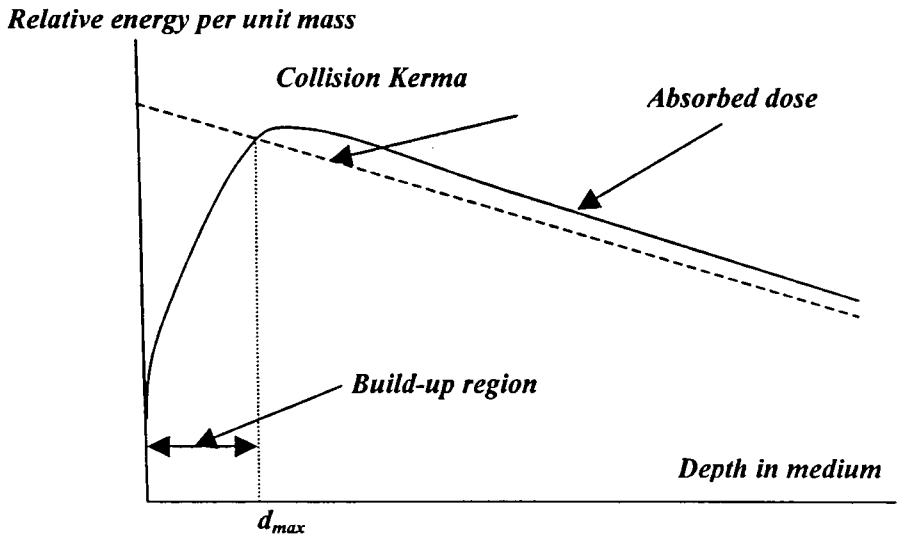

Figure 2.7. Collision kerma and absorbed dose as a function of depth in a medium.

Since radiative photons mostly escape from the volume of interest, one usually relates the absorbed dose to collision kerma. Kerma has a maximum value at the surface of the material, and then gradually decreases because of photon attenuation. Since the energy transfer (kerma) from the photon beam to charged particles at a particular

location does not lead to the absorption of energy by the medium (absorbed dose) at the same location, the absorbed dose for a megavoltage beam as a function of depth is at first much smaller than kerma and then builds up through the electron build-up region until a maximum value occurs at the depth of dose maximum d_{max}. This is due to non-zero range of energetic secondary charged particles, which were first released through photon interactions and then transfer their kinetic energy to the medium. At the depth of d_{max}, which is comparable to the range of secondary electrons, absorbed dose D is equal to collisional kerma. The conditions of the charged particle equilibrium (CPE) are present at this depth: each charged particle of a given type and energy leaving the volume of interest V is replaced by an identical particle entering the volume. In the region beyond d_{max}, absorbed dose is directly proportional to the collision kerma and decreases due to photon attenuation at the same rate as kerma. This region is referred as the region with transient charge particle equilibrium (TCPE).

2.3.1 Ionization chamber dosimetry

To monitor the dose in the medium, gas-filled dosimeters called ionization chambers are used. They measure ionization in their own medium (gas-filled cavity) but those readings are in direct relation to the dose to the surrounding medium.

The Bragg-Gray cavity theory relates the ionization produced in a gas-filled cavity to the energy absorbed in the surrounding tissue. The theory assumes that the cavity is small enough compared to the range of charged particles crossing it that it does not perturb the particle fluence which would exist in the medium without the cavity. The ionization in the cavity is caused entirely by the charged particles crossing the cavity. The particles originate in the surrounding medium. When the Bragg-Gray conditions are

fulfilled, the following relationship for absorbed dose in the medium D_{med} without the cavity is satisfied:

$$D_{med} = J_{gas}\left(\frac{\overline{W}}{e}\right)_{gas}\left(\frac{\overline{S}}{\rho}\right)_{gas}^{med}, \tag{2.28}$$

where J_{gas} is the ionization charge of one sign produced per unit mass of cavity gas. The product $J_{gas}\left(\frac{\overline{W}}{e}\right)_{gas}$ is the energy absorbed per unit mass of the cavity gas. $\left(\frac{\overline{S}}{\rho}\right)_{gas}^{med}$ is the mean ratio of the mass stopping power of the medium to that for the cavity gas for electrons crossing the cavity.

The "primary electrons" (electrons generated by photons) give rise to ionization as well as to secondary electrons, but the Bragg-Gray theory does not account for the effects of secondary electrons produced. Spencer-Attix cavity theory relates the dose delivered to the gas in the ion chamber to the dose in the surrounding medium, D_{med} and accounts for the secondary electrons by using $\left(\frac{\overline{L}}{\rho}\right)_{gas}^{med}$, the mean ratio of restricted mass collisional stopping power of the medium to that for the cavity gas with a cutoff energy limit Δ:

$$D_{med} = J_{gas}\left(\frac{\overline{W}}{e}\right)_{gas}\left(\frac{\overline{L}}{\rho}\right)_{gas}^{med}. \tag{2.29}$$

The Spencer-Attix cavity theory assumes that the cavity does not perturb the electron spectrum in the medium and that all ionizations in the cavity come from the electrons entering the cavity from the surrounding medium. The theory states that electrons with energies below a cutoff energy Δ deposit their energy locally and they will not contribute to the dose in the cavity. The electrons with energy above Δ are able

to cross the cavity and deposit energy in the cavity. The value of Δ for most ionization chambers lies between 10 and 20 keV.

2.3.2 Absorbed dose in the medium (TG-51 calibration protocol)

Recently a new protocol for clinical reference dosimetry of external beam radiation therapy has been developed by the AAPM Task Group 51 (TG-51)[13] to replace the previous protocol (TG-21)[14]. The TG-51 protocol is based on an absorbed dose to water calibration coefficient in ^{60}Co beams ($N_{D,W}^{60Co}$) and an energy-dependent correction factor, k_Q. However, the TG-21 protocol is based on an exposure (air kerma) standard and multiple energy-dependent correction factors. Our accelerators are calibrated based on the TG-51 protocol. This protocol allows determining absorbed dose to water at the point of measurement of the ionization chamber placed under certain reference conditions.

The main equation to determine absorbed dose from photons in water in the TG-51 protocol is:

$$D_W^Q = M k_Q N_{D,W}^{60Co} \quad , \tag{2.30}$$

where Q is the beam quality of the clinical photon beam for which clinical reference dosimetry has been performed. In our experiment we have been using two beam energies – 6 MV and 18 MV.

D_W^Q is the absorbed dose to water for a given number of monitor units.

k_Q is the quality conversion factor, which converts the calibration factor for a ^{60}Co beam to that for a beam of quality Q.

M is fully corrected ionization chamber reading, corrected for ion recombination, environmental conditions, polarity effects, inaccuracy of electrometer and polarity effects. M can be expressed as:

$$M=P_{ion}P_{TP}P_{elec}P_{pol}M_{raw}\ , \tag{2.31}$$

where M_{raw} is the raw, uncorrected ionization chamber reading in coulombs, C.

P_{ion} (the recombination correction factor) corrects for incomplete ion collection efficiency.

P_{TP} (the temperature-pressure correction factor) makes the charge or measured current correspond to the standard environmental conditions: $T=22\ ^{o}C$, $P=101.33\ kPa$.

P_{elec} (the electrometer correction factor) corrects the electrometer reading to true coulombs if the electrometer is calibrated separately.

P_{pol} (the polarity correction factor) takes into account any polarity effect in response of the ionization chamber.

Chapter 3.

Equipment

The significant advances made in cancer treatment over the last decades can be attributed partially to the development of improved radiotherapy equipment. Modern conventional simulators, CT scanners and medical accelerators provide the capability for very precise tissue localization and accurate dose delivery to the target volume. This chapter discusses the equipment used at different stages of the clinical process as well as some historical aspects of the development and principles of operation of this equipment.

3.1 Simulators

3.1.1 Conventional simulators

Modern radiation therapy treatment is a sophisticated multi-step process which begins with defining and localizing the volume of the tissue to be treated with radiation and the organs at risk to which the dose should be limited. Once the planning target volumes and critical organs are defined, the radiation beams should be aimed properly at the treated tissue volume.

One of the main concerns in radiotherapy is to ensure the appropriate beam placement on the patient. For this purpose a conventional simulator is used. The first conventional simulators appeared in the beginning of the 1960s, almost at the same time as the first isocentrically mounted linear accelerators[4]. Simulators were introduced into radiotherapy clinical process to remove the time consuming aspects of treatment

planning and patient setup from needing to be done on very expensive radiotherapy machines. A conventional simulator allows the exact geometric simulation of a linac. A rotating gantry, collimating system and couch replicate the geometry of a megavoltage treatment unit (Fig. 3.1).

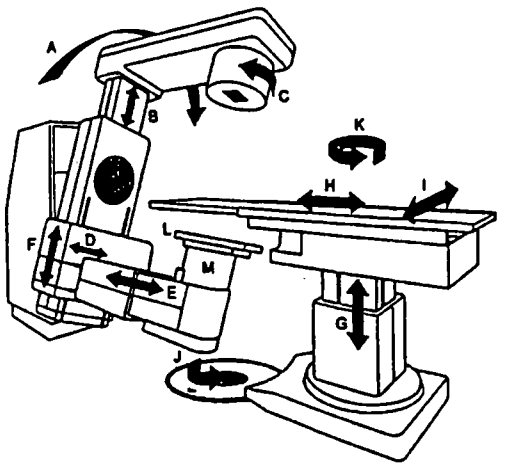

Figure 3.1. The basic components and motions of a radiation therapy simulator[15].

A, gantry rotation; B, source-axis distance (SAD); C, collimator rotation; D, image intensifier (lateral); E, image intensifier (longitudinal); F, image intensifier (radial); G, patient table (vertical); J, patient table (longitudinal); I, patient table (lateral); J, patient table rotation about isocenter; K, patient table rotation about pedestal; L, film cassette; M, image intensifier.

In modern simulators the source-axis distance (SAD) can vary from 80 up to 150 cm[15]. Full rotation of the gantry is possible for SAD up to 100 cm. Distances greater than 100 cm allow simulating treatment fields that are larger than 40x40 cm^2, such as in Hodgkin's disease patient simulation. In some situations the combined rotation of both the gantry and the treatment couch can be limited because of the interference of the large image intensifier. In those cases a CT scanner and virtual simulation process help to solve the problem.

The simulator couch is similar to the one on the treatment machine and mimics the geometry of its motion for identical patient positioning on both units. Three optical

systems are used to provide accurate patient positioning and beam alignment. The simulator light field outlines the radiation field and crosshairs indicate its center; an optical distance indicator (ODI) shows source-surface distance (SSD) or source-axis SAD; four ceiling- and wall-mounted laser positioning lights are used to indicate the isocenter.

Images produced by a simulator have better contrast than verification films from treatment machines. The X-ray tube of the simulator is a source of diagnostic X-rays which have a range of energies where photoelectric interactions that are dependent on atomic number dominate. A typical design of an X-ray tube is presented in Figure 3.2.

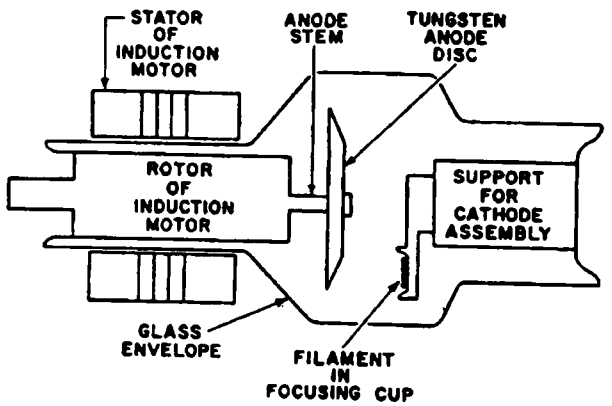

Figure 3.2. The major components of the X-ray tube with rotating anode[16].

X-rays are produced when electrons are boiled off a tungsten cathode filament (thermionic emission) and are accelerated across a vacuum tube to bombard a positively charged tungsten target (anode). A high voltage generator provides the X-ray tube with high DC voltages. The generator converts the low line AC voltages to much higher AC voltages and then converts the AC voltage into a DC voltage through a rectification process. An X-ray tube operates at high instantaneous currents of up to 800 mA. To avoid target overheating the rotating anode is used to spread the heat over a circumference of 30 cm. The simulator can operate in a radiographic mode and an image

can be obtained on the X-ray film or in fluoroscopy mode, providing real time monitoring on the cathode ray screen. Since the fluoroscopy exposure takes longer than a single radiographic exposure, a larger focal spot is used in this mode to prevent target overheating.

The patient simulation procedure on the conventional simulator demands relatively long x-ray exposures. In order to keep the total x-ray dose low, each of the fluoroscopic images is made with a relatively low exposure. Because of the small number of X-rays used to build up each fluoroscopic image, X-ray detectors must be very sensitive. An X-ray Image Intensifier (II) provides the capability to produce a bright image without giving to a patient an excessive radiation exposure. The components of an II are shown in Figure 3.3.

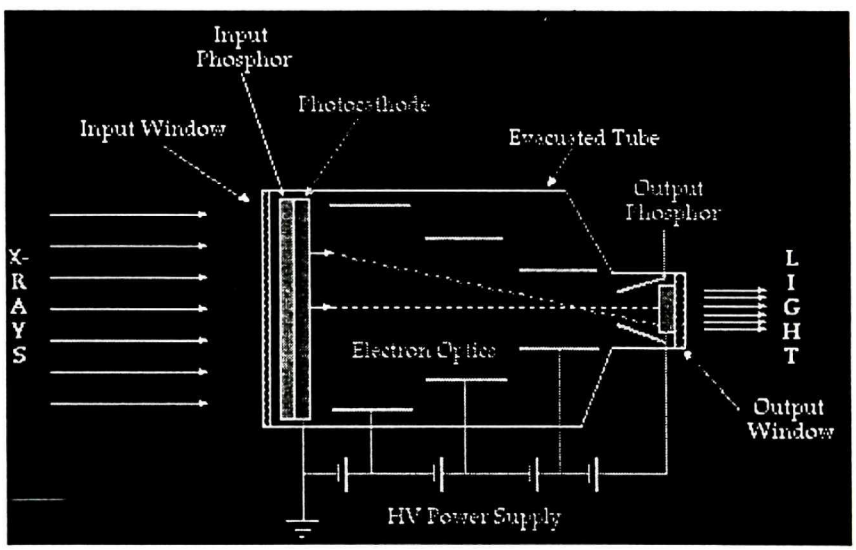

Figure 3.3. Image intensifier[17].

Usually the II tube is a cylindrically shaped evacuated glass envelope, containing several basic elements. After an X-ray passes through the patient, it enters the input window and strikes the input phosphor.

In modern image intensifiers the input window is made of a relatively thin sheet (e.g., 0.25 - 0.5 mm) of aluminum or titanium that can prevent X-ray scattering and

minimize attenuation effects while still having a good strength for containing the vacuum. The fluorescent input screen absorbs X-rays and converts their energy to light photons. The input phosphor is typically 15 to 40 cm in diameter, depending on the II. It is made of CsI, doped with Na, which is deposited on an aluminum substrate. Both cesium and iodine are good absorbers at diagnostic x-ray energies having K-edges at 36 and 33 keV, respectively. Screens made of these materials absorb approximately two thirds of the incident beam and provide good results compared to other materials. The photons from the fluorescent input phosphor strike the photocathode, which emits electrons. The photocathode is a photoemissive material and typically consists of an alloy of antimony and cesium. The number of photoelectrons released via the photoelectric effect in the photocathode is proportional to the brightness of the screen. Emitted electrons are accelerated in the vacuum with the help of high potentials of 25 kV to 35 kV and acquire large velocities. The electron beam is focused by electrostatic focusing lenses (electrodes) as it flows toward the output phosphor, which emits a green light when it absorbs the accelerated electrons. The output phosphor is made of silver-activated zinc-cadmium sulfide (ZnCdS: Ag). A typical fluorescent screen is 0.005 mm thick and 25 to 35 mm in diameter. A thin aluminum film is plated on the inner surface of the phosphor, which serves both as the anode and to prevent light moving back towards the output window. Image magnification can be controlled by varying potentials on the electrostatic focusing lenses. Electron beam acceleration and focusing give rise to the image intensification, which increases up to 50 times compared to the case when an intensifying screen is used on its own.

The secondary phosphor light image can be viewed either directly through a series of lenses and mirrors or captured with a video camera and presented on a monitor.

In modern systems a frame grabber is used to digitize and record the electronic signal from video camera. The digitized images and relevant simulator setup parameters are stored in the computer and than analyzed to plan radiotherapy beam placement. The range of organ movement during the respiration cycle can also be estimated.

Introducing conventional simulators into medical practice gave numerous advantages compared to the use of megavoltage beams from treatment units for verification films. Among those advantages are: improved image contrast, reduced dose to the patient, the possibility to make beam adjustments in real-time and to conserve very expensive treatment unit resources.

3.1.2 CT Simulators

A new era of medical imaging began in April 1972 when a new imaging technique called "computerized axial transverse scanning" was introduced. This revolutionary discovery was a product of intensive research work of numerous investigators. Computed tomography (CT) is the modern name for a technique that has combined a conventional tomographic procedure with computer technology. The basic principle behind the CT is that the internal structure of the object can be reconstructed from multiple X-ray projections. X-ray beams at different angles irradiate a single thin cross-section of the human body and the transmitted intensity values are detected and sent to a computer for analysis by a mathematical algorithm. In this way the entire volume of interest is scanned and, from the projection information, image reconstruction generates a cross-sectional image matrix up to 1024x1024 pixels* in size[4]. In this matrix each pixel is an accurate measure of the relative linear attenuation coefficient at

* Pixel is the smallest unit of an image, one of the dots that make up a screen picture.

diagnostic energies. The pixel values are measured in CT numbers and displayed by grey levels. A CT number is defined as:

$$CT\ number = 1000 \times \frac{(\mu_{medium} - \mu_{water})}{\mu_{water}}\ , \qquad (3.1)$$

where μ_{medium} and μ_{water} are linear attenuation coefficients of medium and water, respectively.

The data-gathering techniques have undergone significant technological evolution since the mid-1970s when CT became commercially available. The stages of the technique development are called "generations".

The first generation scanner employed a single pencil-like X-ray beam and an X-ray detector cell to collect all data for a single slice (Fig. 3.4).

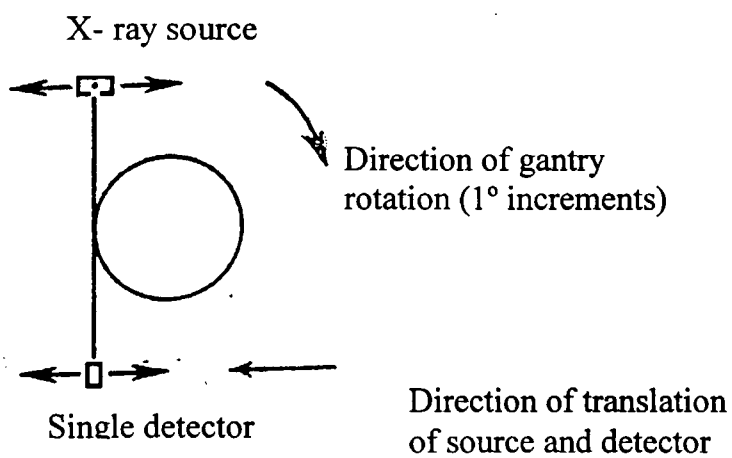

Figure 3.4. First Generation as originally developed by EMI Ltd in 1972[18].

The source and detector were rigidly coupled and the pencil beam was translated across the patient to obtain a set of parallel projection measurements at one angle. The X-ray tube-detector movements were both linear and rotary. The gantry was rotated at increments of 1° and the linear motion procedure was repeated until 180 distinct views were obtained. This was a very time-consuming method because of the numerous

mechanical movements required. A time of about 4-8 minutes was required in order to obtain images of two contiguous sections. Because of the translation and rotation process, this geometry is referred to as a translate/rotate method.

One of the main objectives of the scans of the "next" generation was to perform the scanning sequence in a reasonable time. Since the X-ray source emits radiation over a large angle, the efficiency of measuring projections was greatly improved by using multiple detectors. The source and the array of detectors are translated as in the first generation system, but due to the implementation of 30 beams with a separation of 1/3°, a single traverse of the system was able to register 30 distinct views. That means that rotation between translations was increased to 10° and the number of repetitions of linear movements has decreased to 18. This generation, similarly to the first one, is referred to a translate/rotate method (Fig. 3.5).

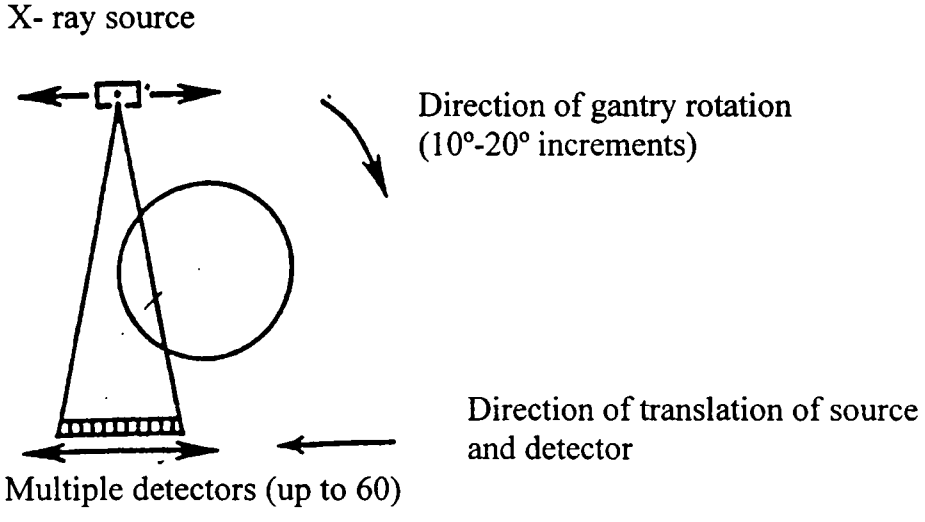

Figure 3.5. 2nd Generation employing multiple beams to increase scanning speed[18].

The second generation scanners are significantly more efficient and faster than the original first generation scanners due to their ability to acquire multiple projections

each traversal past the patient. As a result of employing the fan beam array of detectors, the scan time decreased from 4 minutes (first generation) to 20 seconds.

In 1975 the General Electric Company introduced the scanner in which the translational motion was completely eliminated. A wide-angle fan-beam (40°-50°) was employed with a large array of detectors (Fig. 3.6). The improvements in detector and data acquisition technology made it possible to design a detector array with a high enough spatial resolution to allow the simultaneous measurement of a fan-beam projection of the entire patient cross-section.

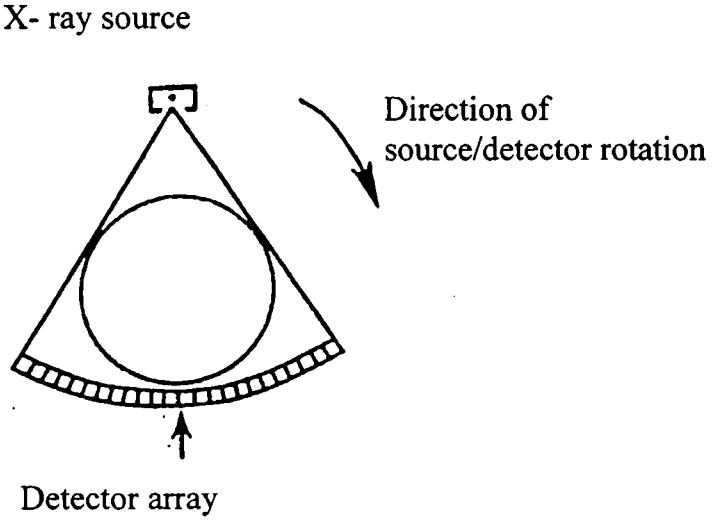

Figure 3.6. 3rd Generation rotate-only system in which the X-ray tube and the detectors both move around the patient[18].

With such a large detector area it is no longer necessary for the X-ray tube-detector assembly to translate past the patient; instead, it simply rotates around the object. Third generation scanners are often referred to as using a rotate/rotate scanner geometry, because of the tube and detector rotation. The scanning time is significantly decreased, but the system is more sensitive to aliasing than the first or second generation scanners and may produce images with ring artifacts.

In order to solve these problems a new (fourth) generation of scanners has been developed (Fig. 3.7). In this design a stationary detector ring surrounds the patient and the X-ray tube is the only rotating part. Fourth generation scanners are referred to as using a rotate/fixed geometry. Both the third and forth generation scanners reduced scanning time to as low as one second.

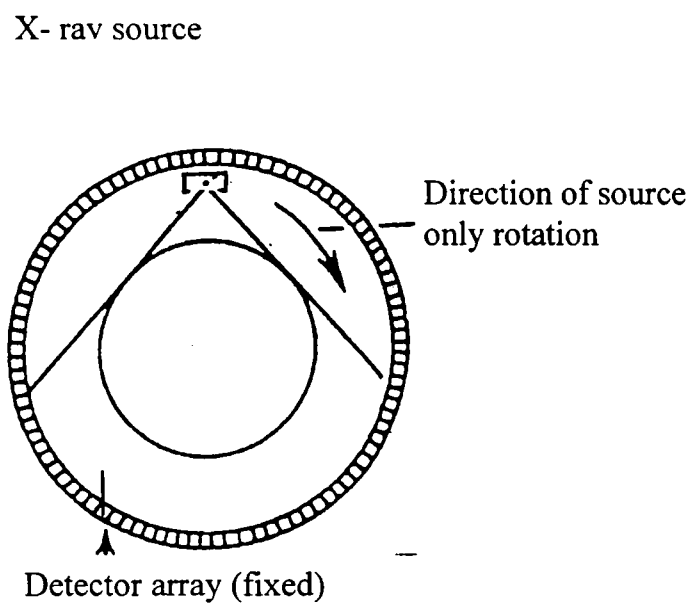

Figure 3.7. 4th Generation, in which the detectors are fixed and the X-ray tube is the only moving component[18].

The fourth generation scanners are not sensible to ring artifacts. But because the stationary detectors have a larger acceptance angle for radiation, they are more sensitive to scattered radiation, compared to the 3rd generation scanners. Fourth generation scanners require a larger number of detectors and electronic channels in order to achieve the same spatial resolution and dose efficiency as the third generation scanners. This increases the cost of the fourth generation scanners in comparison to the third generation scanners.

Recently several other CT scanner geometries have been developed and marketed. These systems do not precisely fit the above categories; however, there is no agreed-upon generation designation for them yet[19].

The rotate-nutate scanner has a circular detector ring which is inside the source trajectory. The scanner gantry is more compact due to the reduced size of the detector array. In these systems, the detector array nutates so that the detectors do not obstruct the X-rays as they pass from the source to the object. Another geometry is the cine CT system where there is no mechanical scanning motion; both the X-ray detector and the X-ray tube anode are stationary. Instead, it has a very large semicircular anode ring that forms an arc around the patient, as part of a very large, non-conventional X-ray tube. In this system the electron beam is steered around the same path as in a fourth generation CT scanner. This scanner can reach very rapid image acquisition rates because the electron beam can be moved very rapidly.

Another development is the slip-ring technology implemented in spiral (helical) scanners, which permits continuous rotation of the X-ray tube as the patient is slowly translated through the scanner. The rate of image acquisition is very high for the slip-ring scanners. They can attain sub-second rates, which make their implementation extremely useful in the studies of organs that are subjected to movement while breath-hold technology is applied. Up to 40 slices can be acquired during one breath-hold. This type of scanner has been used in our project for patient simulation during breath-hold.

The modern CT-Simulator (Fig. 3.8) combines a conventional diagnostic CT scanner, an additional computer graphics workstation with virtual treatment software and a laser alignment/marking system.

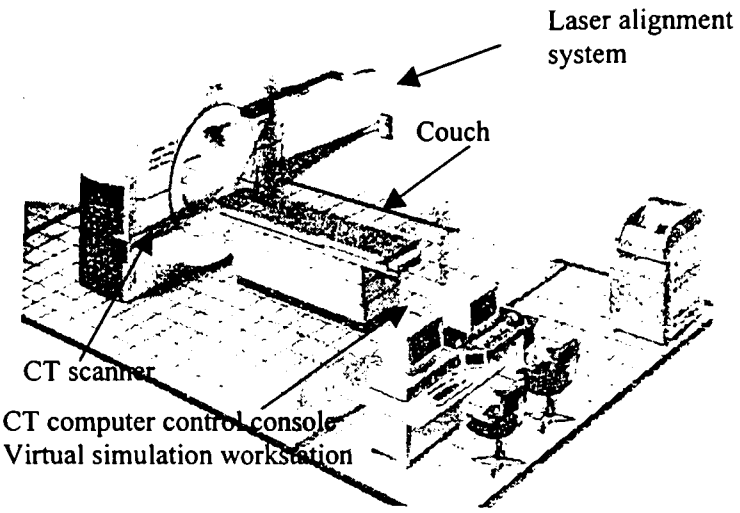

Figure 3.8. The major components of a CT Simulator[15].

A CT simulator scanner should meet special requirements to perform the specific tasks of simulation. Because of the importance of 3-D reconstruction accuracy and the need to generate high quality digitally reconstructed radiographs (DRRs), the number of slices per study is significantly increased. As a result the scanner's X-ray tube should have a higher rating, i.e., higher heat load capacity than conventional CT scanners. In addition, the accuracy of the image geometric scales, couch positioning and alignment to the scan plane are very important for the 3-D reconstruction process and require special consideration. For the CT simulator scanner, couch registration accuracy should be better than 0.5 mm for maximum load.

The CT-simulation process starts with patient positioning using a four-laser alignment system, which provides lateral, horizontal, vertical and sagittal lines. For the flexibility of patient setup the scanner should have the largest possible physical aperture diameter. Modern CT-simulator scanners have aperture sizes of 68-85 cm and circle of reconstruction (field-of-view) sizes of 48-50 cm. The CT scanning/acquisition of patient

data is a crucial step of the simulation process. Future treatment depends on the data obtained during this stage and errors or uncertainties could significantly affect treatment planning results. The scan region should be defined very carefully to encompass all the anatomical structures, which are necessary for DRR reconstruction and dose volume histogram (DVH) calculation. Slice thickness and pitch factor are very important imaging parameters. Despite the fact that image quality can be improved by decreasing slice thickness, this parameter should be chosen taking into account increased tube loading and additional reconstruction and contouring time for thinner slices.

Subsequently to the CT scanning procedure there is a three-dimensional planning process that helps visualize the tumor tissue directly in 3D space. Our deep inspiration breath-hold (DIBH) gated technique planning procedure is similar to standard treatment planning and consists of the following main steps: structure delineation, beam placement and calculation of an isodose distribution.

The radiation oncologist first delineates the tumor and critical organ structures by outlining them on a CT scan. A Planning Target Volume (PTV) is also delineated on each scan. The margins for this volume usually include consideration for all possible geometrical variations (e.g., set-up, movement). The Clinical Target Volume (CTV), which includes demonstrable malignant growth, gross tumor volume (GTV) and microscopic disease, is incorporated within the PTV volume[5]. When this procedure is done, a three-dimensional conformal plan is designed and various geometrical calculations are performed.

The second step, after creation of three-dimensional graphical structures, is a virtual simulation or beam placement. This procedure is performed using a piece of software called the Virtual Simulator, which is intended to replace a physical simulator.

During this procedure such parameters as the SSD, table and collimator settings as well as gantry position are obtained.

After the optimal beam geometry has been selected, the information is transferred to a treatment planning computer where dose distributions and the isodose pattern are calculated and displayed.

CT-simulation offers several advantages over conventional simulation. The system provides 3-D imaging capability and CT number/electron density information that can be used for dose calculation. The system software enables the automatic outlining of treatment volumes, external contours and critical structures, with interactive treatment field display and placement, display of dose distribution, and review of multiple treatment plans. The patients need only be present for the CT scan and are spared from the subsequent simulation process since their electronic data are used for the simulation. All of these features of the modern CT-simulator provide a greater level of treatment accuracy and patient comfort.

3.2 Megavoltage medical linear accelerators

The microwave-powered electron linear accelerator (linac) has become the dominant radiotherapy treatment unit in the world. In North America medical linacs now comprise almost all of newly installed teletherapy units. Numerous technical advances in linacs have led to continuing improvements in linac radiotherapy during more than four decades since their first introduction in the early fifties[20]. During their technological evolution medical linacs have gone through five distinct generations[21]. First generation linacs produced low energy photon beams (4-8 MV) and were equipped with a simple collimating system – symmetric jaws and external wedges and just a single transmission ionization chamber. With each stage of technical development of medical linacs, more sophisticated and advanced features were introduced into the design. The modern generation of linacs has an increased number of electron and photon energies with possible dose rates of 800 MU/min in photons and 1000 MU/min in electrons. They are capable of photon beam shaping and intensity modulation with a multileaf collimator, pulse-to-pulse beam control for dynamic treatments and beam gating support.

All the dosimetry experiments presented in this work were conducted using a high energy (up to 18 MV) linear accelerator (Clinac 2100 C/D manufactured by Varian Medical Systems Palo Alto, California). A photograph of our linac is shown in Figure 3.9.

A medical linac consists of five basic operating components (Fig. 3.10). In the injection system or so-called electron gun, a simple electrostatic accelerator (diode or triode) is the source of electrons. Particles are thermionically emitted from the heated cathode, focused, and accelerated toward the waveguide entrance. The electrons possess

a sufficiently high initial energy to be captured and accelerated by unmodulated RF field in the waveguide. The RF system, including RF power source (magnetron or klystron), pulsed modulator, control unit, accelerating waveguide and a circulator, is responsible for electron acceleration. Electrons are transported from the accelerating waveguide to the target or scattering foil with the help of a bending magnet and steering and focusing coils which are components of the beam transport system. The role of the auxiliary system is to maintain vacuum in a waveguide, air pressure in pneumatics and support the water cooling and dielectric gas systems. The beam collimating and monitoring system is involved in producing, shaping, localizing and monitoring clinical beams.

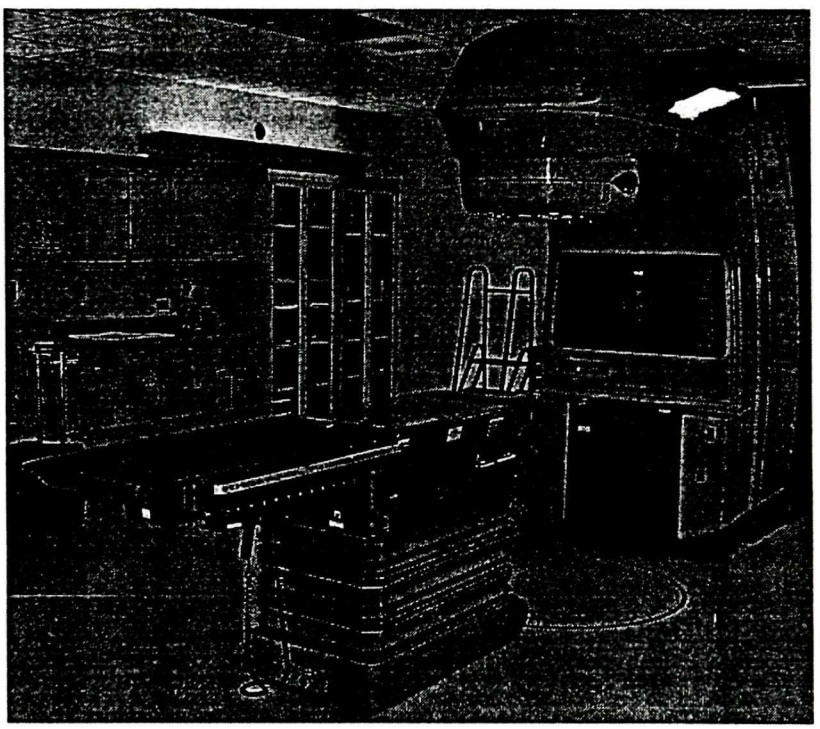

Figure 3.9. High Energy Clinac 2100 C/D with Multileaf Collimator and Portal Vision Imager.

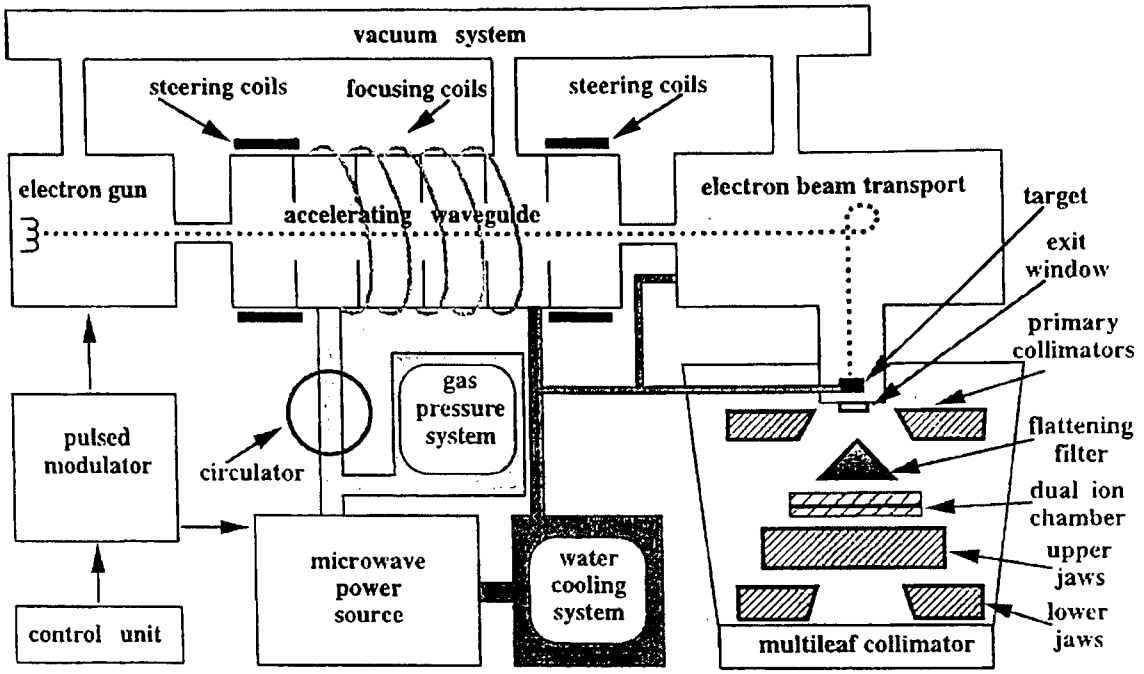

Figure 3.10. Block diagram, illustrating the main parts and component systems of Linac[21].

Below is a more detailed description of the main features and characteristics of a linac.

Accelerating waveguide

The central component of the linac is the microwave accelerator structure – the accelerating waveguide, where charged particles (electrons) are accelerated to high energies by high frequency electromagnetic waves. Microwave propagation through the uniform waveguides is governed by Maxwell's equations:

$$\vec{\nabla} \bullet E = \frac{\rho}{\varepsilon_o} \quad , \tag{3.1}$$

$$\vec{\nabla} \bullet B = 0 \quad , \tag{3.2}$$

$$\vec{\nabla} \times E = -\frac{\partial B}{\partial t} \quad , \tag{3.3}$$

$$c^2 \vec{\nabla} \times B = \frac{j}{\varepsilon_o} + \frac{\partial E}{\partial t} \quad , \tag{3.4}$$

where E and B are electric and magnetic fields, ε_o is the dielectric constant for vacuum, ρ and j are the charge and current densities respectively.

Propagation of microwaves should satisfy the boundary conditions on the interfaces between metallic walls and dielectric material inside, which demands that the tangential component of the electric field and the normal component of the magnetic field be equal to zero.

A typical waveguide used in a high-energy linac is an evacuated copper cylindrical tube with a series of cavities. These structures play a very important role in electron acceleration. In order to be accelerated by the electric field, electrons should possess the speed v_{part}, which is equal to the phase velocity of the electric field v_{ph}. However, in the absence of cavities in the uniform waveguides v_{ph} exceeds the speed of light in vacuum. Since a particle's speed cannot exceed the speed of light, acceleration of charged particles in a uniform waveguide would be impossible. To slow down the phase velocity of the electric field v_{ph} below c, equidistant perturbations are added along the tube in the form of disks with small holes in the center, thus forming a non-uniformly loaded waveguide. These disks divide the tube into cylindrical cavities with typical diameters about 10 cm and lengths of 2.5-5 cm[21]. There are two types of accelerating waveguides used for particle acceleration: traveling wave structures and standing wave structures (Fig. 3.11).

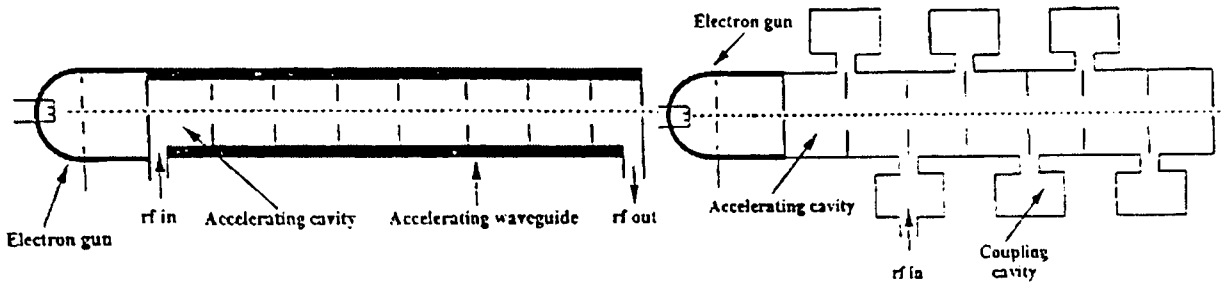

a) b)

Figure 3.11. Schematic diagrams of a) traveling wave accelerating waveguide; b) standing wave accelerating waveguide[21].

In the traveling wave structure, high frequency microwaves are transmitted in the evacuated waveguide tube through evenly spaced accelerating cavities with length $\lambda/4$ (about 2.5 cm), then they are absorbed in a resistive load at the end of the guide which prevents them from reflecting and interfering with incoming waves or they are fed back into the input end of accelerating waveguide. For this structure energy transfer of 5 MeV/m is typical.

In a standing wave structure microwaves traveling toward the high energy end of the waveguide are reflected by the conducting disk with a $\pi/2$ phase change. As a result two traveling waves of equal amplitude and period travel through the waveguide in the opposite directions form a standing wave. In this structure every second cavity carries no electric field at all times. To enable electrons to experience acceleration through each accelerating cavity and effectively reduce the traveling distance – coupling cavities (with no electric field) are moved outside of the waveguide structure. The typical energy transfer in a standing wave structure is about 20 MeV/m. RF power in this structure can be delivered at any convenient point along the accelerating waveguide, which is opposite to the traveling wave structure where RF supply is restricted to the low energy end of the

waveguide. Despite the fact that the standing wave structure yields higher energy transfer per unit length compare to the traveling wave structure; the former demands a higher RF power (25% more) for operation.

The operational frequency of the accelerating waveguide is 2856 MHz (S-band). The basic mode is transverse magnetic TM_{01} in which electric field has a component in the direction of electron propagation.

The length of standing wave structure accelerating waveguides (typically used in Varian Linacs) depends on the final electron energy. It varies from 30 cm in length for 4 MeV electron energies up to 150 cm for 25 MeV. The dimensions of low energy waveguides (4-6 MeV) allow direct isocentric mounting with the accelerating waveguide integrated directly into the gantry head. The intermediate and high-energy treatment units employ a horizontally mounted standing wave accelerator structure. In these cases the waveguide is usually placed either in the gantry or in the gantry stand parallel to the gantry axis of rotation.

One of the distinctive features of the Clinac 2100's waveguide is its ability to generate both low (6 MV) and high (18 MV) X-rays. This is accomplished by employing an energy switch – a device that shortens the accelerating length of the waveguide by approximately 1/3. The switch consists of a pneumatically driven copper pin that penetrates into the evacuated waveguide cavity through special bellows.

In order to keep the beam traveling down the axis of the waveguide both the beam angle and beam position must be controlled from the moment the beam enters the waveguide. The main four reasons for the beam not traveling along the central axis of the guide are the imperfections in the accelerator structure and the gun alignment, the presence of a small component of radial electric field and the effects of external

magnetic fields (Earth's field and fields due to the presence of steel in treatment room environment and effect of electron repulsion due to the electrostatic forces).

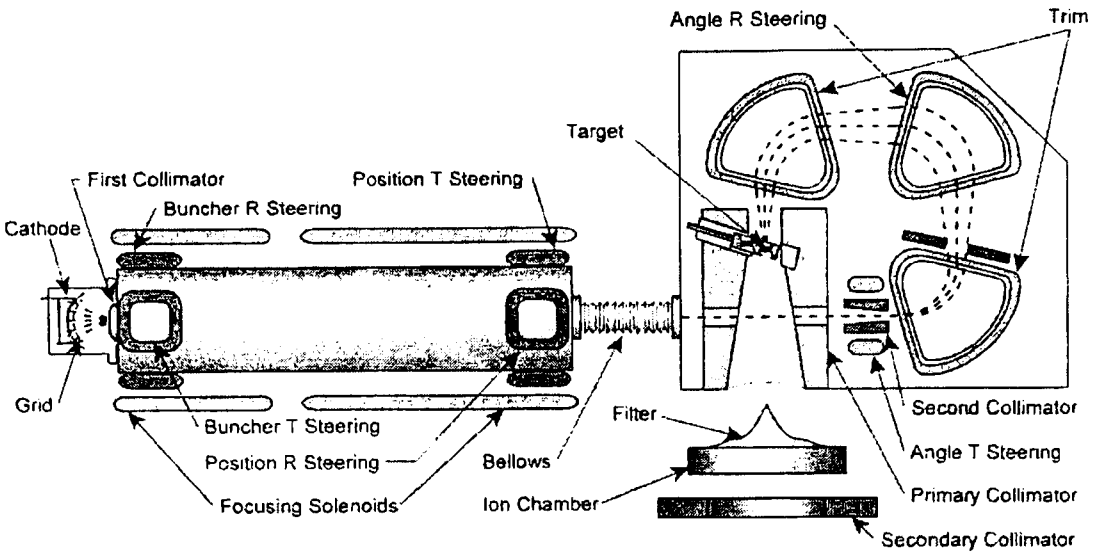

Figure 3.12. The steering coil placement of the accelerator[22] .

Thus, the electron beam must be actively steered through the waveguide. This is achieved by the use of two sets of steering coils, each containing four coils, mounted at the both ends of the waveguide (Fig. 3.12). Coils at the gun end are responsible for buncher radial and transverse steering; target end coils achieve radial and transverse position steering. Also, the waveguide is coaxial with and placed inside the two focusing solenoids at each end of the waveguide. The focusing magnetic field prevents electrons in the beam from diverging and also defines the required size of the beam in the drift tube before it enters the bending magnet structure. Mechanically, the waveguide and the focusing coils comprise a single unit, since the accuracy of their mutual positioning is very critical for the linac operation. To compensate for mechanical shifts due to the dissipation of heat in the coils they are constantly cooled by the accelerator's internal water cooling system.

Electron Gun

The source of the treatment beam in a linac is an electrostatic accelerator – a triode or diode type electron gun. Both types of electron guns contain a thermionic tungsten-based cathode as an emitter of electrons, and a grounded anode. A triode type gun incorporates a grid to control the electron emission (Fig. 3.13).

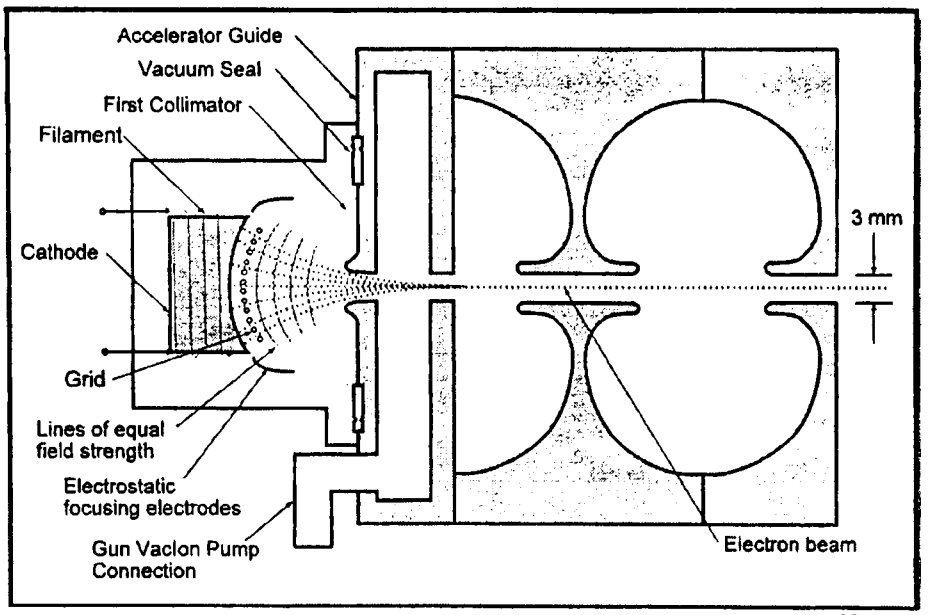

Figure 3.13. Schematic view of high-energy Clinac electron gun[22].

The Clinac 2100 C/D employs a triode type electron gun with an indirectly heated dispenser cathode. Electrons are thermionically emitted from the cathode, focused into a pencil beam by electrostatic focusing electrodes and accelerated toward the grounded anode.

Accelerator's waveguide system operates at the ground potential with the electron gun cathode, supported on a ceramic structure, at up to -25 kV. This voltage defines the initial energy of the electron beam injected into the waveguide. The control grid is held at a potential negative to the cathode, which makes it possible to control the timing and amplitude of beam pulses by applying voltage pulses to the grid. Voltage applied to the grid can vary between – 150 V and + 180 V with respect to the cathode.

Electron gun current is equal to zero when voltage of – 150 is applied to the grid and increases as the grid potential becomes more positive. In order to maintain the constant energy of electrons at the target end of the waveguide, a 1-2 μs delay is employed between the microwave pulse and the injection of the beam. The delay provides time needed for a standing wave to be fully established in the waveguide.

Most tungsten cathodes operate at a temperature reaching 1800° C and the embedded electron emitter is thorium. However, in most guns, this temperature would melt the grid. To solve this problem, finely ground particles of barium are distributed evenly within the tungsten cathode, allowing the cathode to operate at a lower temperature. When the temperature reaches 714° C (the melting point of barium) the particles migrate to the surface, where they form a thin film. As the surface barium is used up, more barium is "dispensed" from within the cathode to the surface, hence the name "dispenser cathode."

A unit called the "gun driver" is dedicated to operate the gun. Controlled by a microprocessor, it incorporates several power supplies, diagnostic circuitry and a control device. It is used to control all parameters of the electron gun, including gun filament current, amplitude and timing of control grid pulses, gun voltage, etc. This is needed when switching between different energies and modes of operation of the linac, which require different gun settings.

Bending magnet

A 270° bending magnet performs "achromatic" bending of the electron beam, so that electrons that emerge from the magnet will strike the target or foil at the same point and in the same direction, independent of their energy at the entry point of the magnet. This is achieved due to the design of the magnet. Electrons entering the bending magnet with higher speeds penetrate further into the magnetic field, thus becoming subject to a stronger field, which leads to shortening of their orbit (Fig. 3.12).

Target and flattening filters

When a pencil-shaped beam of electrons strikes the target three different types of interactions can occur: collisional, radiative and scatter. As a result of collisional losses electron energy is deposited as heat. To avoid target overheating, water is circulated through a copper fixture in which the tungsten target is seated. Radiative interactions are a source of the bremsstrahlung radiation. In the megavoltage range the X-ray beam produced by the target has a fluence distribution sharply peaked in the direction of the incident electrons. As the energy of the impinging electrons is increased, the fluence distribution becomes increasingly forward peaked. The third possible interaction is electron scattering, which depends on the atomic number of the target and causes increasing angular spread of bremsstrahlung photons. The target can be thick, intermediate, or thin as compared to the practical range of electrons R_p. Electrons striking a thin target with a thickness of about 0.02 R_p, are less scattered and photons are produced by maximum energy "collinear" electrons. In thick targets (with a thickness of about 1.1 R_p), the electron kinetic energy varies from zero to maximum, and the angular distribution of the X-rays created is broader. Despite these drawbacks medical linacs employ thick targets because they do not transmit incident electrons, and therefore also

minimize the production of extra focal X-rays at the flattening filter. The flattening filter is used in conjunction with the target to create a highly uniform dose distribution along the radial dimension of the X-ray beam. The flattening filter is a cone-shaped copper block, which provides the required uniformity of the dose distribution on a 40x40 cm^2 plane at the isocenter of the machine, for each photon energy at a chosen depth in phantom. However flattening filter also substantially reduces the dose rate at the center of the beam. In the Varian 2100 two flattening filters and up to 5 foils are located on a special carrousel which allows for positioning of the required flattening filter or foil under the beam, depending on the selected mode of operation. The X-ray production efficiency for different combinations of target and flattening filter materials was estimated in studies carried out by Podgorsak E.B. et al.[23,24]. The results showed that the most penetrating beams could be obtained from a target with low atomic number *Z* and a low atomic number *Z* flattening filter for electrons above 15 MeV, and high Z target/low Z flattening filter for electron energies below 15 MeV.

Dose monitoring system

The "heart" of the dosimetry system employed in the Clinac 2100 linac is a Kapton dual ionization chamber, consisting of two independently sealed ionization chambers. The purpose of the ionization chamber is to monitor the beam position and dose rate (Fig. 3.14).

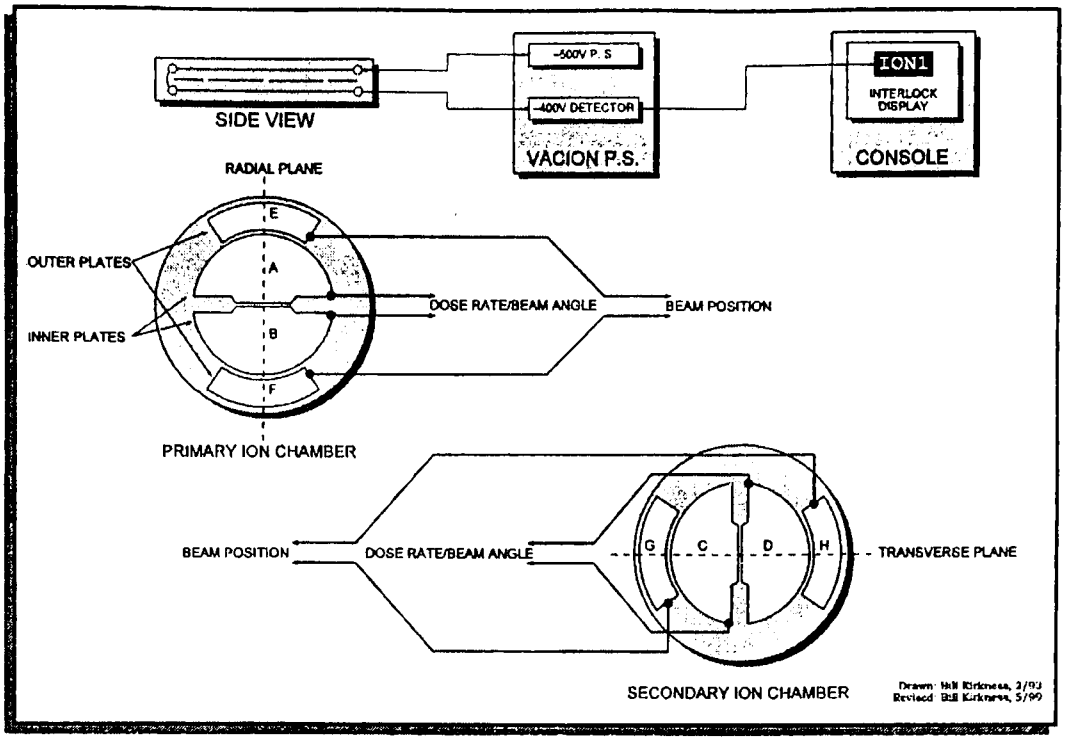

Figure 3.14. Schematic diagram of a dual ion chamber[22].

The ionization chamber operates at –500 V. Each chamber has two pairs of plates. In the primary chamber (close to the flattening filter) the plates are aligned along the radial axis of the beam; in the secondary chamber the plates are aligned along the transverse axis. The summed output from the inner plates on both chambers is proportional to the dose rate. The differential output current is proportional to the beam angle symmetry error. The outer plates are used to provide information about beam position symmetry error through monitoring their differential output.

During the beam-on state, when the total charge collected between the inner plates of the ionization chamber reaches certain preselected level, the electrometer is reset and the dose counter is advanced by one unit called a "Monitor Unit" (MU)[25]. Each MU corresponds to a predetermined dose value and commonly treatments are prescribed in terms of numbers of MU. The counter starts to count monitor units up to the desired

value and the beam control circuitry triggers the beam-off command when this value is reached.

Pulsed modulator

The pulsed power to the microwave generator (either klystron or magnetron) is provided by the pulsed modulator which basically contains a high voltage power supply (three-phase full-wave rectifier), a resonantly charged pulse forming network (PFN) and a high current thyratron for discharging the voltage from the PFN (Fig. 3.15). The current pulse generated by the PFN discharge is routed through the primary windings of the step-up high voltage pulse transformer bringing the negative pulse amplitude of the cathode of the microwave generator to 50 - 120 KV. The modulator works at the pulse repetition frequency of up to hundreds of Hz and pulse duration of up to 10 μs.

The output of the high voltage AC power supply (HVPS) in the modulator is routed via a charge choke and rectifying diodes to the capacitors of the PFN, charging them to abut 25 kV. This voltage may depend on the power mode (low or high energy X-rays) and voltage settings on the selected program board. A special regulating technique, called the DeQing, is used to control the PFN voltage and to dynamically change it on every charge cycle. The PFN voltage is monitored by a 3000:1 high voltage divider and is being constantly compared with the reference voltage from the program board. During the charging cycle, when the PFN voltage reaches a preset value, the signal is sent to the grid of DeQing thyratron, which interrupts the charging current to the PFN.

The current through the HVPS and the main thyratron is monitored by dedicated interlock circuitry in order to prevent damage to the tube and other elements due to shorting in the discharging and charging circuits.

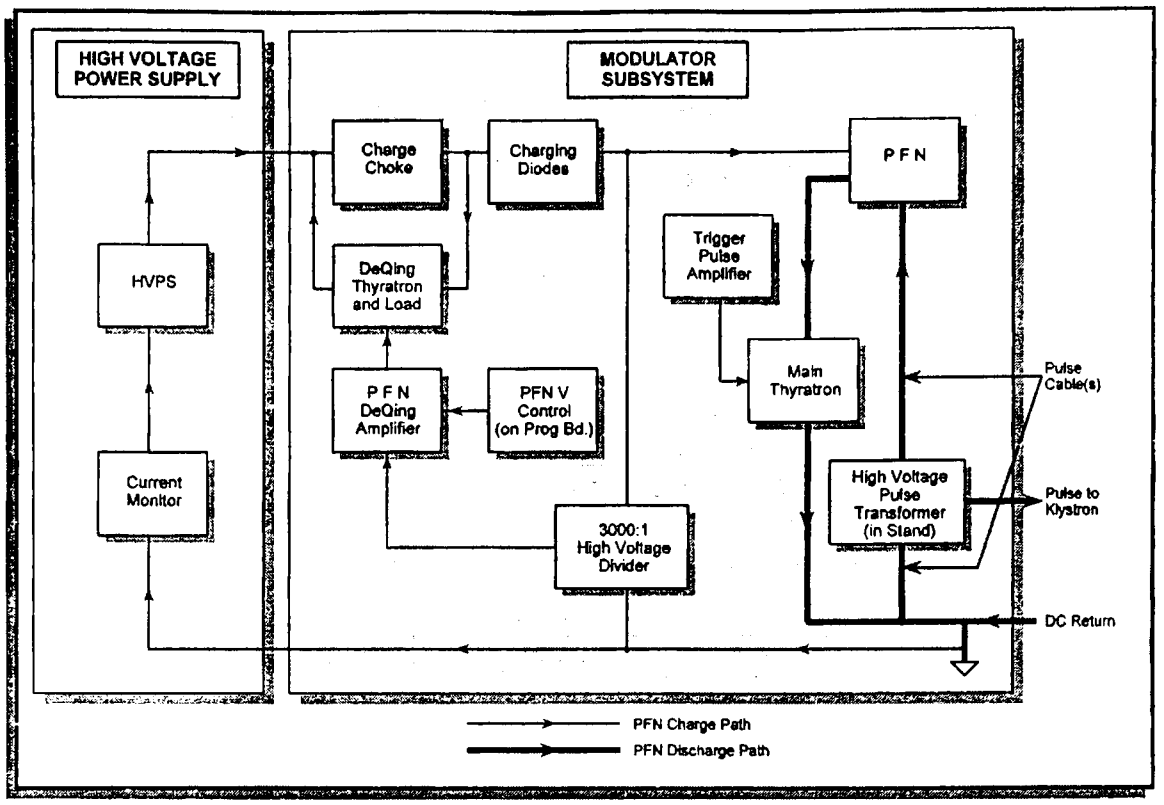

Figure 3.15. Block diagram of the Clinac's pulsed modulator[22].

The PFN voltage is applied to the anode of the main thyratron tube. Once the trigger pulse amplifier sends the 2 KV pulse to the thyratron grid, the thyratron becomes conductive and the PFN discharges through the thyratron and the primary winding of the pulse transformer (turn ratio 1:11) via four 50-Ohm pulse cables thus generating pulses up to 120 kV that feed the microwave generator.

Microwave power source and circulator

The two types of microwave generators commonly used for radiotherapy accelerators are magnetrons and klystrons. The magnetron is a self-exciting source of high power microwaves, while a klystron works as an amplifier of the RF output from the special oscillator called an RF driver. The main practical consideration for using one or the other microwave generator is the peak power that they produce. Magnetrons are

used for electron energies up to 10 MeV, when a peak RF power of up to 3 MW is sufficient. For higher electron energies, a higher peak power (up to 12 MW) is required and a klystron is the microwave generator of choice.

The major components of a magnetron are illustrated in Figure 3.16(a). The water-cooled anode consists of an array of cavities arranged around a cylindrical, oxide coated cathode, indirectly heated by a tungsten spiral. The whole structure is placed between the poles of a permanent magnet with the lines of force parallel to the anode cylinder axis. When the negative voltage pulse is applied to the cathode, the electrons from the cathode accelerate toward the anode and circulate concentrically round the anode–cathode space due to the presence of the magnetic field. The magnetic field in the anode cavities oscillates at a frequency determined mainly by the dimensions of the structure. Electrons may be either accelerated or decelerated in passing the gap of the cavity. The spiraling electrons transfer energy to the oscillating cavities when they are decelerated, and this results in the emission of the microwaves.

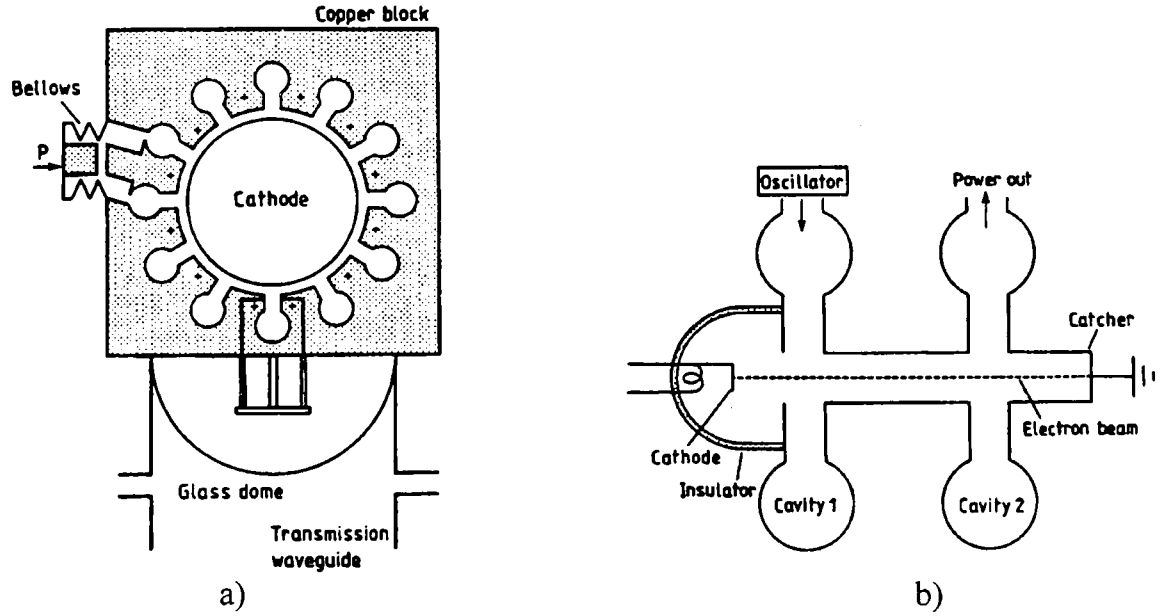

Figure 3.16. Schematic of microwave generator: a) magnetron; b) klystron[20].

The peak power generated by a magnetron depends on electron emission from the cathode and the applied voltage.

In high-energy standing-wave linacs the source of microwave power is usually a klystron (Fig. 3.16 b), which generates power at the resonant frequency of the waveguide. The primary resonant cavity (cavity 1 or "buncher" cavity) is exited by a low-power RF driver. The electron beam, produced when a negative high voltage pulse is applied to a heated cathode, passes along the central axis of the system and is either accelerated or decelerated while passing through the gap of the oscillating cavity 1. A focusing coil is used to maintain the electron beam on the axis. At the gap of the secondary cavity electrons arrive in bunches at a frequency determined by the frequency of the primary cavity. The secondary cavity has the same resonant frequency as the primary, thus electrons are exciting the secondary cavity, effectively passing their kinetic energy to the oscillating field of the cavity as they arrive at the water-cooled catcher at the end of the valve.

During the power pulse from the modulator, the klystron amplifies the RF driver output to produce the power needed for the accelerator waveguide (Fig. 3.17). When the RF power first reaches the standing-wave accelerator structure all of it is initially reflected back toward the source. Once its amplitude has stabilized, if its frequency is equal to the resonant frequency of the accelerator, it begins to flow into and resonate within the accelerator. At the end of the pulse, as the amplitude begins to decrease, the power is again totally reflected. In order to separate the forward and reflected power, a 4 port circulator is employed.

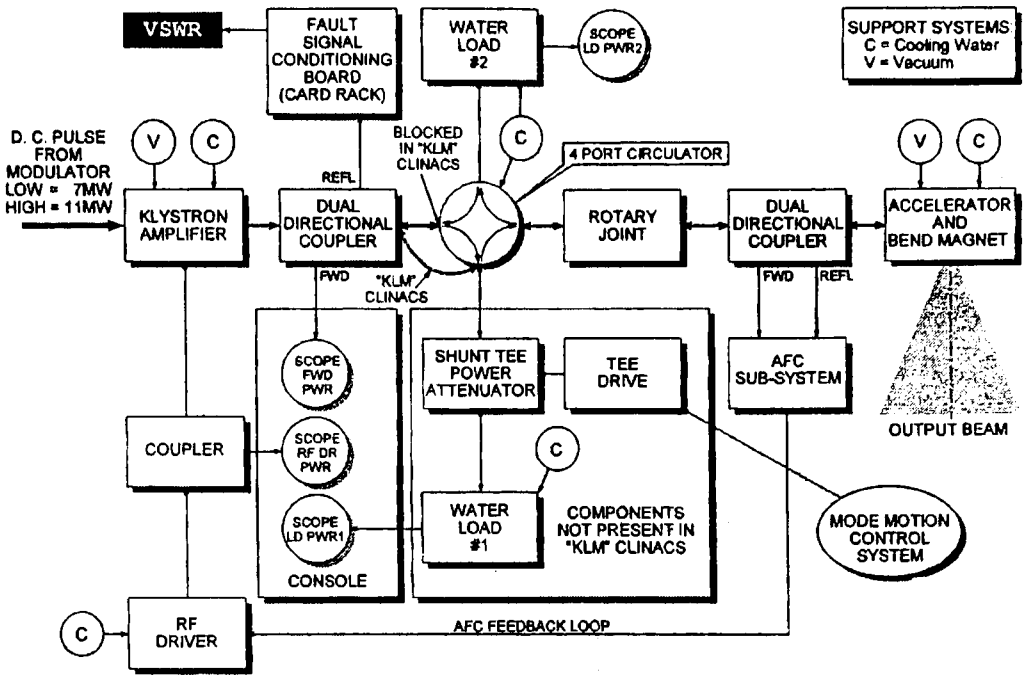

Figure 3.17. High Energy Clinac RF System Block Diagram[22].

To compensate for the changing of the resonant frequency of the waveguide during the beam-on state an automatic frequency control (AFC) subsystem is used. The phase of the forward power signal and reflected power signal at the output of the dual directional coupler are compared. This is the function of the 3-dB Quadrature Hybrid, which then generates two output signals. These signals have equal amplitude when inputs are equal in phase. A special board monitors the differential signal at the output of the 3-dB Quadrature Hybrid and changes the RF Drive frequency accordingly to keep it equal to the resonant frequency of the waveguide.

Collimator

A high energy linac employs two beam-defining independent collimators, also called the upper and the lower jaws. The position of each of the four collimator blocks can be controlled independently, and may be moved symmetrically about the axis of

rotation of the treatment head. To minimize the X-ray beam penumbra the collimator blocks move in an arc with the arc center being on the target.

Multileaf collimator

In order to minimize the irradiation of the normal tissue it is often necessary to apply non-rectangular collimation to achieve irregularly shaped fields. On our linac this function is performed by the multileaf collimator (MLC) Mark 2, which includes 80 specially shaped tungsten leaves (40 leaves on each side), each leaf driven by a motor. To ensure precise leaf positioning, motors have special rotary encoders on their shafts (primary feedback), and each leaf has a secondary feedback circuitry. While moving the leaf to a predefined position, the MLC Controller constantly compares the primary and secondary readings, thus providing reliable leaf positioning accuracy.

Control unit

The linac modes of operation are controlled by a dedicated controller inside the console cabinet, which incorporates an assortment of control and interlock systems. The interlock system is provided to ensure that only valid selections of accelerator settings are used and will interrupt treatment if a discrepancy between the predefined settings and current parameters of the beam occurs. Most interlocks in the linac include both hardware and software paths to maintain the highest possible level of safety.

Support Systems

A high energy linac employs several auxiliary systems which are not directly involved in beam generation but are absolutely necessary for the proper operation of the machine. These include the vacuum system, the cooling system, dielectric gas, and compressed air.

Vacuum system

Ion pumps are typically used when an ultra-clean and ultra-high vacuum is needed. A high-energy linac incorporates three ion pumps: for the accelerator waveguide (5kV power supply, 20L), for the electron gun and for the klystron (3kV power supplies, 8 and 2L respectively). These pumps maintain the pressure in the waveguide and klystron at the level of 10^{-7} Torr. Two titanium cathodes in the form of grids and a cylindrical anode sitting between them represent a basic ion pump cell (Fig. 3.18). The whole system is placed between the poles of a permanent magnet.

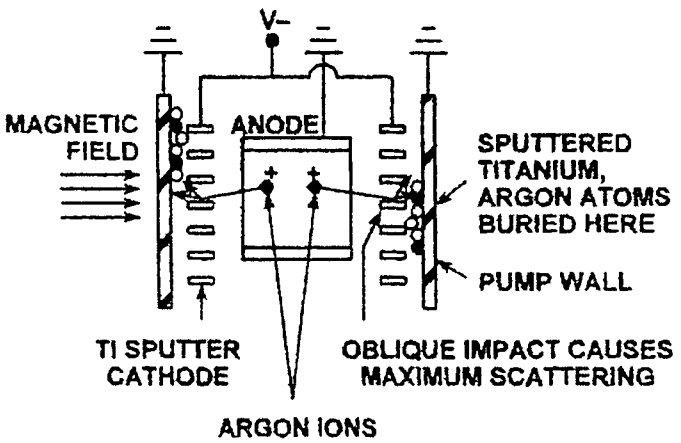

Figure 3.18. Ion Pump Schematic[22].

When the high voltage is being applied to the anode, free electrons begin travel toward the anode of the cell, ionizing gas molecules. Ions generated as a result of ionization accelerate towards the titanium cathode and hit its surface with the energy defined by the discharge voltage. Secondary electrons along with the particles of titanium are being emitted by the cathode thus maintaining cold cathode glow discharge in the cell. Spattered titanium deposits over the internal structure of the ion pump. The needed pumping action is accomplished by the thin titanium layers, which chemically interact with the gas molecules and convert ("bury") them into solids residing on the internal structure of the cell, mainly on the walls of the pump.

The aim of the permanent magnetic field is to lower the working pressure of the pump. This happens as result of the increase in the free path of electrons – the distance the electron travels between two successive collisions. Instead of straight lines in the absence of the magnetic field, they travel in long helical orbits with the increased probability of ionizing gas molecules. The pump current is proportional to the gas conditions inside the pump – a higher current indicates a higher pressure. Thus no special gauge is needed to monitor the vacuum in the system.

Cooling water system

The internal distilled water is pumped throughout the linac by a submersible pump sitting in the water tank in the stand of the machine. A heat exchanger transfers the heat of the internal water to an external water line. The normal temperature of the internal water is maintained at the level of 40^{o} C. In order to remove all the impurities from the internal water, including metallic ions, a Culligan deionizer/filter system has been implemented. Water flow is monitored by four flow switches in each of the cooling water loops of the internal water system.

Dielectric gas

The RF power from the klystron is transmitted to the accelerator waveguide via the S-band rectangular waveguide in a TE_{01} mode. High electric field strength in the waveguide sections require high pressure of SF_6 to avoid high voltage breakdowns. To separate evacuated sections of the accelerator waveguide from the gas filled rectangular waveguide a special ceramic window is used. The SF_6 pressure is maintained at the level of 30 psi. Special measures are taken to prevent the pressure from exceeding 35 psi to limit the load onto the ceramic window.

Compressed air

Several linac units require compressed air to operate. These include target drive mechanism, carrousel pin mechanism, T-drive and the energy switch. The air pressure is about 40 psi.

Portal Imaging System

The Portal Vision (PV) system allows real time acquisition of images for verifying proper positioning of the patient (in lieu of a port film) and establishes a permanent patient image record on the Vision Database (the database tracking). The PV system consists of an image detector unit placed on a special holder, which is a part of a retractable arm (R-arm), allowing for proper positioning of an image detector unit in reference to the patient set up. The image acquisition system on the accelerators in Halifax contains a special planar ionization chamber incorporating an array of electrodes (256x256), which generates a signal proportional to the X-ray distribution across the image detector unit (Fig. 3.19). The PV image acquisition system has a sensitive area of 32.5x32.5 cm^2; its absolute special resolution is 1.27 mm (approximately 1 mm at the isocenter).

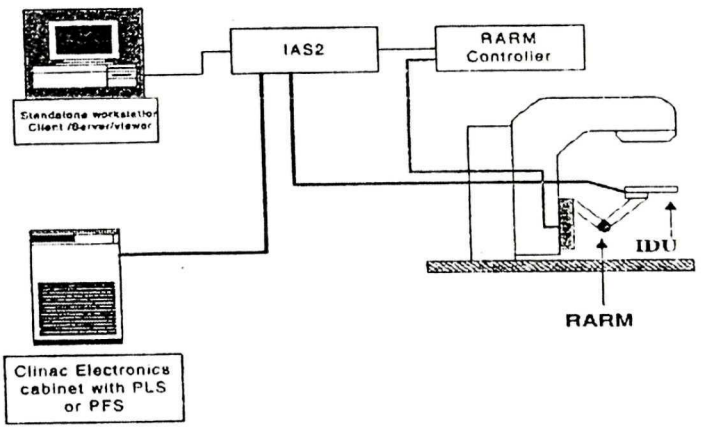

Figure 3.19. Basic Portal Vision System.

Chapter 4.

Breathing-synchronized radiotherapy: literature review

Tumor movement during the respiratory cycle causes various problems in radiotherapeutic process, such as improper sampling during the CT simulation, as well as volumetric and positional errors in the CT planning This results in increased treatment margins to account for the tumor movement during the planning and treatment process. Many researchers have studied tumor movement associated with respiratory motion using different types of organ motion detectors. As well, several techniques have been developed for simulation and treatment dose delivery. In order to reduce the treatment field size and spare healthy tissue, radiation has been administered at a predetermined stage of the breathing cycle. Various tumor motion detectors have been investigated, including direct and indirect tumor motion monitoring devices. The results obtained by different investigators show the usefulness of motion tracking and gated radiotherapy systems. The aim of this chapter is to present a literature survey of the current respiration-synchronized radiotherapy techniques.

4.1 Characteristics of respiratory motion

The purpose of the lung is to act as a contact surface between blood and air. The lung volume changes significantly during the respiratory cycle, and can cause lung tumor motion. During respiration lung tumors can move in all directions: inferior-

superior, anterior-posterior and lateral. The range of movement depends on many factors, such as the patient's constitution, the breathing pattern of the patient and the tumor location. Tumor position in the lung is considered one of the most important factors. The closer a lesion is to the diaphragm, the larger the range of movement. The most significant range of motion (up to 5 cm) can be caused by diaphragm movement and occurs in the inferior-superior direction.

Chen et al.[8] performed imaging studies of a patient with two metastatic tumors (Fig. 4.1)[8]. They showed, that the tumor close to the hilar region on the patient's left side moved during the respiratory cycle with a range of 5 mm, while the up-and-down displacement of the other tumor next to the diaphragm was approximately 3 cm.

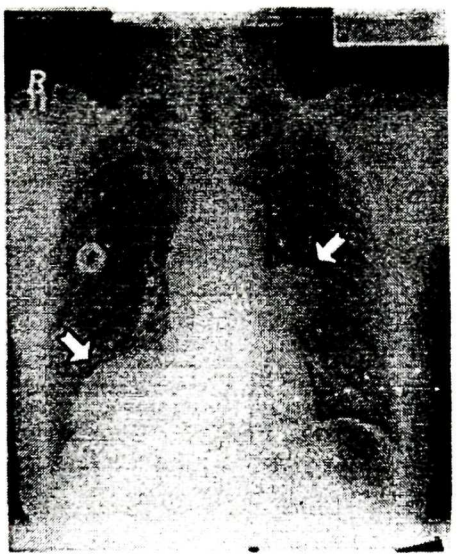

Figure 4.1. Radiograph of a patient with two lung lesions. Tumor sites are marked with arrows[8].

In diagnostic radiology, tumor motion during the respiratory cycle significantly affects the estimation of the volumes of critical structures. Movement in any direction causes blurring and artifacts in CT images. Inferior-superior motion leads to improper sampling of the structure on CT (which will be described later). In radiotherapy, especially in the case of lung cancer treatment with a two-field technique (AP-PA beams

– first phase and lateral boost– second phase), all possible directions of tumor movement should be considered and extra margins added to a clinical target volume to account for tumour motion.

To illustrate how drastically the treated volume changes when extra margins are added to a tumor volume to account for its movement we consider 1 cm margins added to a sphere-shaped tumor with a diameter of 2 cm. In this case extra margins of 1 cm added to account for a movement during respiration cycle cause an increase of the PTV by 8 times.

4.2 Breathing-synchronized radiotherapy systems currently in use

Currently, several types of breathing-synchronized systems, based on different types of organ motion detectors, are in use in radiotherapy.

4.2.1 Spirometer-based systems

Spirometer-based systems are used for monitoring the volume of air in the lung. The patient breathes into a mouthpiece connected to a differential pressure pneumotachograph spirometer and nose clips are used to prevent air leaks. The spirometer signal is connected to the serial port of a computer. The computer display shows a graph that tracks the patient's breathing volume over time. Treatment can be provided at any specific phase of the respiratory cycle[6,7,11] (Fig. 4.2). Figure 4.3 illustrates the possible tumor motion during treatment without and with respiratory gating technology.

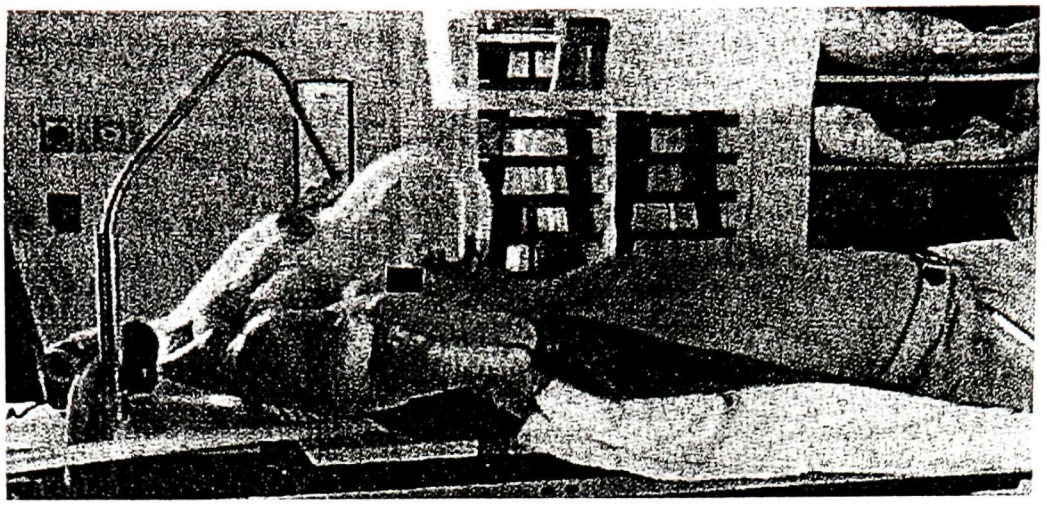

Figure 4.2. Monitoring of respiration with a pneumotachograph spirometer[6].

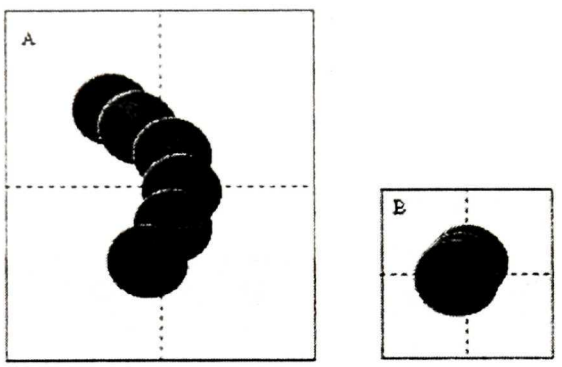

Figure 4.3. Tumor motion during treatment: a) without respiratory gating, b) with gating technology[26].

4.2.2 Video camera-based systems

Video camera-based systems characterize the patient's breathing pattern using a video monitor. A block with retro-reflective markers is placed on the patient. Infrared light aimed at a marker is reflected and monitored by a camera (Fig. 4.4) and the continuous signal is processed by a computer system. A treatment plan can be created by correlating the tumor location with the location of external markers during simulation. The treatment beam is gated "on" only when the tumor falls within the planned beam aperture[9,10,27].

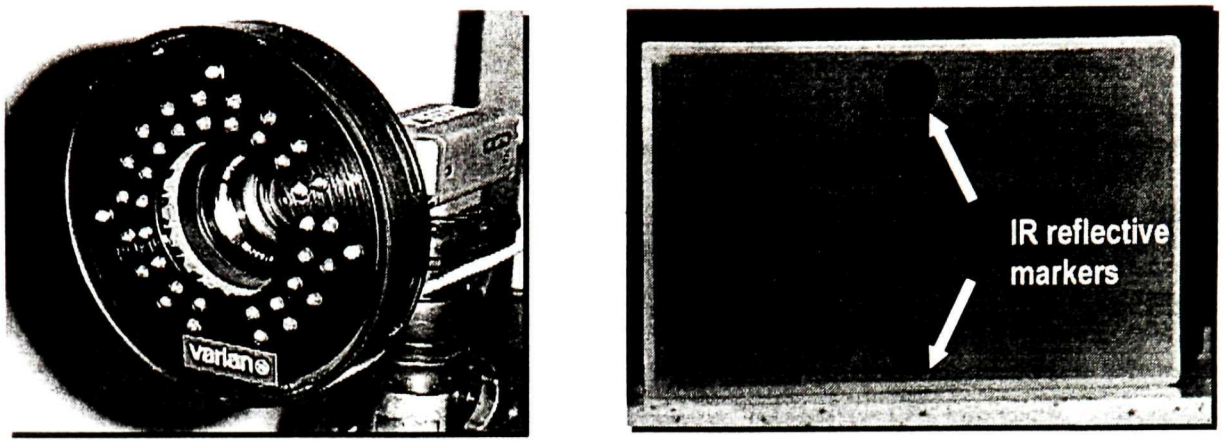

a) **b)**

Figure 4.4. a) Wall or ceiling mounted video camera for standard simulation and treatment; b) the block with infrared retro reflective markers[28].

4.2.3 Systems tracking changes in the body circumference

Several types of sensors are used in systems which track changes in the body circumference such as strain gauge sensor or respiband (inductive plethysmography)[7,27,29].

A strain gauge sensor is a device whose electrical resistance varies in proportion to the amount of strain in the device. Strain is the amount of deformation of a body due to an applied force. The strain gauge consists of metallic foil arranged in a grid pattern, which maximizes the amount of foil subject to strain in the parallel direction and due to minimized cross sectional area reduces the effect of shear strain and Poisson strain. The grid is attached to a thin backing, called the carrier, which is adjusted directly to the test specimen. In breath-synchronized radiotherapy, the strain due to the patient's thorax and abdominal pressure is sensed by the strain gauge, which responds with a linear change in electrical resistance. Then the signal is amplified and analyzed by the computer.

Respiratory Inductive Plethysmography (RIP) measures changes in the cross-sectional area enclosed by a wrap-around inductive sensor (respiband). The sensor is

placed around the patient's abdomen, while signals are traced by the analyzing system. It has a minimal influence on the spontaneous breathing pattern.

4.2.4 Fluoroscopic real-time tumor tracking systems

A fluoroscopic real-time tumor tracking system consists of up to four sets of diagnostic X-ray television systems and a moving object recognition system to capture the image of gold markers implanted in the tumor or near the tumor[30]. During radiotherapy the gold marker fluoroscopic image is displayed on two of the four X-ray television systems adjacent to the treatment console of the accelerator. Coordinates of fluoroscopic real-time images are compared with coordinates of the tumor center and the gold marker, which have been transferred from the 3D treatment planning system to the fluoroscopic real-time tumor tracking system. The system allows the beam to be switched on only if the coordinates of the marker are within the limits of the predetermined permitted dislocation (Fig. 4.5).

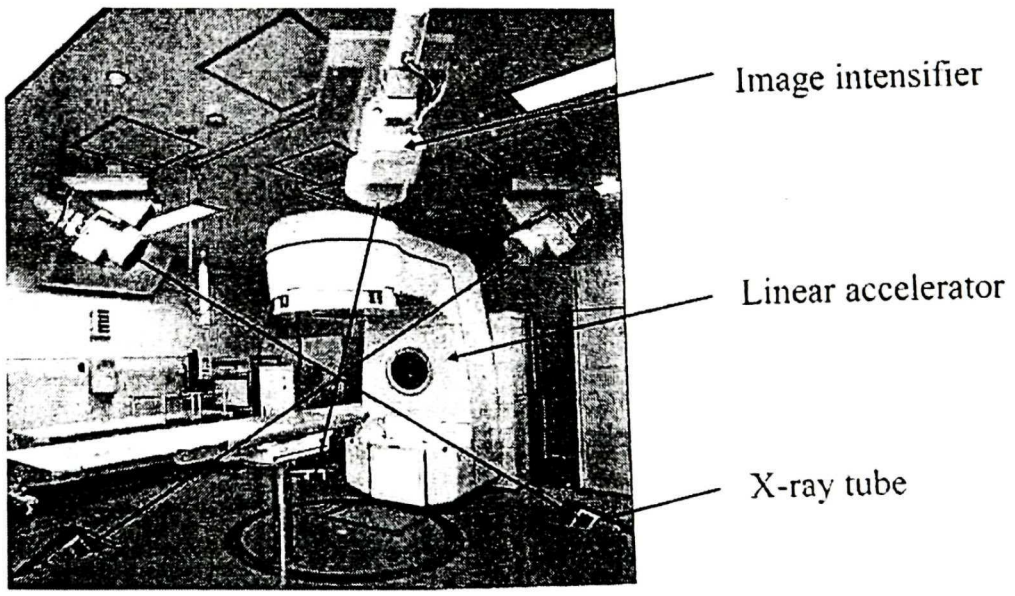

Figure 4.5. The motion-gated linear accelerator system and fluoroscopic real-time tumor tracking system[30].

4.2.5 Thermosensor-based systems

Thermistor and thermocouple temperature sensor systems monitor the temperature change as air flows in and out of a patient's air pathway. Chromega-constantan thermocouples and 0.5 mm glass-bead thermistors were studied by Kubo et al.[31] Sensors were placed into the patient's nostrils. They used two similar sensors in order to a) double the signal size and b) ensure that even if one nostril is partially blocked it is still possible to have a reasonable signal size. All signals were fed into a Keithley-181 nanovoltmeter. Both the thermistor and thermocouple showed similar response curves, but the signal from the thermistor was 23 times higher. The signal from the temperature sensor tracks the air volume in the lung. The amplitude of the signal depends on the room temperature when inhaling and on the lung temperature when exhaling. The temperature sensor signals were characterized by their accuracy, reproducibility and rate of response. This is a cost effective way to study organ motion and patients seemed to tolerate this technique very well.

4.3 Two basic approaches in treatment delivery

The signal from organ motion detector systems can be used to start and stop the external beam radiotherapy treatment at any arbitrary point of the respiration curve. There are two basic approaches to using this capability in treatment delivery: breath-hold and free breathing techniques. In the free breathing technique, gating thresholds are established and each time the signal falls between two gate levels, treatment is enabled (Fig. 4.6). This type of respiratory gating allows the patient to breathe naturally and

remain comfortable. The treatment field will be larger in this case than for the breath-hold technique, to account for tumor movement within the gated window.

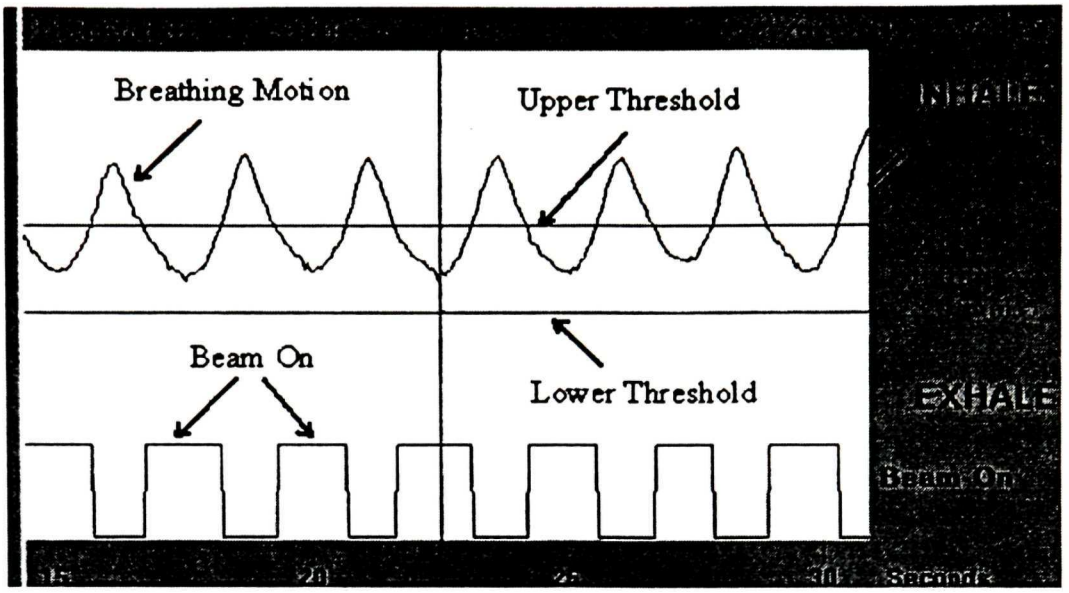

Figure 4.6. Representation of the marker position vs. time. Gating thresholds are indicated by horizontal lines, set here at expiration. The bottom trace indicates the beam-enable signal[32].

The breath-hold technique is usually performed either at the exhalation phase or the inhalation phase of the respiration cycle. It is believed that the exhalation stage is more reproducible, because the diaphragm is more relaxed at this time[7,29,33]. The breath-hold technique demands that the patient acquire some skills during a training session. The Deep Inspiration Breath-Hold (DIBH) technique has the advantage of sparing healthy tissue: due to maximum lung expansion, considerable healthy lung is moved away from the primary beam. Thus, the dose to the tumor can be escalated safely for the same risk of normal tissue complications. Figure 4.7 represents a spirometry signal with DIBH[6]. Treatment is delivered during breath-hold (flat part of the signal).

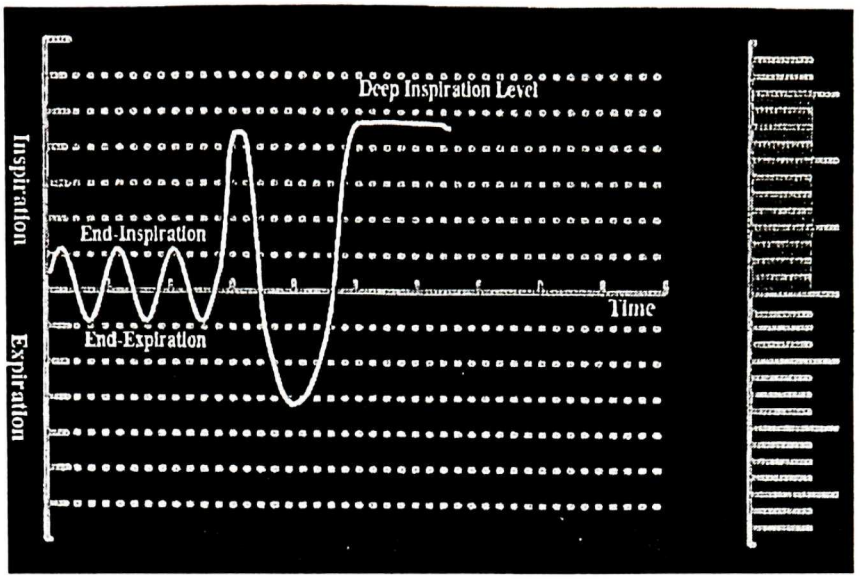

Figure 4.7. Representation of spirometry tracings with DIBH technique[6].

As shown in the research work of Hanley and colleagues[34], gated treatment (prescribed dose – 75 Gy) in combination with the DIBH technique reduced the mass of healthy lungs receiving a dose greater than 25 Gy by one-third, whereas gated therapy with the free-breathing technique reduced the mass by one-fifth. In the case of the breath-hold technique, the patient can control the breath voluntarily or it can be controlled with an Active Breathing Coordinator (ABC) device (Fig. 4.8). The ABC device is a modified ventilator, which is used for respiratory care. This device immobilizes breathing motion by restricting airflow to and from the patient. During the procedure nasal clips are attached to prevent nasal breathing. The patient breathes through a mouthpiece. At the pre-set lung volumes, both the inhalation and exhalation paths of the patient's airflow are temporarily closed under computer control. Due to pausing of the patient's breath at a precisely indicated tidal volume, clinicians have shown a median reduction of 12% lung mass irradiation for treatment of Hodgkin's disease[35]. It is recognized that efficacy of respiratory gating can be enhanced using the

ABC device, however, it has been reported to be an uncomfortable technique for the patient.

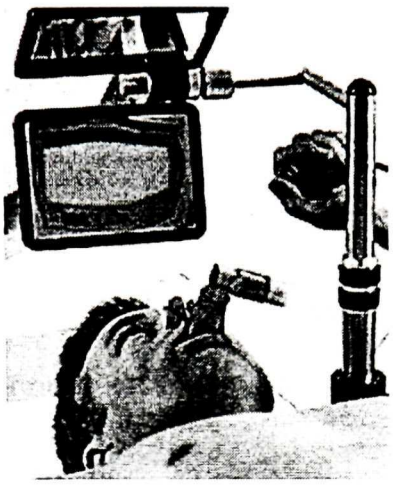

Figure 4.8. Active Breathing Coordinator[36].

4.4 Image studies and advantage of gating technology

For almost every cancer patient the first step of the treatment involves imaging studies of the tumor and critical organs. This is a very important stage during which the treatment volume and critical organs are defined. The more accurately the treatment field is defined during the simulation, the better are the results expected from the treatment.

In the thorax region, where a tumor is subjected to a significant displacement because of respiratory motion, special attention should be paid to accurate localization of the tumor during the breathing cycle. Precise tumor localization is accomplished in a variety of ways.

4.4.1 Conventional simulation

To quantify the relationship between the respiratory volume and diaphragm movement, anterior-posterior (AP) and lateral films can be taken of a patient in the supine position. This allows the estimation of the position of the diaphragm and other thoracic organs under different respiration conditions: free breathing, deep inspiration, shallow inspiration and shallow expiration[6].

Fluoroscopy studies have been found to be extremely useful for studying the direction and magnitude of organ motion[8,11,29,34]. The fluoroscopy images can be recorded, digitized and compared to the breathing signal from an organ motion detector that is simultaneously recorded. This analysis allows an off-line estimation of organ motion and provides the information for the optimal gate window for minimum organ motion during subsequent CT scanning and treatment.

4.4.2 CT studies

Compared to conventional simulation, CT simulation helps visualize tumor tissue directly in 3D space and allows treatment volumes to be determined more appropriately.

One of the major problems with CT images is related to periodic respiratory motion of anatomical structures. Motion artifacts are produced in a CT image if an object is not static but is assumed so in the reconstruction process. Motion artifacts include the doubling of small vessels, black voids and thick white streaks around the high-attenuation structures. Respiratory motion causes improper sampling of the structure on CT images leading to their misinterpretation[37,38] (Fig. 4.9). Volumetric and position errors in CT planning may cause inadequate dose delivery (Fig. 4.10).

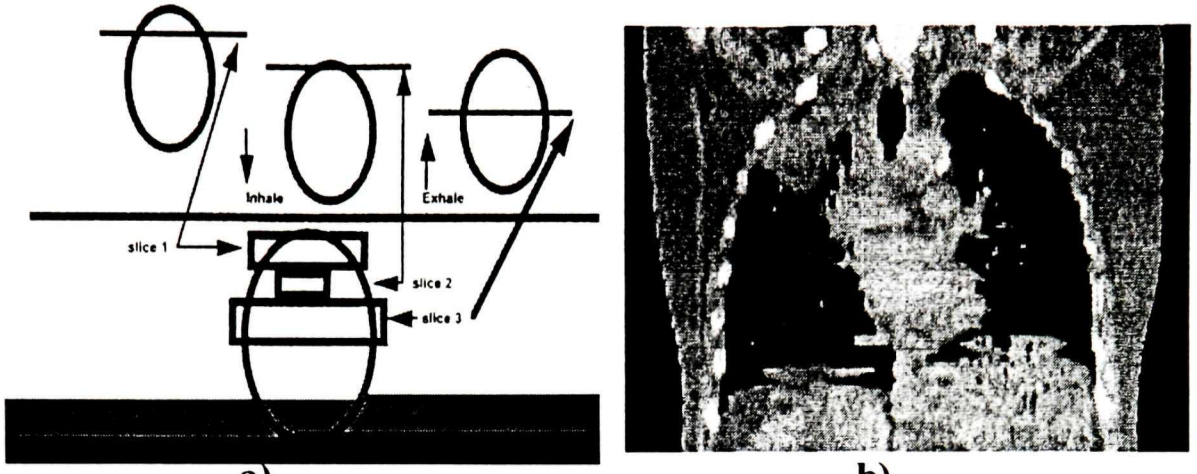

Figure 4.9. a) The inferior-superior motion during respiration cycle causes improper sampling of the structure on the CT[37], b) DRR shows the diaphragm extending into lung tissue due to improper sampling.

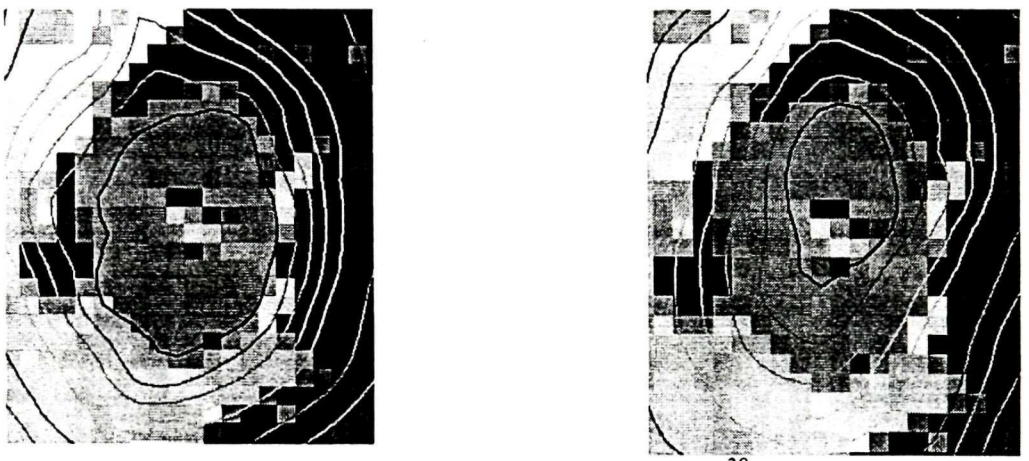

Figure 4.10. Motion related errors in CT planning[38]
a) Planning dose for the static object. b) Actual dose for the moving object.

The process that accounts for the breathing motion and minimizes organ movement artifacts is called respiration-synchronized CT data acquisition[6,11,26,29,30,34,37,38,39]. The breathing signal is tracked by an external motion sensor. The patient breathes under free breathing conditions but image data are acquired only within the predetermined gated window. The same gated window is used subsequently for treatment. In the case of breath-hold gating, CT images can be acquired under different respiration conditions: inspiration, deep inspiration, exhalation, etc. The

resulting three-dimensional imaging volume and free breathing or breath-hold respiration patterns are used to design a gated three-dimensional conformal radiation therapy (3D-CRT) treatment plan. Conformal radiotherapy creates a dose distribution conforming tightly to the shape of the tumor volume in three dimensions, while minimizing the dose to the normal tissue.

4.5 Dosimetric studies

In gated radiation therapy a sequence of small units of dose is delivered in contrast to conventional external beam radiotherapy where the daily prescribed dose is delivered with a single beam-on/beam-off sequence. Several studies have been performed in order to estimate the effects of small monitor unit segments on beam dosimetry[31,40,41,42,43]. The purpose of the study by Ramsey and colleagues[40] was to evaluate systematically the effect of various gating sequences on X-ray central output, ionization ratios (nominal accelerating potential), beam flatness and beam symmetry. Measurements were carried out on a Varian 2100 C/D linear accelerator for 6 MV and 18 MV photons. The gating cycles consisted of 5 gating windows of either 20, 10, 5 or 2 MUs, for an integrated total of 100, 50, 25 or 10 MUs, respectively. The gating lengths used were 0.0, 0.6, 0.9, 1.5, 1.8, 2.5, 3.0, 3.6 and 4.2 seconds. The test with a gating length of 0.0 seconds represents non-gated treatment, which was used for comparison. The results show that the photon beam dosimetry is not significantly affected by gating interruptions. The beam output, flatness and symmetry were within 0.8% for most sequences. The maximum deviations occurred at low-MU sequences (<5 MU). Several other investigators obtained similar results[31,41,42,43]. They report that dosimetric changes

in linac beam characteristic are within specifications and are not clinically significant. The studies show better results for higher MU-gated windows, which suggests that for gated treatment with the breath-hold maneuver (when the dose delivered during a single segment is considerably higher and gating length is larger), the dosimetric effects will be less significant.

Chapter 5.

Our approach: Gated Breath-Hold technique

In our work we have developed a new technique for treatment of lung cancer patients who exhibit a significant range of tumor movement during the respiration cycle. This approach combines the principle of an automatically gated treatment with a Deep Inspiration Breath-Hold (DIBH) maneuver. We use a Linear Position Transducer (LPT) to monitor the changes in the patient's abdominal cross-sectional area. Tumor movement was investigated using fluoroscopy and a CT-simulator. We studied the possible dosimetric effects of small-dose delivery and demonstrated their clinical insignificance. A CT simulator experiment with a dynamic phantom has illustrated the influence of structure movement on the CT planning results. Patient training, simulation and treatment techniques have been developed and the first patient has been treated. The overall Deep Inspiration Gated clinical process is presented on the flow chart below (Fig. 5.1).

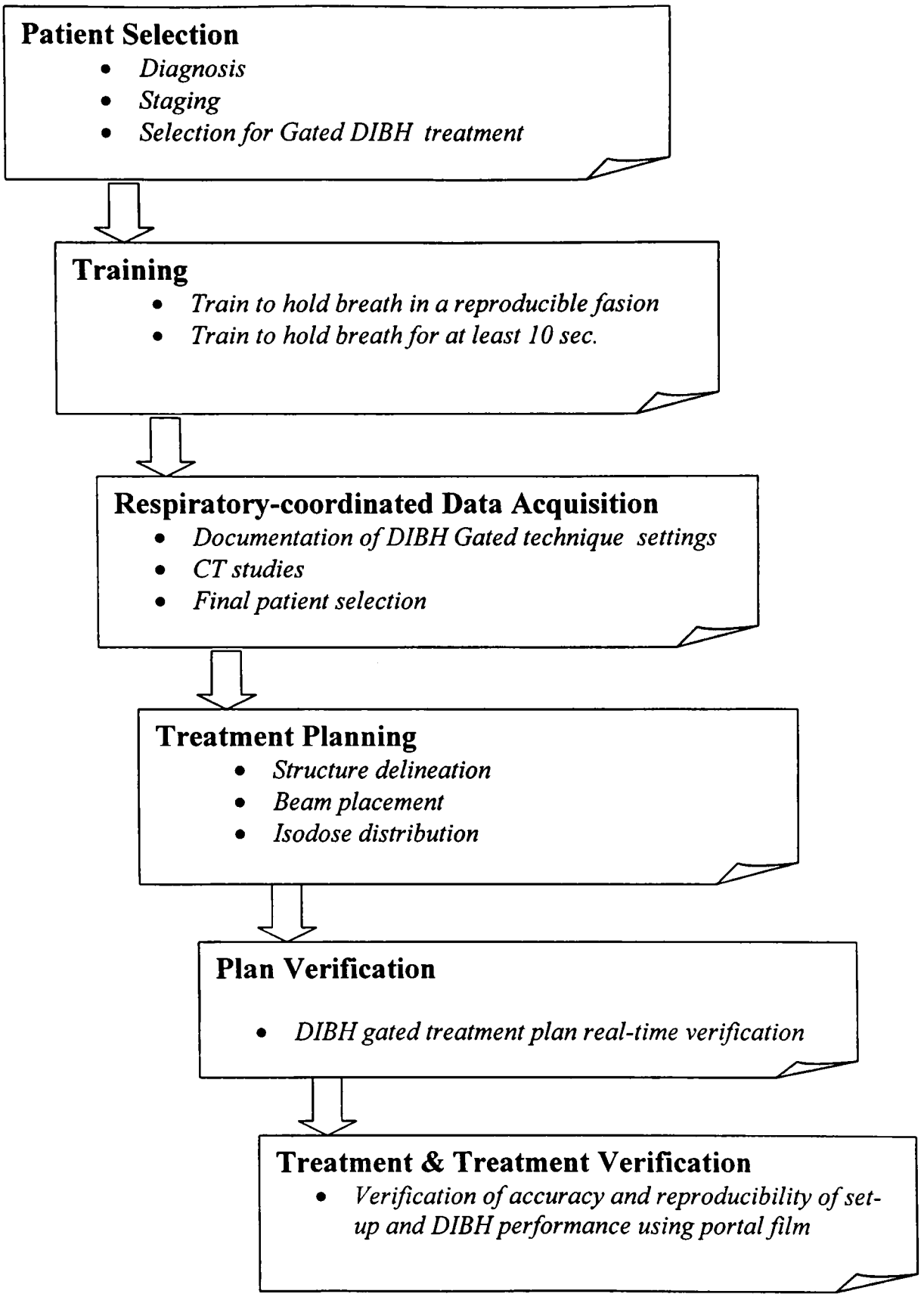

Figure 5.1. Block diagram of Deep Inspiration Breath Hold (DIBH) Gated clinical process.

5.1 Technique: Linear Position Transducer-based monitoring

In our approach we combine two methods: automatically gated treatment and the Deep Inspiration Breath-Hold technique. Treatment is started following a deep inspiration breath-hold maneuver when the lungs reach their full capacity level. The beam is automatically turned off once the patient resumes breathing. The whole treatment can be accomplished with 1-3 breath holds.

For a tumor motion detector we use a Linear Position Transducer LX-PA-2 (UniMeasure Inc., USA), which is a spring-loaded potentiometer with a light rope wound around the axis of the potentiometer (Fig. 5.2). The Linear Position Transducer (LPT) is fixed to one railing of the treatment bed next to the patient's abdomen. A light strap, fixed at one end to the other bed rail, runs over the patient's upper abdominal region and is connected to the rope from the LPT. The Linear Position Transducer is used to generate a voltage signal from the changing circumference in the upper abdominal region as the patient breathes. This device detects a linear range of motion in the strap of 50 mm at a nominal output of 18.5 mV/mm and a nominal wire rope tension of 4.4 N. Weight loss does not affect the gating signal from the LPT because the LPT voltage window is adjusted for a deep inspiration maneuver and accounts only for the difference between the deep inspiration and normal breathing level.

The LPT analog signals are sent to a Micro-P display, which acts as the processing interface between the analog linear position transducer and the user. It applies a current to the resistor in the Linear Position Transducer and displays the measured voltage on the LED display. The Micro-P provides a 10 V DC output to power

the transducer, eliminating the need for an external power supply. Every mili-second, it reads the value from the linear position transducer and automatically displays the reading value on the LED display. An RS-232 serial port allows the Micro-P to communicate with a computer, enabling the computer to graph the chest movement in real time at the treatment console so that the therapist can observe the patient's level of deep inspiration from outside of the treatment room. When a predetermined threshold is achieved, an interface box sends a logic signal to an interface board in either the CT-simulator or the Varian 2100C/D linear accelerator. At the same time, when the threshold is reached, a signal from the relay output of the Micro-P display goes to a pair of feedback glasses worn by the patient. LEDs on these glasses turn on when the beam is on. In our technique we use feedback glasses in order to help patients to monitor breath-hold properly and improve the reproducibility of this maneuver.

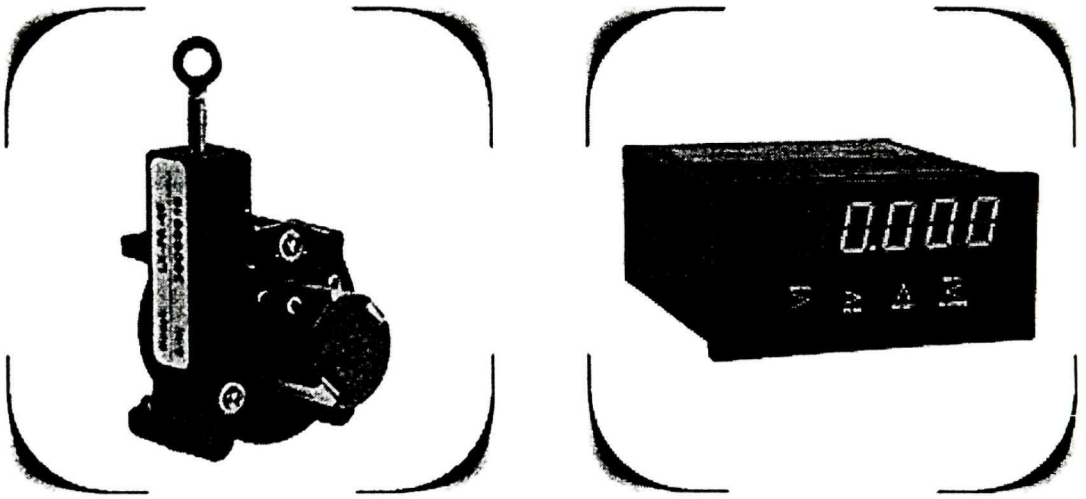

a) **b)**

Figure 5.2 a) Linear Position Transducer UniMeasure LX-PA-2; b) Micro-P display[44].

5.2 Patient training/preparation

Patients selected for DIBH treatment should have adequate pulmonary function, ability to follow the procedure and to perform DIBH. Patients with significant cough, pain, anxiety or with abdominal or shallow breathing patterns are not suitable for this technique.

The Deep Inspiration Breath-Hold maneuver should be performed at full lung capacity and demands certain skills from patients. Patients are scheduled for the training session prior to the simulation. During the training session they are coached by a radiotherapist to reproduce the same deep inspiration level during the simulation and subsequent treatment.

To practice this maneuver a patient needs to lay on his/her back with both arms up above his/her head, with hands holding opposite wrists. A pillow is placed under the knees (Fig. 5.3a). A MED-TEK Vac-Lok immobilization system is used for an accurate and reproducible positioning of the patient throughout the simulation and treatment. A strap from the motion detector LPT is adjusted on the upper abdominal region of the patient. It is thin and narrow with minimum markings of 1 mm enabling the therapist to position the patient reproducibly. The LPT connected to Micro-P device monitors the respiration level. The radiotherapist can estimate the level of the patient's respiration and the reproducibility of the DIBH maneuver from the graph on the display of the computer (Fig. 5.3b). The graph represents the respiratory signal vs. time.

The patient maintains the same level of deep inspiration with the help of feedback glasses. The feedback glasses are ultraviolet-blocking sunglasses with 2 frosted

red LEDs mounted inside. The LEDs are connected to the relay output of the Micro-P display such that when the trip point is reached the lights turn on.

To set up the apparatus the patient first takes a deep breath in and holds it. The tension on the strap is adjusted until the Micro-P reaches the trip value (red light turns on) and the value on the strap is recorded. Adequate performance of the system and strap tension adjustment is checked by asking the patient to take a few regular breaths and by observing the breathing motion signal on the computer monitor. If the tension on the strap is not adjusted properly, the system will not track the respiration motion correctly and it is necessary to repeat the adjusting procedure.

Once everything is set up, a patient takes a few regular breaths in and out. This is followed by a slow deep inspiration, and then a slow deep expiration. The patient then takes a deep breath to the maximal inspiration level (diode lights in glasses turn red) and holds for at least 10 seconds[34]. The patient should not allow any air to escape through the nose or mouth and should repeat this maneuver a few times in order to insure that a deep inspiration level is reproducible.

Patients are asked to practice DIBH at home in order to increase the time of a breath hold and to improve the reproducibility level. We found that it is best to practice twice per day for at least 10 deep breath holds. Because stomach content can influence reproducibility of the organ positions, the patients are requested not to eat during the 2 hours before simulation or treatment sessions.

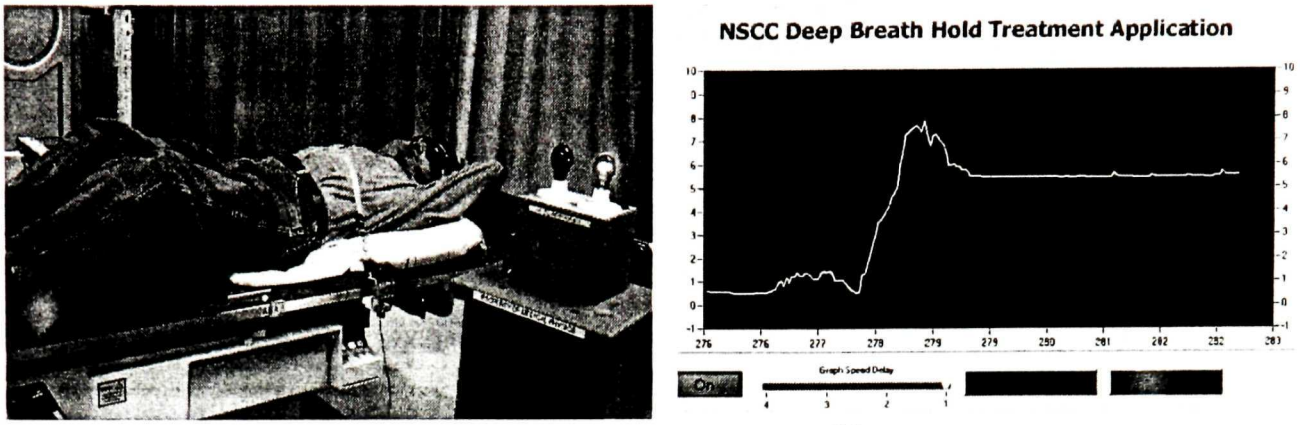

a) b)

Figure 5.3. a) Patient setup; b) Deep Inspiration Breath-Hold signal.

5.3 CT simulation

One of the major steps in the process of treatment planning is target volume localization with the help of a CT scanner. In our technique we use a CT study with multiple acquisitions. The studies were performed on a Picker PQ2000S AcQSim CT-simulator.

The Philips Medical Systems Q series CT imaging system is capable of operating in conjunction with a contrast injector, which allows triggering the CT scanner acquisitions by a signal from a patient during the Deep Inspiration Breath-Hold maneuver.

To perform a single helical scan triggered by a signal present at the injector interface, a new study is opened on the scanner and all the pertinent patient information is entered. The system operators select the injector trigger option via the Operator Communications interface* at the CT console and then begin the scan.

---

* Operator Communications interface (Opcom) is the software that runs on the main computer of the CT scanner. This software allows communication between the user and the computer through peripherals (the touch panel display, VGA monitor, and control keyboard).

When the new study is requested from the Opcom, the scan parameters, such as the requested kV, mA, slice thickness, filter and compensator, are sent to the X-ray controller (the XSC+) in preparation for the scan. When all conditions are satisfied, the console's "Start" button will light green. Depressing the "Start" button will not actually start the scan but will set the injector latch (INJSTRT) within the scanner. The CT scanner will then wait for the trigger from the injector line (INJIACT).

The patient's breathing cycle is monitored by the Linear Position Transducer (LPT), which is adjusted to an upper abdominal region. The LPT tracks the changing body circumference and produces an analog signal, which is fed into the Micro-P device. The Micro-P interface box converts the analog signal into a digital signal and when the signal from the LPT reaches a predetermined level, an interface box sends a logic signal to the injector port J700 of the Picker PQ2000S AcQSim CT simulator and acquisition is started. The flowchart of the CT Simulation process is presented in Figure. 5.4.

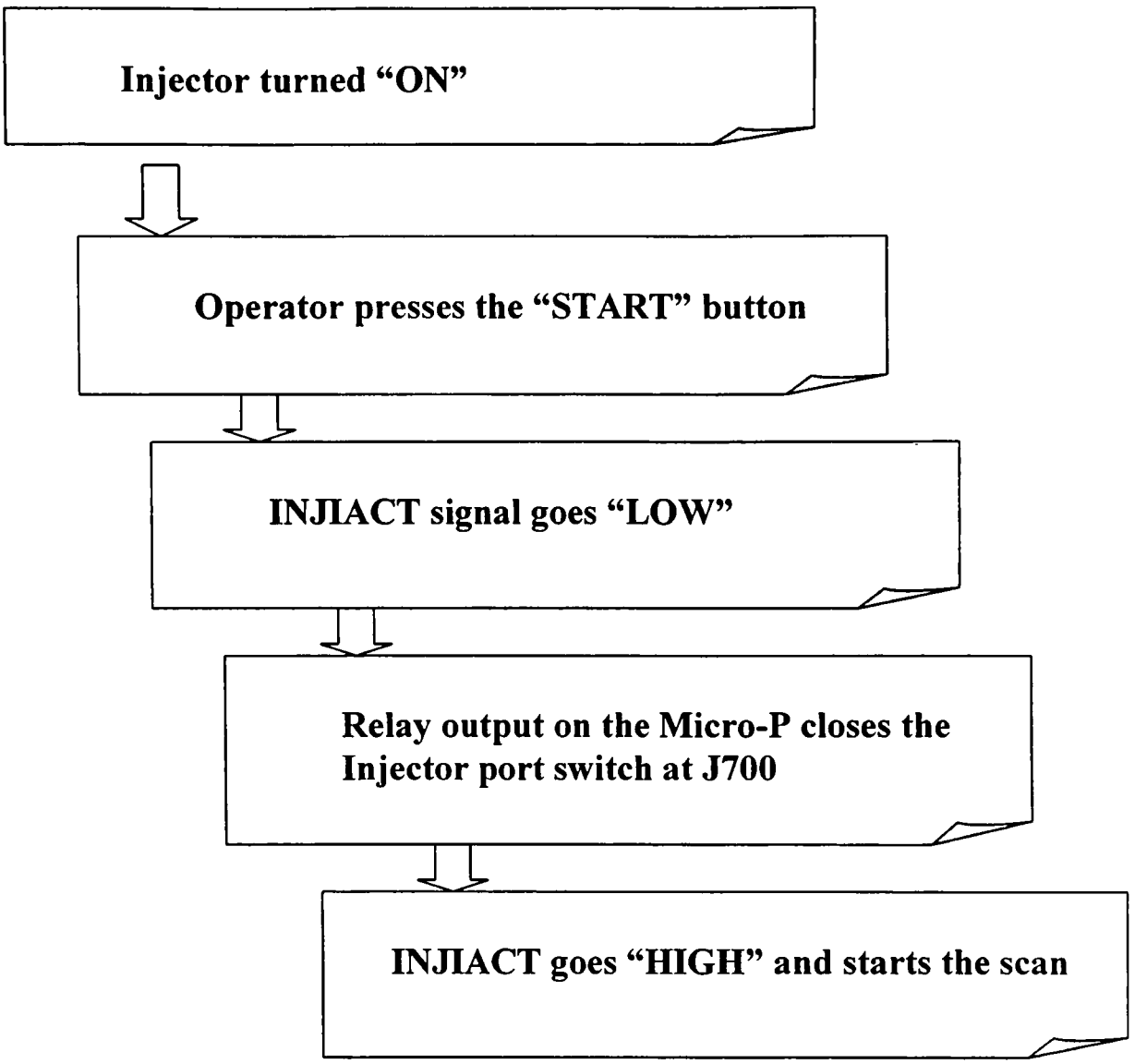

Figure 5.4. The Flow-chart of the CT simulation process.

At the end of the study a signal (INJSTOP) is issued and acquisition is terminated. Helical CT scan acquisitions are performed with a slice thickness of 0.3 cm in the tumor region and 0.5 cm in the rest of the scanning region. The number of acquisitions is determined by the time interval during which patients can maintain a breath hold. During training sessions the average time of breath hold is estimated, and is used for planning the time of acquisitions in CT studies. For an average breath-hold time of 10 s, about eight acquisitions per study are done (~ 10 slices per acquisition). After the first study is accomplished, the patient takes a few regular breaths and then repeats the DIBH maneuver. Once the signal from the LPT reaches the threshold level, the second scanning study starts. The procedure is repeated until the entire planned thorax region is scanned.

For the CT studies the standard patient set up procedure should be performed as described in Section 5.2 and shown in Figure 5.5.

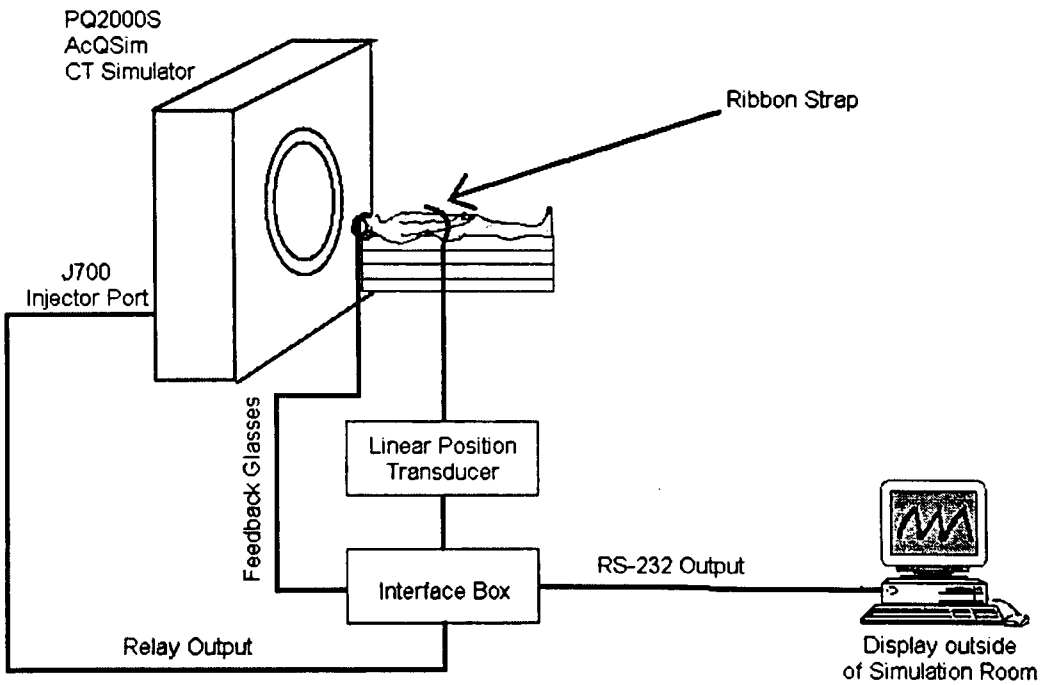

Figure 5.5. Schematic diagram of the CT simulation setup of the Deep Inspiration Breath-Hold using a Linear Position Transducer.

During the simulation procedure the patient wears feedback glasses with built-in LEDs. Feedback glasses are intended to help the patient to self-monitor the breath-hold maneuver. The logic signal of the interface box relay turns on the LED lights once the predetermined threshold for deep inspiration is reached.

The therapist can observe the breathing signal on the computer monitor outside the simulation room. The computer receives the digital signal from the Micro-P box via an RS-232 serial port and displays it in a graphical form as breathing signal vs. time.

The DIBH gated scan demands increased time for the procedure itself and for the setup. As a result of breath-hold during image acquisition, it is anticipated that major problems in acquiring CT images related to periodical respiration motion of anatomical structures can be minimized and volumetric and position errors in CT planning can be avoided.

Subsequently to CT scanning, the target volume/structure delineation and three-dimensional treatment planning is performed, as described in Section 3.1.2. For the first several patients being treated with our DIBH technique, CT scans were performed using both the gated technique and a regular free-breathing procedure. As a result of performing the DIBH maneuver during the image acquisition, we expect a decrease in PTV margins for a targeted volume and improvement in the localization of organs at risk. Results obtained for different methods were calculated, Dose Volume Histograms generated and treatment plans compared.

5.4 Plan verification

The next important step in respiration-correlated imaging is plan verification. This procedure is a real-time verification of the DIBH-gated treatment plan using conventional simulator fluoroscopy.

For our DIBH-gated technique plan verification we use a Phillips SLS 6507 Simulator. This machine has the same geometry as the treatment unit used in our study. For the verification procedure the patient is positioned in exactly the same manner as for the treatment setup (Section 5.2) and CT simulation. During plan verification the patient is imaged in anterior-posterior and lateral directions. The LPT device is adjusted to the upper abdominal region for monitoring the patient's breath cycle. Feedback glasses help the patient to maintain a reproducible breath hold. The patient is asked via intercom to take a few regular breaths in and out, followed by a slow deep inspiration, a slow deep expiration and then take a deep breath until the Micro-P trip point is reached (the red light on Micro-P and feedback glasses indicator both turn red). At this moment the fluoroscopy study should be started. Fluoroscopic studies during the patient's normal breathing can be done to see how tight the PTV is. During fluoroscopic studies with the same geometry as on the treatment machine, beam placement with respect to patient's anatomy can be visualized and adjusted. The physician will check whether or not the planning target volume adequately covers the tumor and accounts for variations in tissue position, size and shape as well as for variations in patient position and beam position. In the case of the DIBH technique intrafraction tumor movement during the breath-hold should be considered. Despite the fact that the breath-hold almost immobilizes the

tumor, the residual motion with a range less than 10% of normal breathing cycle movement can be present.

To digitize and record the fluoroscopic imaging a frame grabber (Matrox Meteor II/Multi-Channel) is attached to the simulator monitor. It allows image capture from interlaced and progressive scan component RGB and single or dual channel monochrome analog video sources with sampling rates up to 30 MHz and with a sampling grid of 640x480 at 8 bits per pixel.

During the real-time plan verification the radiation oncologist verifies the acceptability of the treatment plan by ensuring adequate coverage of the target volume and appropriate shielding of organs at risk. All necessary beam and shielding adjustments are performed during the plan verification procedure. After this verification procedure the patient is ready for the external beam radiation therapy.

5.5 Treatment

The treatment is the final step in the clinical process. By this time the treatment volume region is defined, the treatment plan is prepared and verified, and the patient is well trained for performing the DIBH technique.

In our Varian linear accelerator a gridded gun is used to gate the X-ray beam by stopping the electron flow to the waveguide[40]. The electron flow is stopped by using a fine wire grid over the output end of the electron gun. The grid can be charged and discharged rapidly. Normally the grid is held at a negative potential with respect to the cathode (with a static negative potential -20 kV)[21]. Voltage pulses of between –150 V and +180 V (with respect to the cathode potential) are applied to the grid to control the electron flow to the accelerating waveguide. These pulses are synchronized with pulses

applied to the microwave power source. When these two types of pulses are generated coincidently, electrons from the gun are injected into the waveguide while the RF power is present and a beam pulse is produced. When voltage pulses applied to the grid are delayed compared to the microwave power source pulses, electrons are injected into the waveguide after the RF power and no beam occurs. Gating the beam using gun delay does not power-down any component of the linear accelerator. During the beam hold-off period the electron flow to the waveguide is simply interrupted.

In our clinic the DIBH gated radiation treatment is performed on a Varian Clinac 2100 C/D. In order to reduce the required breath-hold time for patients the dose rate is chosen as 600 MU/min. Patients are positioned as described in Section 5.2. The LPT strap is adjusted around the upper abdominal region (Fig. 5.6) and the patient is instructed via an intercom to take a few regular breaths and then take a deep breath in and hold it.

When a predetermined level of a deep inspiration is reached and the LPT voltage crosses the threshold value, a Micro-P interface box sends a signal to the Clinac console (MHOLDOFF). The MHOLDOFF signal on the Input Interface #1 board in the Clinac console is normally high (+12 V DC) and will enable the beam on and will not delay the gun trigger pulse. When we plug in the gating "shorting" type connector, the MHOLDOFF signal is then driven low (0 volts) which causes the gun pulse to be delayed so that it is no longer coincident with the RF pulse. When the relay output is activated in the Micro-P during the Deep Inspiration Breath-Hold maneuver, the MHOLDOFF signal is then driven high and the beam is turned on. When the patient terminates the DIBH maneuver, the relay is deactivated and the MHOLDOFF signal stays low until the next time it is high again.

Red LEDs in the feedback glasses lights turn on when the Micro-P reaches the trip value. The patient breathing signals from the LPT are fed to a computer via the Micro-P and graphical representation of the breathing signal vs. time is displayed on the monitor.

Patients are trained to perform breath-holds for at least 10 seconds. This means that the entire treatment can be delivered within 1-3 breath holds. Once the beam is gated, the patient is instructed to breathe regularly. The beam can be held off for a maximum of 15 seconds. If the beam is held off for more than 15 seconds, a DPSN (Dose Position) interlock will occur. It was shown with staff volunteers and patients that 15 s is a sufficient time for taking a few regular breaths and preparing for the next DIBH maneuver. When the patient is ready for the next breath-hold, he/she takes a deep breath in, holds it and the whole process is repeated.

The DIBH gated treatment using an LPT as a movement sensor is a highly automated process. The therapist observes the breathing signal on the monitor outside of the treatment room and communicates with the patient via intercom when the time comes to start the DIBH maneuver. Treatment delivery is started and terminated automatically depending on the breathing signal from LPT sensor. This reduces human error influence and improves the accuracy of the method.

Before each treatment a portal image is taken under breath-hold for each field in order to verify the reproducibility of the DIBH maneuver. Portal images are taken daily during the first week of treatment and then weekly thereafter.

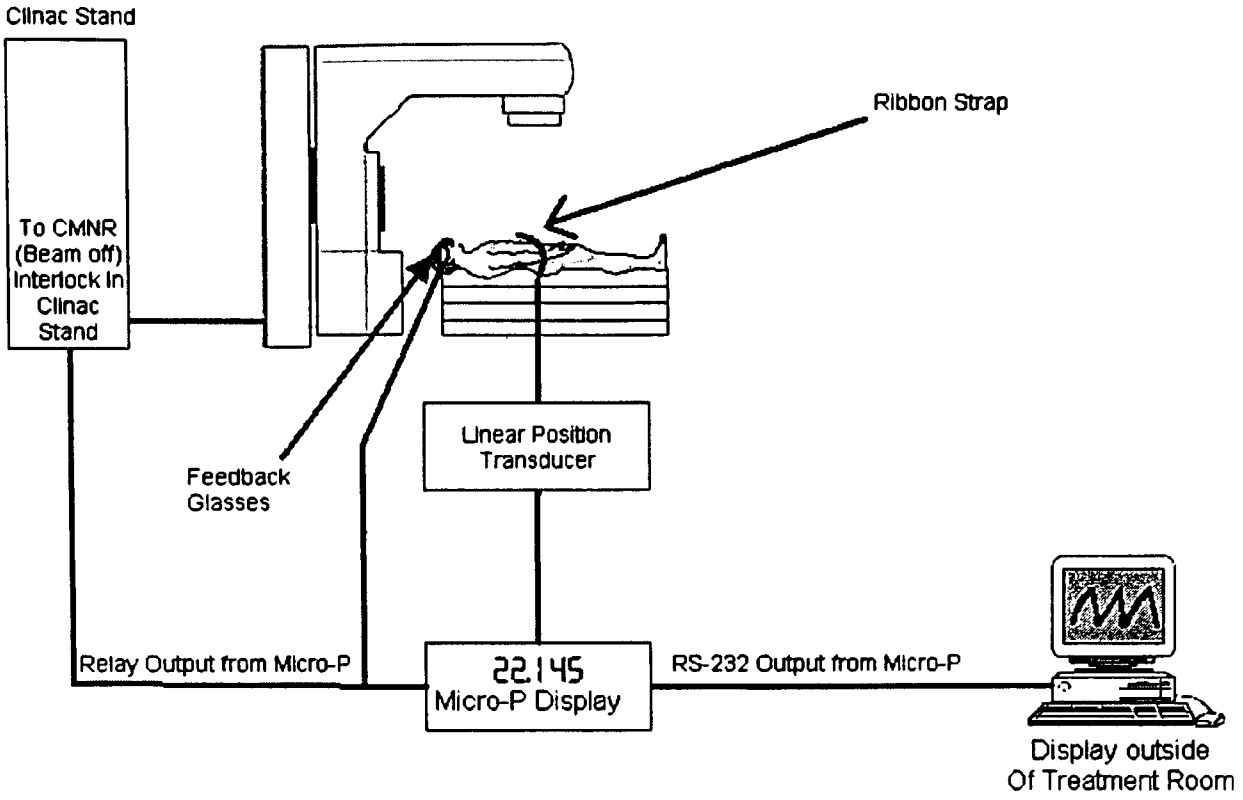

Figure 5.6. Linac setup.

5.6 Experimental verification

5.6.1 Dosimetric studies

In our Deep Inspiration Breath-Hold gated technique patients are expected to hold their breath for more than 10 seconds. Since we use a high dose rate for irradiation (600 MU/min), a single field can be treated in 1-3 breath holds. However, administration of a low number of monitor units is expected in some gating windows. The purpose of this study was to evaluate the dosimetric effects of delivering a low number of monitor units on important dosimetric characteristics, such as the X-ray central beam output, beam symmetry and beam flatness. Measurements were taken for 6 MV and 18 MV photon beams, various dose rates and various sequences for dose delivery for both in-plane (axial) and cross-plane (transverse) tests.

The calibration protocol for measuring absorbed dose in water for photons was described in Chapter 2[13]. Measurements of the central dose output have been performed, using a Farmer-type thimble chamber Extradin Model A12 (Standard Imaging, Middleton, WI), a coaxial-designed chamber made of air-equivalent plastic and suited for calibration of therapy beams in water (Fig. 5.7 a). One electrode forms a thimble-shaped shell around the collecting volume of 0.65 cm^3. The other electrode is a narrow central rod. The MAX 4000 electrometer (Standard Imaging, Middleton, WI) with a sensitivity range of 0.01 pC to 999,999 nC was used for data acquisition (Fig. 5.7 b).

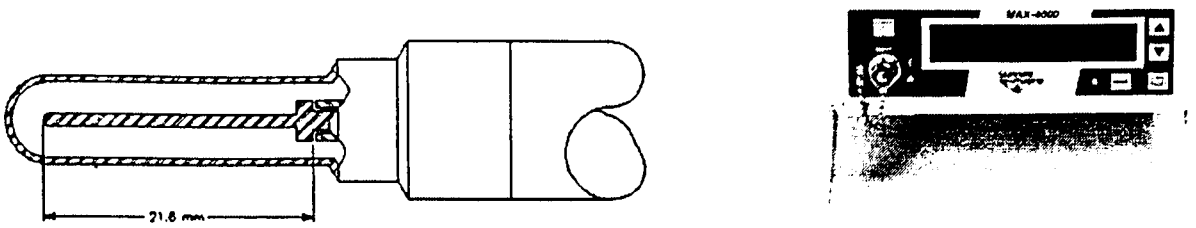

a) b)

Figure 5.7. a) Farmer-type thimble chamber Extradin Model A12; b) The MAX 4000 electrometer[45].

Measurements were carried out on a Varian Clinac 2100 C/D linear accelerator at SSD of 100 cm, a field size of 15x15 cm^2 and at 5 cm water depth. A "dose" of 100 MU corresponding to 105.7 cGy (for 6 MV photon beam) and 103.7 cGy (for 18 MV photon beam) at depth of dose maximum in phantom at SSD = 100 cm and 15x15 cm^2 field size, was delivered in three different ways:

1) As a single exposure of 100 MU;
2) In a gated sequence of 10 exposures in 10 MU increments, and;
3) In a gated sequence of 20 exposures in 5 MU increments.

These three studies have been done under one setup of the ionization chamber for beam energies of 6 and 18 MV and dose rates of 300 and 600 MU/min. The central-axis dose output values presented in the Table 5.1 are an average of three readings. For each value the standard deviation was calculated.

Table 5.1. Central axis beam dose output for 6 MV and 18 MV beams, SSD=100 cm, field size=15x15 cm^2, depth=5 cm.

Dose rate, (MU/min)	MU delivered	6 MV		18 MV	
		Central axis dose output (cGy)	ΔD (percent)	Central axis dose output (cGy)	ΔD (percent)
600	100 MU	89.44±0.01	0.0	101.47±0.01	0.0
	10x10 MU =100 MU	89.61±0.01	0.2	102.32±0.03	0.9
	20x5 MU =100 MU	90.09±0.01	0.8	102.93±0.02	1.5
300	100 MU	89.50±0.01	0.0	101.47±0.01	0.0
	10x10 MU =100 MU	89.67±0.01	0.2	102.02±0.01	0.6
	20x5 MU =100 MU	89.91±0.02	0.4	102.45±0.03	1.0

The percentage difference ΔD between the dose delivered in a sequence of several exposures and the dose delivered in one single exposure is expressed as:

$$\Delta D = \frac{D - D_n}{D} \times 100\% \ , \qquad (5.1)$$

where D is the reading from 100 MU delivered in one exposure, D_n is the reading from 100 MU delivered in multiple exposures. For n =1 the dose is delivered in 10 exposures in increments of 10 MU each, for n =2 the dose is delivered in 20 exposures in increments of 5 MU each.

The totals of the gated central axis outputs for both energies (Table 5.1) are within the range of the non-gated output values.

The dosimetric studies of the beam flatness and area symmetry were performed using a Profiler Model 1170 (Sun Nuclear Corporation, Melbourne, FL) (Fig. 5.8). This device is intended for precise verification of the radiation profile across the beam. This

beam scanning system is composed of a linear array of 46 solid-state detectors (radiation-hardened diodes) with a 5 mm spacing distance[46].

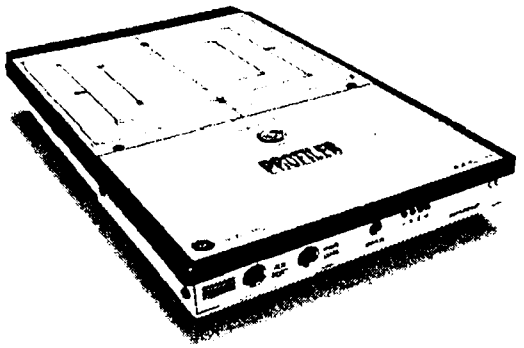

Figure 5.8. Profiler Model 1170 (Sun Nuclear Corporation, Melbourne, FL).

The same three studies with gated and non-gated sequences have been done under various setups of the Profiler for beam energies of 6 and 18 MV and dose rates of 300 and 600 MU/min. The results obtained for the flatness and area symmetry are presented in Table 5.2 for the 6 MV beam and in Table 5.3 for the 18 MV beam.

The values presented in the tables are an average of five readings. For each value the standard deviation was calculated. The Profiler calculates the flatness (FLAT) of the radiation profile using the following formula:

$$FLAT = \pm\left[\frac{MX - MN}{MX + MN}\right] \times 100\% \qquad (5.2)$$

The beam flatness, expressed as a ± percent value is calculated over 80% of the field size in the central portion of the beam. MX and MN are the maximum and minimum dose point values on the profile, respectively.

Area symmetry (SYMA) is calculated from the integrated left (SAL) and right (SAR) portions of the profile, in the central field region of 80% of the field size. The

numeric result is the percent difference of the right half of the array with respect to the left half.

$$SYMA = \left(\frac{SAR - SAL}{SAR + SAL} \right) \times 200 \qquad (5.3)$$

The Profiler result allows the user to see which reading is greater. A positive result means the right half is greater; negative means the right half is smaller.

For the cross-plane and in-plane flatness and symmetry, splitting the 100 MU delivered dose into 10 or 20 segments affects the flatness and symmetry values by less than 1%. Therefore, we conclude that the output, flatness and symmetry deviations that occurred when a dose is delivered in a gated sequence are not clinically significant.

Table 5.2. Dosimetric characteristic for the 6 MV beam profile, SSD=100 cm, field size=15x15 cm^2, d=5 cm.

	Dose rate, (MU/min)	MU delivered	Flatness (percent)	Area symmetry (percent)
axial	600	100 MU	1.7±0.1	0.2±0.1
	600	10x10 MU=100 MU	1.8±0.1	0.2±0.1
	600	20x5 MU=100 MU	1.7±0.1	0.3±0.1
transverse	600	100 MU	1.4±0.1	-0.4±0.1
	600	10x10 MU=100 MU	1.4±0.1	-0.4±0.1
	600	20x5 MU=100 MU	1.4±0.1	-0.4±0.1
axial	300	100 MU	1.7±0.1	0.1±0.1
	300	10x10 MU=100 MU	1.7±0.1	0.2±0.1
	300	20x5 MU=100 MU	1.8±0.1	0.2±0.1
transverse	300	100 MU	1.4±0.1	-0.3±0.1
	300	10x10 MU=100 MU	1.4±0.1	-0.3±0.1
	300	20x5 MU=100 MU	1.5±0.1	-0.4±0.1

Table 5.3. Dosimetric characteristic for the 18 MV beam profile, SSD=100 cm, field size=15x15 cm^2, d=5 cm.

	Dose rate, (MU/min)	MU delivered	Flatness (percent)	Area symmetry (percent)
axial	600	100 MU	1.6±0.1	0.2±0.1
	600	10x10 MU=100 MU	1.7±0.1	0.4±0.1
	600	20x5 MU=100 MU	1.7±0.1	0.4±0.1
transverse	600	100 MU	1.8±0.1	0.3±0.1
	600	10x10 MU=100 MU	1.9±0.1	0.6±0.1
	600	20x5 MU=100 MU	1.9±0.1	0.5±0.1
axial	300	100 MU	1.6±0.1	0.0±0.1
	300	10x10 MU=100 MU	1.6±0.1	0.2±0.1
	300	20x5 MU=100 MU	1.6±0.1	0.1±0.1
transverse	300	100 MU	1.8±0.1	0.2±0.1
	300	10x10 MU=100 MU	1.8±0.1	0.4±0.1
	300	20x5 MU=100 MU	1.9±0.1	0.5±0.1

Figure 5.9 shows a typical plot of the beam profile measured along a cross section of the beam. The vertical axis represents the relative dose intensity in percent at a particular detector location found on the horizontal axis. The horizontal axis has two sets of markings. The actual detector location is shown above the horizontal axis with tick marks every fourth detector, corresponding to the detector numbers on the Profiler surface. The distance markings (in cm) are shown below the horizontal axis, with 0 at the center between detectors 23 and 24; negative values to the left and positive to the right. The cumulative profile shape of an integrated dose for the 18 MV photon beam is displayed in Figure 5.9. 100 MU has been delivered as a sequence of 20 shots of 5 MU each at the dose rate of 600 MU/min.

A dosimetric experiment has also been done to check consistency of small dose delivery for various dose rates. 5 MU was administered and the axial-plane and transverse-plane profile measurements have been performed for the two beam energies (6 MV and 18 MV) at dose rates of 600 MU/min, 300 MU/min and 100 MU/min. The experiment showed that the central beam axis dose output is not affected by the dose rate.

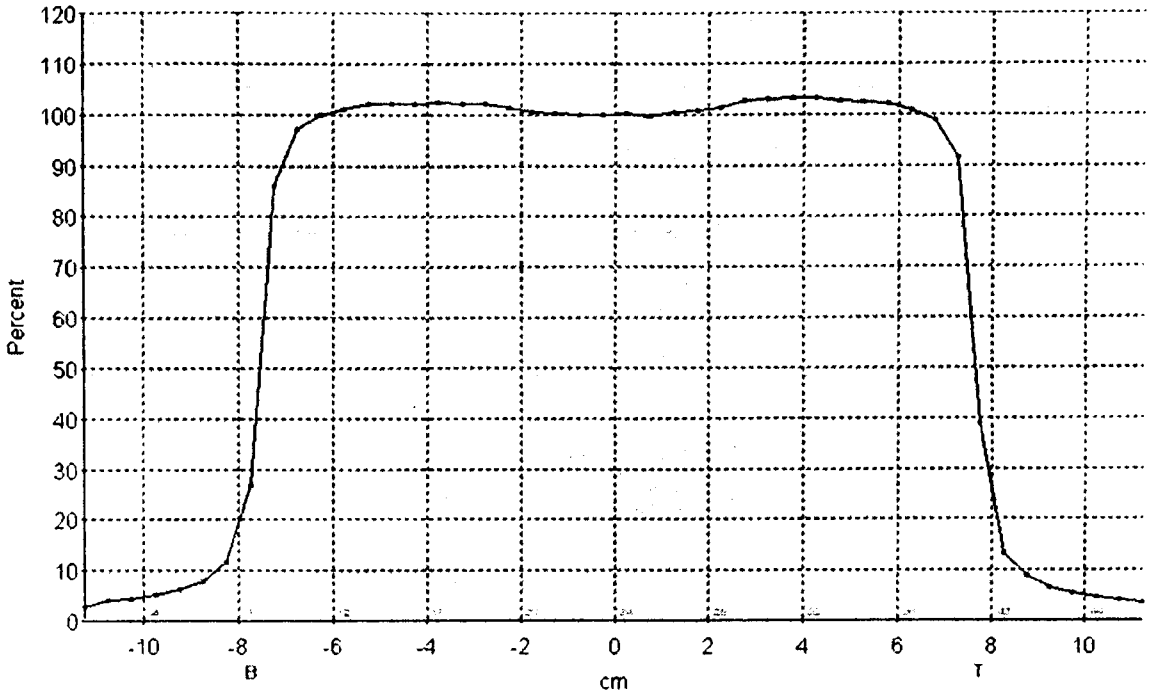

Figure 5.9. Dose profile for 18 MV energy photons, 600 MU/min, total "dose" 100 MU in 20 equal fractions of 5 MU.

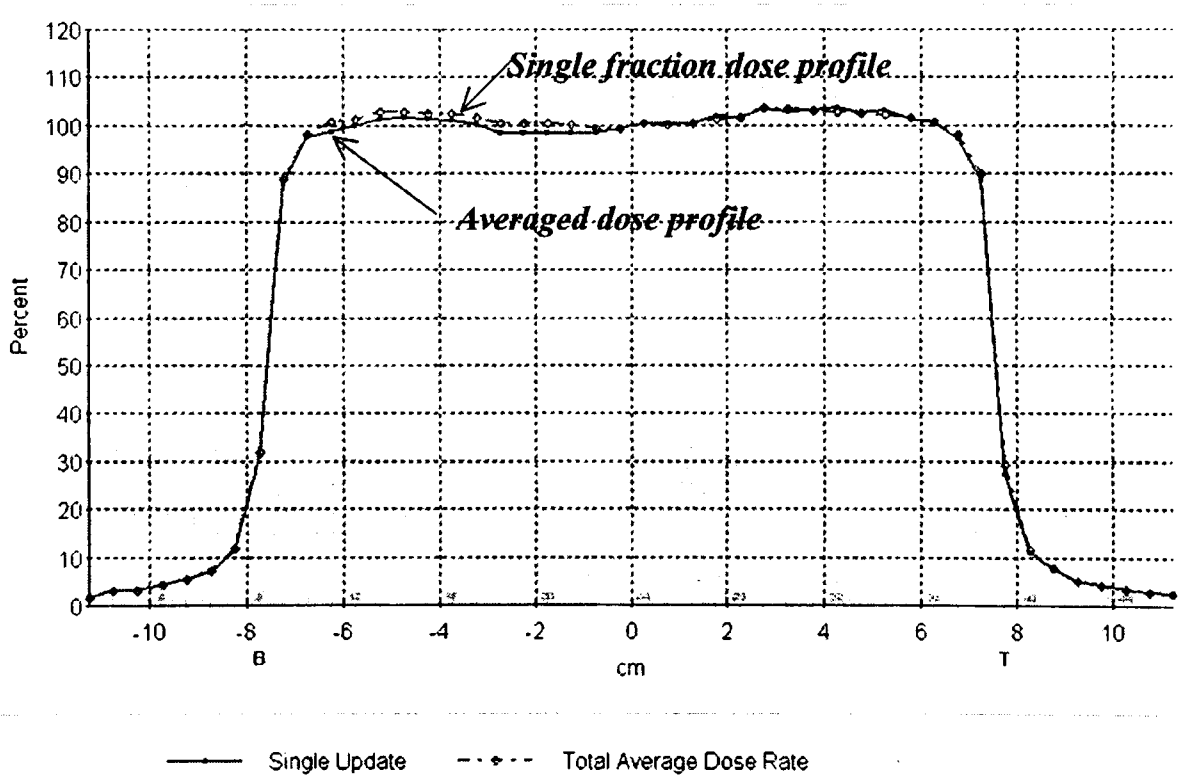

Figure 5.10. Averaged and single fraction dose profiles for 18 MV energy photons, at a dose rate of 600 MU/min, "dose": 5 MU, multiframe capturing 10 frames/sec.

Analysis of the data presented shows that flatness and area symmetry deviations are higher for single exposure of 5 MU (Table 5.4) compared to a sequence of 20 exposures of 5 MU each (Tables 5.2 and 5.3). This improvement in dosimetric beam characteristic for the integrated total dose can be attributed to improved photon statistics at larger "doses".

The results show that increasing the dose rate from the regular treatment at 300 MU/min to 600 MU/min does not affect the central axis dose output, flatness and area symmetry.

For exposures significantly less than 5 MU the flatness and area symmetry deviations can increase considerably. To illustrate this multiple-frame capturing was performed, while administrating 5 MU at a dose rate of 600 MU/min with a field size of 15x15 cm^2 at a depth of 5 cm. Multiple-frame capture consists of a series of snapshots of the beam collected periodically at regular intervals. The collection rate can be adjusted allowing profile measurements at rates up to 14 measurements per second. The application allows the transient effects to be studied. In our experiment a sequence of profiles was taken at a rate of 10 frames per second.

Figure 5.10 displays two overlaid graphs obtained using the multiple frame capture option. The profile plotted with hollow circles is the integration of all frames and is displayed for comparison with the single-frame profile. Overall 6 frames were captured for 5 MU. Approximately 19 pulses per frame were counted except for the last frame with only 10 pulses counted. Flatness and area symmetry vary from ±2.2% to ±2.6% and from −1.8% to +2.2%, respectively. The highest deviation from average for those parameters is for the last frame with a lower number of pulses.

Table 5.4. Dosimetric characteristic for the 6 MV and 18 MV beam profiles, 5 MU delivered, SSD=100 cm, field size=15x15 cm^2 and depth 5 cm.

	Photon energy, MV	Dose rate (MU/min)	Flatness (percent)	Area symmetry (percent)
axial	6	600	2.1±0.2	-0.1±0.1
	6	300	2.6±0.3	-0.9±0.3
	6	100	3.6±0.4	-1.1±0.4
transverse	6	600	1.9±0.1	0.3±0.1
	6	300	2.3±0.2	0.6±0.2
	6	100	3.2±0.5	0.8±0.2
axial	18	600	2.4±0.2	-1.3±0.5
	18	300	2.5±0.2	1.5±0.2
	18	100	2.5±0.3	1.2±0.3
transverse	18	600	2.6±0.1	2.0±0.2
	18	300	3.5±0.3	2.8±0.4
	18	100	4.2±0.3	3.1±0.4

For exposures of less than 5 MU slight deviations in flatness and area symmetry are observed. This result will not have significant clinical influence in our Deep Inspiration Breath-Hold gated radiotherapy technique. Even if 1 MU could be occasionally delivered to a patient (because of a patient's coughing or the last delivered dose during breath-hold sequence), it will not affect the overall dose distribution. The overall error due to the error in 1 MU delivery for a typical single-field treatment of 200 MU is insignificant (less than 0.5 %).

The results obtained from these experiments show that the deviation of the important dosimetric beam characteristics (central-axis output, symmetry and flatness) of the gated sequence from the non-gated are clinically insignificant. Also, the beam deviation observed shows that if a low number of monitor units (<5 MU) is delivered in a gating window the dosimetric effect over the total dose is clinically insignificant.

5.6.2 CT-simulator experiment

To illustrate experimentally how the treatment plan for the static tumor (during DIBH) can be improved compared to a treatment plan for a moving structure (free breathing) and to demonstrate how the LPT-based tracking system works, we have performed a CT-simulation study using a dynamic phantom, consisting of two moving platforms (upper and lower) with external and internal structures on top of the upper platform (Fig. 5.11). A ramp attached to each of the moving platforms allows the horizontal oscillating motion of the lower platform to be converted into vertical oscillating motion of the upper platform. A block attached to the upper ramp simulated a structure in the lung, as it oscillates during breathing.

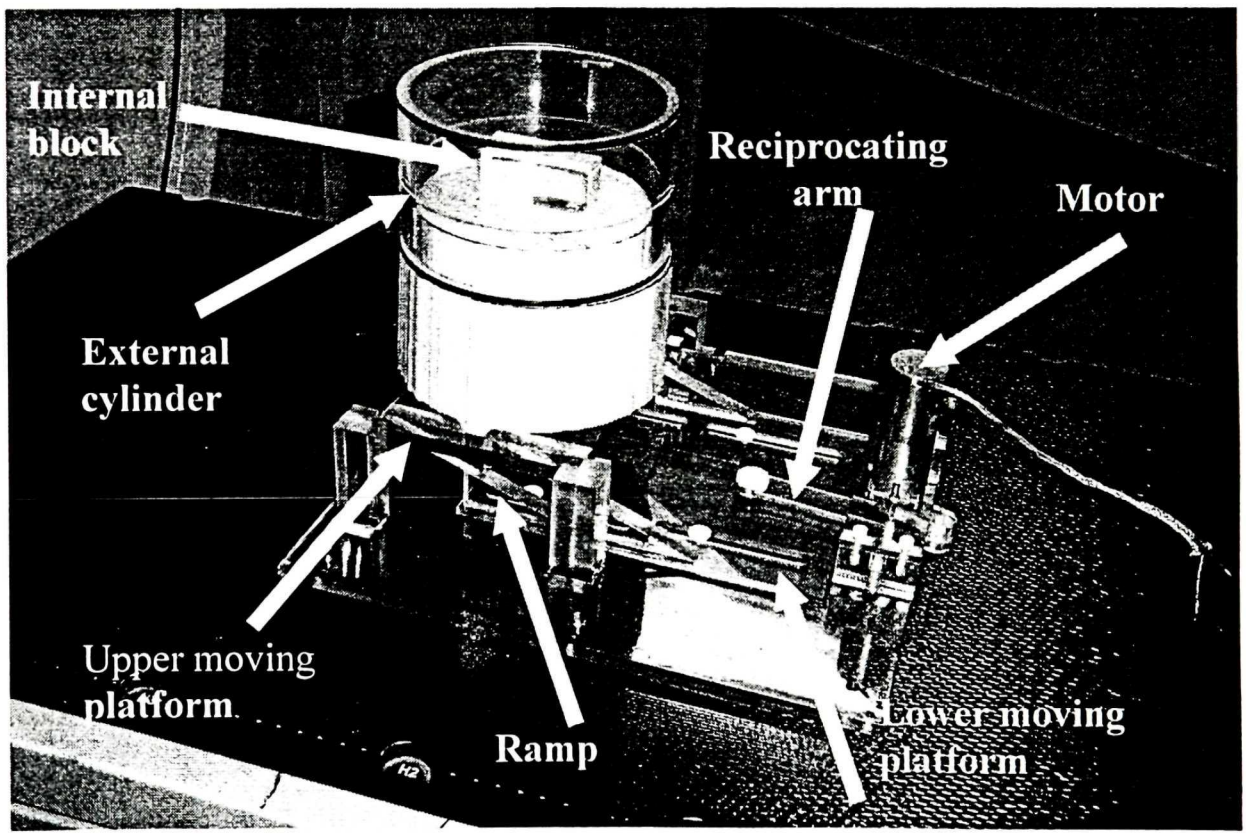

Figure 5.11. Dynamic phantom.

The entire construction was made of acrylic in order to prevent artifacts on the CT images. The lower moving platform, 17.1 cm wide by 19.9 cm long, was connected to a model 5A2320-8 TRW 24 V DC motor by a reciprocating arm which moved the platform in a horizontal (superior-interior) direction. The speed of movement was adjusted using a dual regulated - DC power supply (ANATEK model 25-2D, Freemont, CA). The range of the selected speed could vary from stationary up to 15 cycles per minute. The upper moving platform, 12.1 cm wide by 19.6 cm long, slides along the ramps of the lower platform and is thus moved in the vertical (anterior-posterior) direction with an amplitude of 1.9 cm. An acrylic hollow cylinder with a wall thickness of 0.7 cm, diameter of 15.2 cm, height of 8.3 cm and having 0.43 cm thick bottom and top covers was used as an external structure and was placed on top of a 7.6 cm thick Styrofoam layer on the upper moving platform. An acrylic block (representing a tumor structure) with parameters 2.5x2.5x6.3 cm^3 (HxWxL) and total volume of 39.4 cm^3 was placed inside the cylinder. A Styrofoam layer with a thickness of 2.5 cm separated the acrylic block structure from the bottom of the cylinder.

Helical CT imaging was performed on our Picker PQ2000S AcQSim CT simulator. Two studies were done; one for a static phantom with the block on the platform in the highest position to simulate a DIBH maneuver, and the second one for a dynamic phantom with the block on a moving platform to represent tumor displacement during a free-breathing procedure. The speed of platform movement was selected as 13 cycles per minute to simulate the effect of a typical human breathing cycle. Acquisitions were performed with a slice thickness of 3 mm.

The graphic representation of the platform movement was obtained using the LPT sensor. The sensor strap ran from the CT table rail, over the top of the cylinder on

the platform and down to the LPT. Figure 5.12(a) represents the sinusoidal motion signal for the dynamic phantom. The horizontal axis shows elapsed time in seconds and the vertical axis plots the amplitude in volts. The flat part of the signal in Figure 5.12 (b) displays the signal from the stationary platform in the highest position, simulating the DIBH maneuver.

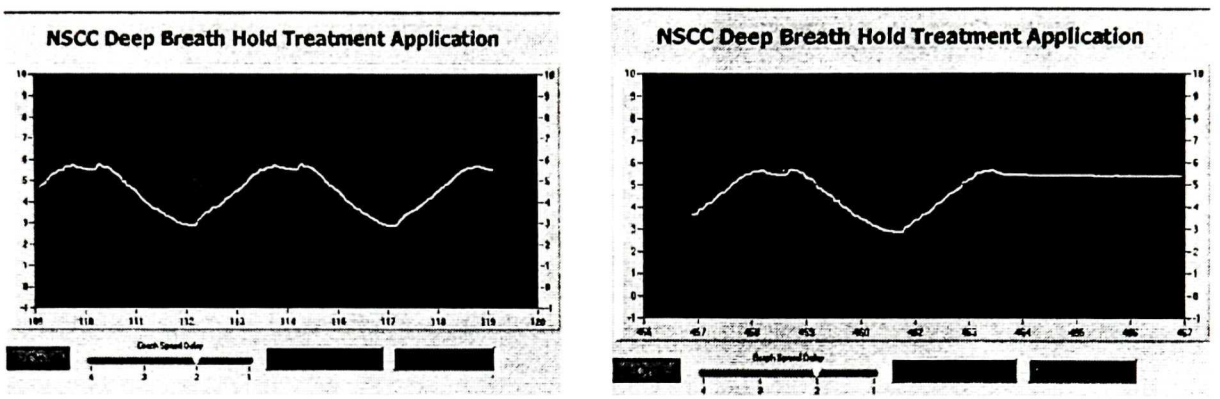

a) **b)**

Figure 5.12. a) Sinusoidal motion signal for the dynamic phantom. b) The flat part of the signal from the stationary platform in the highest position.

The phantom CT study was transferred to the treatment planning computer and the internal and external structures have been outlined. The Gross Target Volume (GTV) was outlined on each scan and three-dimensional graphical structures were created. The structure of the stationary simulation had a rectangular shape and appeared exactly the same as the original block (Fig. 5.13 a). The treatment-plan-calculated volume of the structure was 39.4 cm^3, in good agreement with the volume calculated from its physical dimensions. A three-dimensional picture of the dynamic block shows distortions caused by motion (Fig. 5.13 b). The treatment-plan-calculated dimensional volume of 44.92 cm^3 was significantly larger than the actual physical volume of 39.4 cm^3.

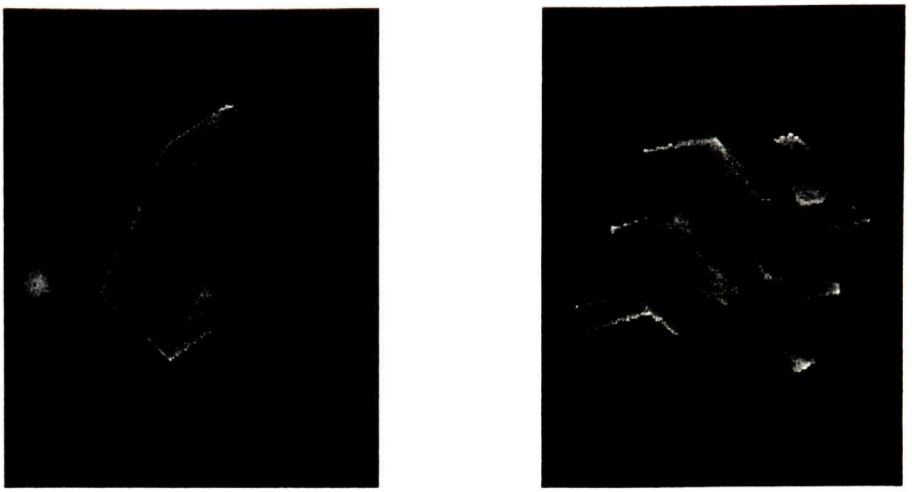

a) **b)**

Figure 5.13. 3D graphical reconstruction: a) static phantom; b) dynamic phantom.

The observed difference in volumes can be attributed to an imprecision in outlining slices of the dynamic structure because of blurred edges. A comparison of Planning Target Volumes shows significant differences (Fig. 5.14, Fig. 5.15). In the static case, margins of 1 cm were chosen, while in the dynamic case the same margins of 1 cm were added and the movement of the structure with an amplitude of 1.9 cm was taken into account. This resulted in a PTV of 164 cm^3 for the static case and a PTV of 277.5 cm^3 for the dynamic case.

The cumulative Dose Volume Histograms for static and dynamic plans show a 14% difference for the GTVs and a 69% difference for the PTVs. In the latter case the difference between the planning target volumes can be attributed to the extra margins added to the dynamic PTV in order to account for the motion.

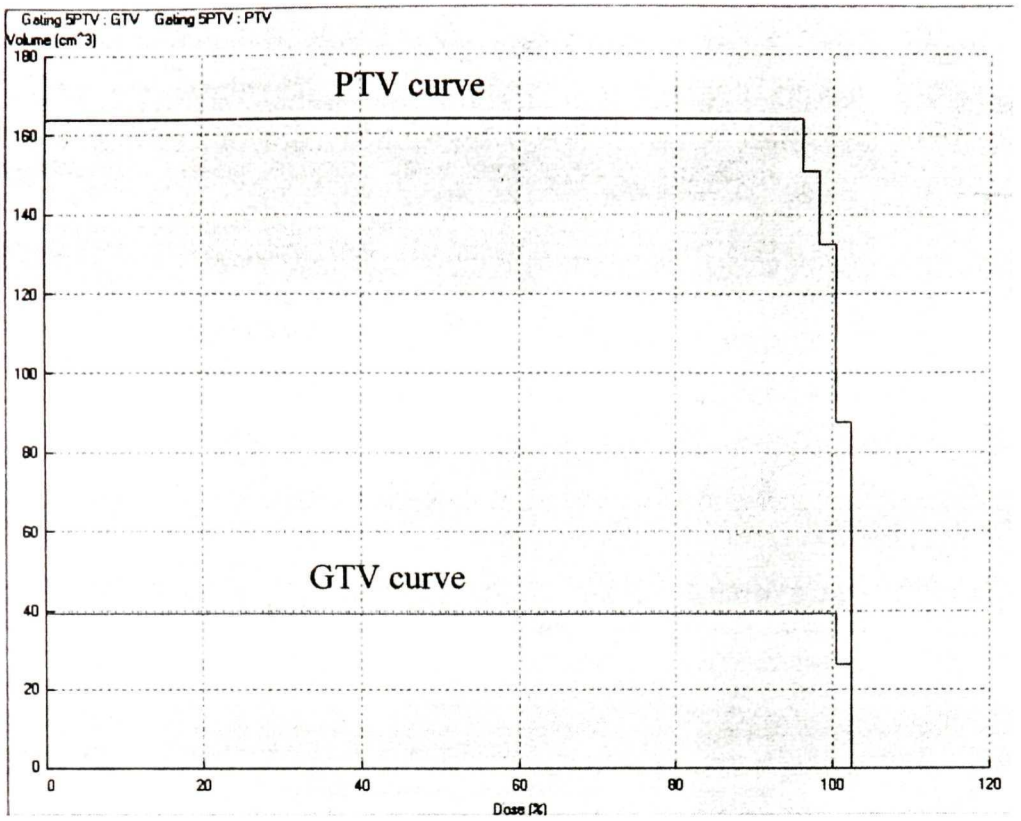

Figure 5.14. Cumulative DVH for the static phantom.

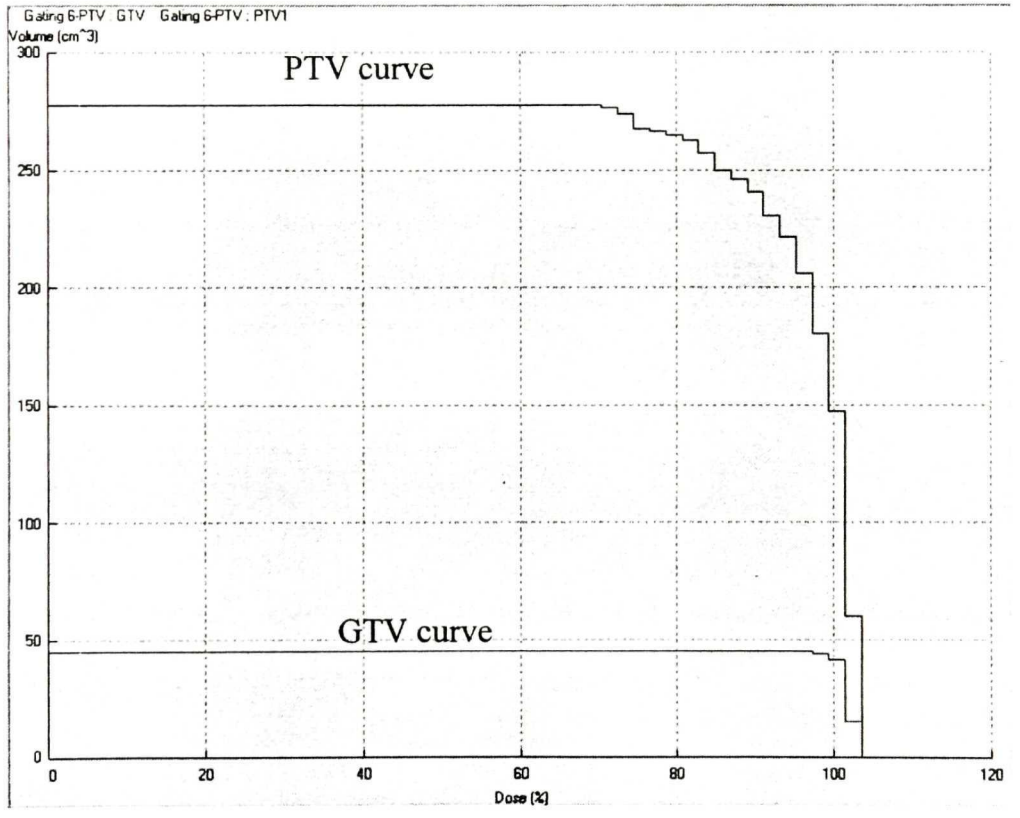

Figure 5.15. Cumulative DVH for the dynamic phantom.

Chapter 6.

Discussion

The Breathing-Synchronized Radiotherapy is a relatively new approach in treatment of thoracic-abdominal lesions and, its development and clinical implementation have been rapid. In the first phase of our research in the Nova Scotia Cancer Centre we have revised and critically analyzed all existing Breathing-Synchronized Radiotherapy methods. In our work, based on the research and experience of other hospitals involved in breathing-synchronized treatments, we have developed and implemented a Deep Inspiration Breath-Hold radiotherapy technique for treatment of patients with thoracic lesions.

Our system is based on the use of a new external motion sensor – a Linear Position Transducer (LPT) to monitor patient breathing-induced organ motion by tracking changes in the patient's abdominal cross-sectional area. The LPT is a patient-friendly, easy to operate and cost-effective device. However, the implementation of our technique has some limitations. First of all, it is not suitable for all patients with thoracic-abdominal lesions. Patients with shallow and abdominal breathing patterns have to be excluded, because the LPT sensor cannot track adequately in a reproducible manner if the chest displacements during normal breathing and breath-hold are distinctly different. The LPT tracking accuracy can also be affected by the patient's weight loss and content of the stomach.

As found by previous users of breathing-synchronized radiotherapy, our first DIBH patient experience shows a significant increase in treatment time compared to the

conventional radiotherapy (15 to 30 minutes). It is expected that this time will decrease as the patients and the therapists get used to technique. Our experience with the first DIBH patient has shown that the setup time increased significantly compared to the conventional therapy procedure. We hope that the time of the sensor adjustment during the setup will be reduced as the therapists get used to the technique.

In our technique we used a DIBH maneuver, which allows sparing of normal tissue due to lung expansion, and thereby moving healthy lung tissue away from the primary beam and achieving tumor immobilization. One of the most significant benefits of using DIBH compared to free-breathing approaches is avoiding any discrepancy between the internal organ movement and external chest movement. Performing this maneuver for a patient is not as comfortable as free-breathing gating, but it reduces the residual target motion to about 10%, as compared to 40% for a free breathing gated technique[47]. Implementation of DIBH requires at least one 30-minute patient training session prior to simulation. During this session the patient is trained to perform the DIBH maneuver reproducibly and to increase the time of a breath hold.

Various authors have shown that the feedback of the breathing signal to the patient plays a positive role in signal reproducibility[48,49]. In our approach to allow patients to cooperate fully in the process and to provide assurance that the system is properly monitoring their breathing, we have used a set of feedback glasses with built-in LEDs. From our first patient experience it was demonstrated that this is a very effective method for enabling the patient to maintain a steady breath hold and to improve the duration of the breath hold.

Before implementing this technique in the clinic, we conducted dosimetric studies of dose delivery with low monitor units. It has been shown that the deviation of

the most important beam characteristics (central axis output, flatness and symmetry) are within 1%, and clinically insignificant. Our results correlate well with data obtained by other investigators[31,40,41,42,43].

The goal of implementing this technique was to improve the accuracy of the dose delivery and to spare the healthy lung tissue. Our CT experiment with a dynamic phantom has shown how a treatment plan for a static structure differs from a treatment plan for a moving structure. Elimination of movement with an amplitude of 1.9 cm for a structure with parameters 2.5x2.5x6.3 cm^3 will decrease the planning treatment volume by a factor of about 1.7.

At the time of writing the first patient has been treated using the gated DIBH radiotherapy technique. The patient had a 3 cm mass in the superior segment of the right lower lobe as well as ipsilateral mediastinal lymphadenopathy. The patient was involved in gated treatment during phase II. In phase I he received conformal radiotherapy treatment. The patient was trained for the DIBH maneuver, was very cooperative and performed breath-holds very well. The CT-simulation with a thoracic scan, which included all lung tissue, was performed during breath-hold maneuvers.

Coronal slice reconstructions from phase I – free breathing during image acquisition (Fig. 6.1) and phase II – DIBH during image acquisition (Fig. 6.2) have been compared and analyzed. Significant blurring effects can be observed on the free-breathing image (Fig. 6.1) related to periodical respiratory motion of anatomical structures.

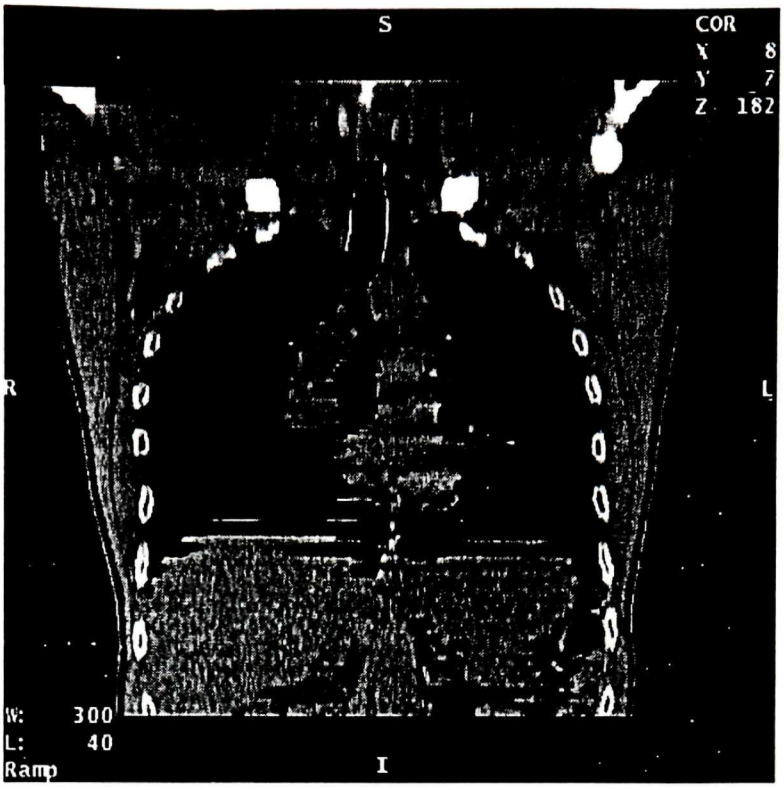

Figure 6.1. Coronal slice reconstruction for free breathing during image acquisition (phase I).

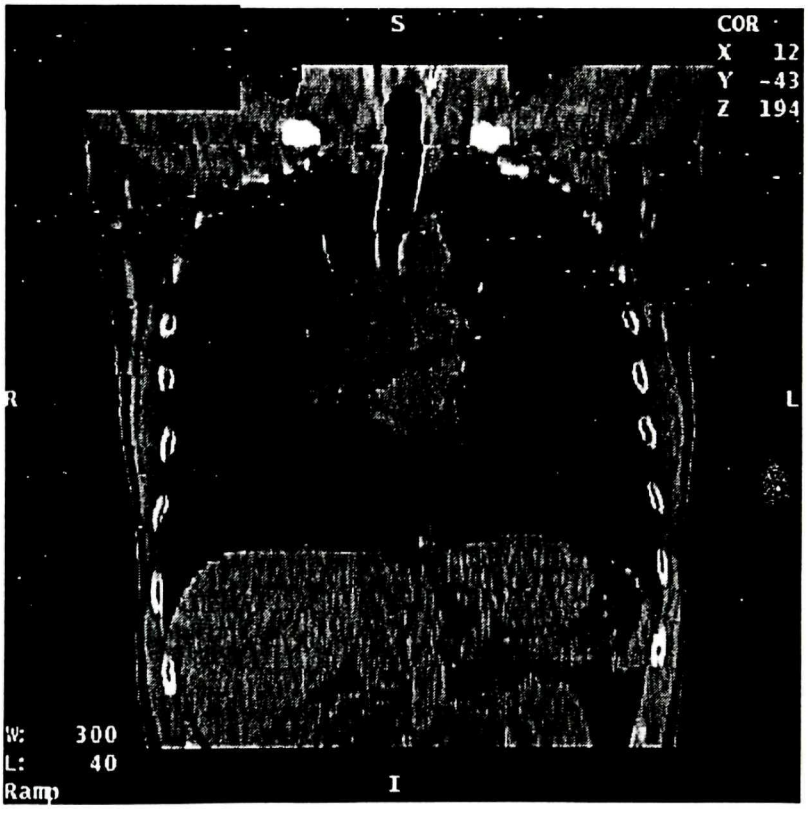

Figure 6.2. Coronal slice reconstruction for DIBH maneuver during image acquisition (phase II).

The radiation oncologist has decided not to reduce the PTV margins and did not change the field size for the first patient. However, even with the same parameters, the treatment planning has shown a 3% reduction in V20. V20 represents a percentage of total lung volume minus the PTV that receives a dose greater than 20 Gy. If the value of V20 is less than 30% then the risk of pulmonary complications is considered acceptably low[50].

Under the DIBH the total lung volume increased by 26%, from 5000 cm^3 to 6300 cm^3. If tighter PTV margins had been used, a significant amount of healthy lung tissue would have been excluded from the high-dose region and dose escalation to the target volume would have been possible with the same risk of normal tissue complications.

Chapter 7.

Conclusions

An automated Deep Inspiration Breath-Hold (DIBH)-gated technique for treatment of patients with thoracic lesions has been developed, evaluated and implemented in 2002 at the Nova Scotia Cancer Center in Halifax. A new external motion sensor, a Linear Position Transducer (LPT), has been used for tracking the organ position in thoracic region during a breath-hold. It was demonstrated that the sensor has a rapid response and produces accurate and reproducible signals. The system proved to be accurate, efficient and cost-effective in comparison with existing commercial systems. Treatment can be delivered automatically whenever the patient achieves a preset deep-inspiration breath level with the accelerator gating. Our work confirmed the feasibility of the gated DIBH radiotherapy technique in treatment of thoracic lesions and its ability to dramatically improve the accuracy of treatment for moving tumors. Measurements of gated beam characteristics showed that neither the gating nor the low-dose delivery affect the beam characteristics significantly.

Unfortunately, not all lung cancer patients are candidates for treatment with our technique. To perform the DIBH maneuver the patient should have lungs in relatively good functional condition, no significant cough and low anxiety. Because of these criteria a large number of patients are not suitable for the DIBH gated treatment; however, those who are suitable can obtain considerable benefits from this treatment technique. Despite some of the limitations, our technique has allowed us to successfully immobilize the tumor, reduce the lung volume in the high dose region and gate the beam

automatically. The first patient experience demonstrated clearly that our technique is effective and has the potential to reduce toxicity and improve tumor control.

Although the present work uses a LPT as a sensor, the technique can be adapted to other sensors easily. In the future we plan to develop the technique further to make it accessible to all radical patients with thoracic-abdominal lesions and to improve the accuracy.

List of figures

Bibliography

[1] National Cancer Institute of Canada: Canadian Cancer Statistics. Toronto, ISSN 0835-2976, April 2002.

[2] Report of the Lung Cancer Progress Review Group.

[3] Ginsberg R, et al. Cancer: Principles and Practices of Oncology. 5th ed. 1997; 858-911.

[4] Khan. F, Potish R. Treatment planning in Radiation Oncology. Williams & Wilkins, 1998; 567-582.

[5]ICRU report 62. Prescribing, recording and reporting photon beam therapy (supplement to ICRU report 50). Issued: 1 November 1999.

[6] Rosenzveig K, Hanley J, Mah D, et al. The deep inspiration breath-hold technique in the treatment of inoperable non-small-cell lung cancer. *Int J Radiat Oncol Biol Phys* 2000; 48 (1): 81-87.

[7] Ohara K, Okumura T, et al. Irradiation synchronized with respiration gate. *Int J Radiat Oncol Biol Phys* 1989; 17: 853-857.

[8] Chen Q.-S, Weinhous M, et al. Fluoroscopic study of tumor motion due to breathing: facilitaiting precise radiation therapy for lung cancer patients. *Med Phys* 2001; 28(9).

[9] Mageras G, Yorke E, et al. Fluoroscopic evaluation of diaphragmic motion reduction with respiratory gated radiotherapy system. *J Appl Clin Med Phys* 2002; 52: 1389-1399.

[10] Mageras G, Yorke E, et al. Initial clinical evaluation of a respiratory gating radiotherapy system. Memorial Sloan-Kettering Cancer Center, NY, USA, Scientific session WE-EBR-04 Treatment techniques 1.

[11] Mah D, Hanley J, et al. Technical aspects of the deep inspiration breath-hold technique in the treatment of thoracic cancer. *Int J Radiat Oncol Biol Phys* 2000; 48(4): 1175-1185.

[12] Podgorsak E.B, Radiation physics. Course materials.

[13] AAPM TG-51. A protocol for clinical reference dosimetry of high-energy photon and electron beams. *Med Phys* 1999; 26(9).

[14] AAPM TG-21. A protocol for the determination of absorbed dose from high-energy photon and electron beams. *Med Phys* 1983; 10: 741-771.

[15] Van Dyk J, et al. The Modern Technology of Radiation Oncology. Medical physics publishing, Madison,Wisconsin, 1999.

[16] Curry T, Dowdey J, Murry R. Christinsen's Physics of diagnostic radiology. Lippincott Williams & Wilkins, 4th edition, 1990.

[17] http://www.bh.rmit.edu.au/mrs/kpm/EPCR/XII.GIF.

[18] Peters T. Introduction to the principles of computed tomography. Montreal neurological institute, McGill.

[19] http://www.amersham-health.com/medcyclopaedia/CT.html.

[20] Greene D, Williams P. Linear Accelerators for Radiation Therapy. IOP Publishing Ltd, 1997.

[21] Podgorsak E.B, Van Dyk J, et al. The Modern Technology of Radiation Oncology. Medical physics publishing, Madison,Wisconsin. 1999; p.349-435.

[22] C-series Clinac® High Energy Beam Delivery System. Varian medical systems, 2000.

[23] Podgorsak E.B, Rawlinson J, et al. Design of X-ray targets for high energy linear accelerators in radiotherapy. *Am J Roentgenol Rad Ther and Nucl Med* 1974; 121: 873-882.

[24] Podgorsak E.B, Rawlinson J, et al. X-ray depth doses from linear accelerators in the energy range from 10 to 32 MeV. *Am J Roentgenol Rad Ther and Nucl Med* 1975; 123: 182-191.

[25] Leung P. The physical basis of radiotherapy. The Ontario Cancer Institute incorporating the Princess Margaret Hospital, 1990.

[26] Ramsey C; Spencer K, et al. Full-Scale Clinical Implementation of a Video based Respiratory Gating System. American Association of Physicists in Medicine 41th Annual Meeting; *Med Phys* 2000; 27(6).

[27] Kubo H, Len P. Breathing-synchronized radiotherapy program at the University of California Davis Cancer Center. *Med Phys* 2000; 27(2).

[28] Hampton L. RPM^{TM} Respiratory Gating. Varian Medical Systems talk in Sydney (NS), October 2002.

[29] Kubo D, Wang L. Introduction of audio gating to further reduce organ motion in breathing synchronized radiotherapy. *Med Phys* 2002; 29(3).

[30] Shirato H, Shimizu S, et al. Four-dimensional treatment planning and fluoroscopic real time tumor tracking radiotherapy for moving tumor. *Int J Radiat Oncol Biol Phys* 2000; 48(2): 435-442.

[31] Kubo D, Hill B. Respiration gated radiotherapy treatment: a technical study. *Phys Med Biol* 1996; 41: 83-91.

[32]Respiratory Gating. http://www.thompsoncancer.com/radonc/gating.cfm.

[33]O'Dell W, Schell M, et al. Dose broadening due to target position variability during fractionated breath-held radiation therapy. *Med Phys* 2002; 29(7): 1430-1437.

[34] Hanley J, Debois M, et al. Deep inspiration Breath-hold technique for lung tumors: the potential value of target immobilization and reduced lung density in dose escalation. *Int J Radiat Oncol Biol Phys* 1999; 45(3): 603-611.

[35] Stromberg J, Sharpe M, et al. Active Breathing Control (ABC) for Hodgkins Disease: Reduction in Normal Tissue Irradiation with Deep Inspiration and Implications for Treatment. *Int J Radiat Oncol Biol Phys* 2000; 48(3): 797-806.

[36] www.electa.com.

[37] Balter J, Ten Haken R, et al. Uncertainties in CT-based radiation therapy treatment planning associated with patients breathing. *Int J Radiat Oncol Biol Phys* 1999; 45(3): 603-611.

[38] Ding D, Fourkal E, et al. Organ Motion in Radiation Therapy of Lung Cancer. Department of Radiation Oncology, Fox Chase Cancer Center, Philadelphia, PA 19111. AAPM talk, Montreal 2002.

[39] Rithie C, Hsieh J, et al. Predictive Respiratory Gating: A New Method to Reduce Motion Artifacts On CT Scans. *Radiology* 1994; 190: 847-852.

[40] Ramsey C, et al. A comparison of beam characteristics for gated and non-gated clinical X-ray beams. *Med Phys* 1999; 26(10): 2086-2091.

[41] Shen S, Duan J. QA Considerations in RPM Gated CT Data Acquisition and Treatment for 3-D RT and IMRT. University of Alabama at Birmingham, AL. AAPM talk, Montreal 2002.

[42] Yorke E, Mageras G, Ford E, et al. Respiratory Gating QA at MSKCC. AAPM talk, Montreal 2002.

[43] Goddu S, Vanek K, et al. Respiratory Gated IMRT: Dosimetric Verification. Medical University of South Carolina, Charleston, SC 29425. AAPM talk, Montreal 2002.

[44] www.unimeasure.com.

[45] www.standardimaging.com.

[46] Profiler Model 1170, Operating Instructions. SUN Nuclear Corporation, Melbourne, Florida.

[47] Yewondwossen M, Denissova S, Andrew J, et al. A Gated Deep Inspiration Breath-Hold Radiation Therapy Using a Linear Position Transducer. *Med Phys* 2003 (to be published).

[48] Vedam S, Keall P, et al. Fluoroscopy based simulation using the Varian Real-time Position Management (RPM) Respiratory Gating System. University of Texas M.D. Anderson Cancer Center, Houston TX USA. AAPM talk, Montreal 2002.

[49] Kini V, Vedam S, et al. Patient training in respiratory-gated radiotherapy. *Medical Dosimetry* 2003; 28(1): 7-11.

[50] Graham M, Purdy J, et al. Clinical dose-volume histogram analysis for pneumonitis after 3D treatment for non-small cell lung cancer. *Int J Radiat Oncol Biol Phys* 1999; 45(2): 323-329.